

TRANSPORT IN LOW PRESSURE PLASMA REACTORS FOR MATERIALS  
PROCESSING

BY

VIVEK VYAS

B.Tech., Indian Institute of Technology, Bombay, 2000  
M.S., University of Illinois at Urbana-Champaign, 2003

DISSERTATION

Submitted in partial fulfillment of the requirements  
for the degree of Doctor of Philosophy in Materials Science and Engineering  
in the Graduate College of the  
University of Illinois at Urbana-Champaign, 2005

Urbana, Illinois

# TRANSPORT IN LOW PRESSURE PLASMA REACTORS FOR MATERIALS PROCESSING

Vivek Vyas, Ph.D.

Department of Materials Science and Engineering  
University of Illinois at Urbana-Champaign, 2005

Mark J. Kushner, Adviser

Plasmas are used extensively in semiconductor manufacturing for etching features and vias, for depositing metals to make interconnects, and for cleaning reactors between wafers. The development of plasma equipment models (PEMs) for investigating chemical, physical, and engineering scaling issues for plasma processing has significantly advanced in recent years. The continuous shrinking of the minimum feature size in microelectronics fabrication has necessitated the use of high-density low-pressure plasma sources. At these pressures, conventional fluid or hybrid simulations are of questionable validity as transport is highly nonequilibrium and a kinetic approach may be warranted.

In this study, a Monte Carlo simulation for ion and neutral transport (IMCS) has been developed and integrated with a plasma equipment model to improve the capabilities to address lower pressures. The ion/neutral energy distribution functions obtained from the IMCS are used to obtain transport coefficients for use in heavy particle momentum conservation equations. The plasma properties obtained using the fluid and the hybrid model have been compared with experiments. The heavy particle temperatures are found to significantly influence densities, electron temperatures, and sputter rates. The consequences of varying power, pressure, and gas chemistries have been investigated for several low-pressure tools.

Ionized metal physical vapor deposition (IMPVD) at pressures of a few mTorr is being increasingly used to deposit diffusion barriers and Cu seed layers into high aspect ratio trenches. Understanding plasma-substrate interactions will be critical to designing the next generation

processes as the industry transitions to the 45-nm node. In this work, IMPVD using a hollow cathode magnetron source has been modeled at the reactor and feature scale. The consequences of varying process parameters such as power, pressure and magnetic fields have been investigated for a hollow cathode magnetron source and comparison has been made with experiments. The fluxes incident on the wafer are strongly influenced by the magnetic field configuration and strength. The ion flux incident on the wafer increases with pressure due to larger number of ionizing collisions. A Monte Carlo Feature Profile Model has been used to investigate the Cu seed layer deposition process. The effect of process conditions on the energy and angular distributions has been investigated. The lateral overburden at the mouth of features, or “overhang,” is strongly correlated to the ion and neutral energy and angular distributions and the ion flux incident on the substrate.

## **ACKNOWLEDGMENTS**

I would like to express my profound gratitude to my adviser, Prof. Mark J. Kushner, for his constant support, encouragement and valuable suggestions.

My sincere thanks go to the members of my dissertation committee, Professor John Abelson, Professor Robert Averback, and Professor Angus Rockett for their thoughtful comments.

I would like to acknowledge the support of the Semiconductor Research Corporation, Novellus Systems, and the National Science Foundation (NSF). Thanks are also due to Larry Gochberg and Daniel Juliano for the internship experience at Novellus.

I am also thankful to my fellow members in the Computational Optical and Discharge Physics Group: Ron Kinder, Junqing Lu, Rajesh Dorai, Arvind Sankaran, Pramod Subramonium, Kapil Rajaraman, Richard Moss, Alex Vasenkov, Ananth Bhoj, Shane Stafford, Ramesh Arakoni, Ankur Agarwal, and Kelly Collier. Thanks also are due to my roommates and friends for making my stay in Urbana-Champaign such an enjoyable experience.

I am most indebted to my parents, my sisters, and relatives for their constant support and encouragement throughout the course of my education.

# TABLE OF CONTENTS

	Page
CHAPTER 1 INTRODUCTION	
1.1 Plasma Processing for Semiconductor Applications.....	1
1.2 Ionized Metal Physical Vapor Deposition .....	2
1.3 Plasma Process Modeling.....	7
1.4 Summary .....	10
1.5 References .....	11
1.6 Figures.....	14
CHAPTER 2 HYBRID PLASMA EQUIPMENT MODEL .....	
2.1 Introduction.....	20
2.2 The Electromagnetics Module .....	20
2.3 The Electron Energy Transport Module .....	22
2.3.1 Electron energy equation method .....	23
2.3.2 Electron Monte Carlo simulation .....	24
2.4 The Fluid-Chemical Kinetics Module .....	25
2.5 The Sputter Module .....	28
2.6 The Plasma Chemistry Monte Carlo Module .....	32
2.7 References.....	33
CHAPTER 3 MONTE CARLO FEATURE PROFILE MODEL .....	
3.1 Introduction.....	35
3.2 Description of the Model .....	35
3.3 Surface Reaction Mechanism for Cu IMPVD .....	40
3.4 References.....	41
CHAPTER 4 ION/NEUTRAL MONTE CARLO SIMULATION.....	
4.1 Introduction.....	43
4.2 Description of the Model .....	43
4.3 Validation.....	49
4.4 Comparative Study of the IMCS and the Fluid Model.....	51
4.5 Summary .....	55
4.6 References.....	56
4.7 Tables.....	57
4.8 Figures.....	58
CHAPTER 5 IONIZED METAL PHYSICAL VAPOR DEPOSITION.....	
5.1 Introduction.....	77
5.2 Description of the Model .....	77
5.3 Cu IMPVD in a Hollow Cathode Magnetron Source .....	78
5.4 Summary .....	89
5.5 References.....	90
5.6 Figures.....	91

CHAPTER 6 CONCLUSIONS .....	128
APPENDIX A: SURFACE REACTIONS FOR Cu DEPOSITION IN Ar BUFFER GAS.....	130
APPENDIX B: LIST OF REACTIONS FOR Ar.....	131
APPENDIX C: LIST OF REACTIONS FOR Ar/Cl <sub>2</sub> .....	133
APPENDIX D: LIST OF REACTIONS FOR Ar/Cu.....	135
AUTHOR'S BIOGRAPHY .....	137

# CHAPTER 1

## INTRODUCTION

### 1.1 Plasma Processing for Semiconductor Applications

Plasma processing of materials is an essential technology for microelectronics fabrication [1]. Plasmas are employed in semiconductor manufacturing for etching features and vias, for depositing metals to make interconnects, and for cleaning reactors between wafers [2]. Plasma processing of semiconductors is achieved by electron impact dissociation of feed stock gases to produce neutral radicals and ions, which drift or diffuse to the wafer where they etch or deposit materials. Silicon etching in a capacitively coupled discharge is shown in Fig. 1.1.

Conventional plasma reactors, which use parallel plates with capacitive coupling, can only generate low-density plasmas ( $10^9$ - $10^{10}$   $\text{cm}^{-3}$ ) as there is an upper limit to the bias voltage to prevent wafer damage from energetic ions [3-4]. The plasma power and ion energy sources are decoupled in high-density plasma reactors. The common methods used to generate high-density plasmas ( $10^{11}$ - $10^{12}$   $\text{cm}^{-3}$ ) include electron cyclotron resonance (ECR), helicon waves and inductive coupling. In an ECR reactor, a microwave source with a frequency equal to the electron cyclotron frequency produces a high plasma density at low pressures [5-6]. Helicon plasma sources apply steady-state magnetic fields to induce helicon waves along magnetic field lines of power [7-8]. In ICP reactors, the power is coupled to the plasma through an antenna, which acts as a transformer [9-10]. The plasma acts as a single-turn conductor that is coupled to a multiturn nonresonant rf coil around the dielectric discharge chamber. To control ion energy to the substrate in these reactors, the electrode on which the wafer is placed can be independently driven by a capacitively coupled rf source. The ions created in the bulk plasma by inductive

coupling are accelerated in the sheath near the wafer by applying an rf bias on the electrode. This is the cause of the anisotropic distribution of ions incident upon the wafer.

## **1.2 Ionized Metal Physical Vapor Deposition**

Moore's law, which forecasts that the performance of microprocessors will double every 18 months, has held since 1965, when it was proposed by Gordon Moore [11]. Moore's law is illustrated by the growth of the number of transistors in logic chips over the years in Fig. 1.2. This trend translates into decreasing feature sizes and increasing number of devices per die in microelectronics. As the number of devices per die increases and critical dimensions decrease, the time delay resulting from metal interconnect wiring becomes an increasingly important consideration in optimizing the performance of integrated circuits (ICs). As much as 90% of the signal delay time in the 100 nm generation of ICs will likely be due to interconnect wiring, while only 10% will be due to actual device switching [12,13]. The need for low-power, high-performance IC designs necessitates the use of Cu as an interconnect material. The low resistivity of Cu ( $1.67 \mu\Omega/\text{cm}$ ) reduces on-chip RC time delay. Copper's lower resistance also improves power distribution, which improves device performance throughout the chip. The higher resistance to electromigration for Cu also improves long-term reliability of ICs. An example of nine-level copper interconnects with low-k ILD as the current state of the art is shown in Fig. 1.3 [14].

The introduction of copper metallization has necessitated new fabrication processes. The metal etch processes critical for aluminum alloy interconnects have been largely eliminated and new processes such as damascene and dual damascene have been introduced [15]. The steps involved in the copper technology scheme are shown in Fig 1.4. The damascene or dual

damascene interlevel or intermetal dielectric is deposited. This dielectric may be multilayered and include etch stops such as silicon nitride and the deposition may require a planarization step using CMP. The damascene or dual damascene structure is then patterned and etched into the dielectric. A diffusion barrier/seed stack is deposited using physical vapor deposition followed by electroplating to fill the features with copper. The excess copper is next polished away using chemical mechanical planarization.

Sputter deposition is one of the most widely used techniques for the fabrication of thin-film structures on semiconductor wafers. Sputter deposition is usually carried out in diode plasma systems known as magnetrons, in which the cathode is sputtered by ion bombardment and emits the atoms, which are then deposited on the wafer in the form of a thin film. This ion bombardment generates collision cascades in the atomic lattice of the target, and some target atoms obtain enough energy from the collision cascades to escape from the atomic lattice. The dynamics of the collision process depend strongly on the incident energy and mass of the bombarding particle. At moderate energies in the range of several hundred eV to several keV, the incident particle can cause substantial numbers of near-surface broken bonds, atomic dislocations, and ejection or sputtering of atoms. Sputtering is widely used to deposit a wide variety of pure metal, alloy, and insulator films at reasonable deposition rates and with good uniformity, surface smoothness, and adhesion.

The dimensions (10s of nm) of the trenches and vias and high aspect ratios (3-10) are generally incompatible with conventional sputter deposition due to the broad angular distribution of the sputtered atoms. Sputter deposition into these features results in significant overhang formation and eventual void formation, which causes increased resistance as well as reliability concerns. A solution to this problem has been collimated sputtering, in which a physical filter is

used with conventional low pressure sputtering to remove particles, which are far from the normal direction [16]. A drawback of this technique is the significant deposition onto the collimators, which reduces the net deposition rate and limits the effective lifetime of the collimator.

An alternative to the filtering of sputtered metal atoms to enhance the net directionality of a metallic deposit is to ionize the majority of the sputtered atoms and form the film from metal ions. Ionized metal physical vapor deposition (IMPVD) is being used increasingly to deposit diffusion barriers and Cu seed layers onto high aspect ratio trenches [17-19]. In a typical IMPVD reactor shown in Fig. 1.5, a dc bias on the order of many 100s V applied to a magnetron target accelerates ions into the target with energies of several hundred eV. The plasma density below the target is enhanced by electrons that are confined there by the static magnetic field generated by the permanent magnet behind the magnetron. The large plasma density increases the ion flux to the target, and subsequently the sputtered metal atom flux. The metal atoms once thermalized are ionized by electron impact. The ions diffuse to the wafer region where they are collimated by the plasma sheath and directionally deposited.

To fill deep trenches and vias, ionized metal atoms are required due to the inability of neutral metal atoms to fill high aspect ratios. Neutral atoms tend to fill the top of the trenches first as they have a large spread in angles. This leaves voids in the trenches and consequently causes defects in the devices. The bias applied to the substrate narrows the angular distribution of the ions and enables ions to fill the bottom of the trench. The secondary plasma used to ionize the sputtered metal atoms is typically an inductively coupled plasma (ICP) [20-21]. The ICP is produced between the target and the substrate by a radio-frequency (rf) driven antenna, either

immersed in the plasma or placed outside. The inductively coupled system acts like a transformer. The rf coil acts as the primary coil, and the plasma acts as the secondary.

The plasma is usually sustained in an inert gas such as Ar at pressures on the order of 10s of mTorr to slow the sputtered atoms and ionize them (either by electron impact ionization or by charge exchange reaction) prior to their reaching the substrate. Typical ionization fractions of the metal are between 10 and 90%. An rf or dc bias may be applied to the substrate to vertically accelerate the metal ions into the wafer. The combination of anisotropic metal ions and isotropic neutral metal atoms results in conformal deposition.

There are several advantages to using an ICP as secondary plasma. The density of the reactor plasma and the ion energy can be separately controlled. The density of the ICP usually increases linearly with ICP power and can be easily controlled. In order to have sufficient sputtered atoms for deposition, the incident ion energy to the target needs to be several hundred eV. The substrate bias, however, needs to be high enough to vertically accelerate the ions, and low enough to prevent excessive resputtering of the deposited metal films due to energetic depositing ions. So the appropriate rf bias amplitude for the substrate is on the order of 10 V, much lower than the target bias. An ICP is a more efficient plasma source than a capacitively coupled plasma. The electron density increases linearly with ICP power, but increases only by the square root of the capacitive power. Hence, the ICP power is frequently used to generate high density plasmas ( $> 10^{11} \text{ cm}^{-3}$ ) in industrial applications.

Recently hollow-cathode magnetron (HCM) has been developed as a new promising IMPVD technology [22]. A schematic of a commercial HCM source is shown in Fig. 1.6. HCM relies on magnetic fields to generate high-density plasma within the volume of the cathode. There is a strong  $E \times B$  parallel to the surface of the target, which helps capture the secondary

electrons near the target surface, resulting in efficient sputtering of target material. HCM is different from a planar magnetron in that there is a high-density ( $n_e > 10^{11} \text{ cm}^{-3}$ ) plasma generated throughout the volume of the reactor. An rf bias can be additionally applied to increase the step coverage in high-aspect-ratio features. Klawuhn et al. noted that as rf bias power is increased, the step coverage transitions from increasing directionality resulting in higher bottom coverage, to increased bottom coverage and sidewall coverage due to a resputtering component, and finally, a large resputtering component [22]. The step coverage transition versus rf bias applied power for HCM-deposited Ti is shown in Fig. 1.7.

In IMPVD, the kinetic energy of sputtered metal atoms from the target is on the order of several electron volts, while the kinetic energy of the background gas atoms is less than 0.1 eV. In addition, the ions that are incident onto the target have energies on the order of 100s of eV and can be reflected as neutral atoms that have kinetic energies of several eV. Power transferred from the sputtered metal atoms and the reflected neutrals to gas atoms during collisions produces “sputter heating” and ultimately rarefaction of the gas. The rarefaction of the gas increases the mean free path of the metal atoms and ultimately limits the ionizing collisions of these metal atoms and their ionization fraction at high power loading. This gas heating and subsequent rarefaction have been observed in various experiments.

For example, in measurements in a magnetron using a directional pressure probe, Hoffman found that the gas density decreased by 10% at pressures on the order of 10 mTorr and currents of 12 A, an effect attributed to sputter heating [23]. Rosnagel measured gas pressures as a function of magnetron power in a magnetron reactor having a secondary ICP [24]. His results indicated that the gas density decreased by 40% while increasing magnetron power from 0.5 to 20 kW at an Ar pressure of 30 mTorr with 600 W ICP power and a Cu target, as shown in

Fig 1.8. Serikov and Nanbu developed a particle-in-cell/Monte Carlo model for gas heating in a dc discharge [25]. The gas temperature at the center of the discharge was 330 K and 460 K for discharge voltages of 300 V and 1500 V at 42 mTorr for the Al target, as shown in Fig. 1.9. As the target bias increases, sputter heating increases and the Ar temperature increases.

The greatest challenge in adopting a PVD approach to Cu seed layer deposition is that of attaining sufficient side-wall coverage in small, high-aspect-ratio features. Deposition of a continuous, Cu seed layer of a critical thickness is the key to attaining void-free electrochemical deposition Cu fill of features. Insufficient Cu step coverage results in void formation in a dual damascene structure. Poor sidewall coverage can be compensated by increasing the PVD seed layer thickness. The usefulness of this approach is limited by the amount of Cu overhang at the top of features, which leads to formation of seams and keyholes during electroplating. Nonuniformity of both barrier and seed films is extremely important because it ultimately dictates the required deposition in the field necessary to attain the required barrier protection. Minimizing the barrier thickness deposited in the field reduces the amount of material that must be removed during Cu CMP, and minimizing the Cu seed deposited is necessary to minimize the overhang of Cu at the top of features.

### **1.3 Plasma Process Modeling**

As plasma processing systems have increased in complexity and cost, it has become prohibitive to develop new reactors by only physical experimentation. The development of plasma equipment models (PEMs) for investigating chemical, physical and engineering scaling issues for plasma processing has significantly advanced in recent years. Use of these models allows costly physical development and manufacturing to be reduced.

If the gas pressure is sufficiently high, collisional processes dominate the dynamics of the plasma. Fluid models are widely used to model such plasmas. One of the first 2-D models for rf discharges was developed by Tsai and Wu in 1990 [26]. Pitchford et al. also produced a 2-D numerical model demonstrating the effects of dc self-bias which compared well to experiments for parallel plate plasma systems [27]. Dalvie et al. also produced a drift-diffusion-based 2-D model and described the effects of enhanced ionization for large radii in parallel plate systems [28]. Lymberopoulos and Economou developed the first finite element model of a parallel plate system and demonstrated comparison to the Gaseous Electronics Conference (GEC) reference cell [29]. Recently, Panagopoulos et al. developed a three-dimensional (3-D) finite element fluid model for studying azimuthal symmetries and their effect on etch uniformity in ICPs [30].

Although the overall structures of plasma discharges are well characterized by fluid equations, they do not model the change in velocity distribution functions, and they are assumed to be Maxwellian. In the low-pressure regime, where the mean free path of the gas particles is commensurate with the dimensions of the reactor, fluid models become inaccurate, and noncontinuum models, typically the Particle-In-Cell Monte Carlo (PIC-MC) technique is used [31-32]. In this method, a number of pseudoparticles (on the order of  $10^6$ ) are released in the system, each pseudoparticle representing a large number of real particles (electrons, ions and neutrals). The movement and chemical reactions of the pseudoparticles are modeled by the Monte Carlo technique, and the plasma properties are obtained. The PIC-MC method is good at predicting energy distributions of particles, especially under non-equilibrium conditions. For example, Vahedi et al. obtained bi-Maxwellian electron distribution functions in an Ar rf discharge, as shown in Fig 1.10, agreeing well with experimental observations [33]. The PIC

method is also frequently used to model sputtering because the sputtered atoms generally have high kinetic energy and are not in equilibrium with the other neutral species in the plasma.

The PIC method is accurate, but computationally expensive. To reduce the computational cost associated with kinetic simulations but still retain some of their advantages, hybrid techniques- i.e., combinations of continuum simulations and kinetic simulations- have been developed. For example, Sommerer et al. used a hybrid method to simulate rf discharges, in which self-consistent fluid equations for electrons and ions were supplemented by particle models for electrons [34]. In this method, the electron-simulation particles were used only as “test particles” to evaluate the electron energy distribution functions, which are then used to determine various reaction rates and transport coefficients. The electron density was obtained by solving the electron fluid equations, thus allowing use of a very small number of electron-simulation particles. Porteous and Graves used an electron-fluid ion-particle method to study magnetically confined plasmas [35].

Modeling of plasma-surface interactions can facilitate better understanding of microscopic phenomena taking place on the substrate. To this end, equipment scale models are typically linked to feature scale models to predict the evolution of the properties of microelectronic features. One method of topography modeling, described as the “string” or “geometric” method, involves solving partial differential equations. For example, SPEEDIE, a string model developed by Ulacia and McVittie, has been used to examine etching and deposition related to metallization processes in VLSI fabrication [36].

Monte Carlo methods are also used widely in modeling feature profile evolution. One of the advantages of using particle models instead of continuum models is that microstructures of deposited films may be taken into consideration. May et al. developed a sputter etch model for

argon impinging on silicon showing the effects of ion angular distribution on trench undercutting [37]. Recently Lu et al. developed an integrated plasma equipment model and feature scale model to simulate trench filling using IMPVD [38]. The model self-consistently accounts for the magnitude, angular distribution, and the energy distribution of the incident metal flux. They observed that high pressure, low magnetron power, and high ICP power are the operating conditions that maximize ionization fraction, and consequently trench filling.

#### **1.4 Summary**

High-density, low-pressure plasma reactors are gaining increasing currency to meet the stringent requirements of microelectronics fabrication. Plasma equipment models are being developed with the goals of both investigating basic physical processes and for use in the design of plasma equipment. The transport in low-pressure plasmas is highly nonequilibrium and a kinetic approach is warranted. In this work, a hybrid modeling approach has been developed in which the ion and neutral temperatures are kinetically derived and implemented in fluid equations to improve the capability to better address low-pressure plasma reactors.

The computational platform for this study is the Hybrid Plasma Equipment Model (HPEM). The modules of the HPEM and the physics therein are explained in Chapter 2. In Chapter 3, the Monte Carlo Feature Profile Model (MCFPM) used for the profile simulations is explained in detail. Nonequilibrium transport at low pressures is modeled using the Ion/Neutral Monte Carlo Simulation (IMCS), and is described in Chapter 4. The transport coefficients and temperatures computed using IMCS are then implemented in the fluid equations in the HPEM. A comparison of the plasma properties obtained using the fluid equations and the ion/neutral

Monte Carlo simulation has been performed. IMPVD is modeled at the reactor and feature scale and the results are presented in Chapter 5.

## 1.5 References

- [1] M. A. Lieberman and A. J. Lichtenberg, *Principles of Plasma Discharges and Materials Processing* (John Wiley & Sons, New York, 1994).
- [2] D. Manos and D. Flamm, *Plasma Etching* (Academic Press, San Diego, 1989).
- [3] B. N. Chapman, *Glow Discharge Processes* (John Wiley & Sons, New York, 1980).
- [4] S. J. Choi, P. L. G. Ventzek, R. J. Hoekstra, and M. J. Kushner, *Plasma Sources Sci. Technol.* **3**, 418 (1994).
- [5] M. Aoyagi, M. Maezawa, H. Nakagawa, and I. Kurosawa, *IEEE Trans. Appl. Superconductivity* **7**, 2644 (1997).
- [6] N. Fujiwara, S. Ogino, T. Maruyama, and M. Yoneda, *Plasma Sources Sci. Technol.* **5**, 126 (1996).
- [7] G. D. Conway, A. J. Perry, and R. W. Boswell, *Plasma Sources Sci. Technol.* **7**, 337 (1998).
- [8] T. P. Schneider, W. W. Dostalick, A. D. Springfield, and R. Kraft, *Plasma Sources Sci. Technol.* **8**, 397 (1999).
- [9] M. S. Barnes, J. C. Foster, and J. H. Keller, *Appl. Phys. Lett.* **62**, 2622 (1993).
- [10] J. R. Woodworth, M. E. Riley, P. A. Riley, and G. A. Hebner, *J. Appl. Phys.* **81**, 5950 (1997).
- [11] Intel research in Si, <http://www.intel.com/research/silicon/mooreslaw.htm>.
- [12] K. Lee, *Solid State Technol.* **41**, 85 (1998).
- [13] J. Hopwood, *Phys. Plasmas* **5**, 1624 (1998).
- [14] Fred Huang, Motorola (private communications, 2003).

- [15] T. J. Licata, E. G. Colgan, J. M. E. Harper, and S. E. Luce, *IBM J. Res. Develop.* **39**, 419 (1995).
- [16] S. M. Rossnagel, D. Mikalsen, H. Kinoshita, and J. J. Cuomo, *J. Vac. Sci. Technol. A* **9**, 261 (1991).
- [17] S. M. Rossnagel, *Semicond. Int.* **21** 99 (1996).
- [18] J. Hopwood, *Phys. Plasmas* **5** 1624 (1998).
- [19] C. Ryu, H. Lee, K. W. Kwon, A. L. S. Loke, and S. S. Wong, *Solid State Technol.* **42** 53 (1999).
- [20] M. Yamashita, *J. Vac. Sci. Technol. A* **7**, 151 (1989).
- [21] S. M. Rossnagel and J. Hopwood, *J. Vac. Sci. Technol. B* **12**, 449 (1994).
- [22] E. Klawuhn, G. C. D'Cuoto, K. A. Ashtiani, P. Rymer, M. A. Biberger, and K. B. Levy, *J. Vac. Sci. Technol. A* **18**, 1546 (2000).
- [23] D. W. Hoffman, *J. Vac. Sci. Technol. A* **3**, 561 (1985).
- [24] S. M. Rossnagel and J. Hopwood, *J. Vac. Sci. Technol. B* **16**, 3008 (1998).
- [25] V. V. Serikov and K. Nanbu, *J. Appl. Phys.* **82**, 5948 (1997).
- [26] J. H. Tsai and C. Wu, *Phys. Rev. A* **41**, 5626 (1990).
- [27] J. P. Boeuf and L. C. Pitchford, *Phys. Rev. E* **61**, 1376 (1995).
- [28] M. Dalvie, M. Surendra, and G. S. Selwyn, *Appl. Phys. Lett.* **62**, 3207 (1993).
- [29] D. P. Lymberopoulos and D. J. Economou, *Appl. Phys. Lett.* **63**, 2478 (1993).
- [30] T. Panagopoulos, D. Kim, V. Midha, and D. Economou, *J. Appl. Phys.* **91**, 2687 (2002).
- [31] C. K. Birdsall, *IEEE Trans. Plasma Sci.* **19**, 65 (1991).
- [32] M. Surendra and D. B. Graves, *IEEE Trans. Plasma Sci.* **19**, 144 (1991).
- [33] V. Vahedi, G. DiPeso, C. K. Birdsall, M. A. Lieberman, and T. D. Rognlien, *Plasma Sources Sci. Technol.* **2**, 273 (1993).
- [34] T. J. Sommerer and M. J. Kushner, *J. Appl. Phys.* **71**, 1654 (1992).

- [35] R. K. Porteous and D. B. Graves, IEEE Trans. Plasma Sci. **19**, 204 (1991).
- [36] J. I. Ulacia F. and J. P. McVittie, J. Appl. Phys. **65**, 1484 (1989).
- [37] T. S. Cale, G. B. Raupp, and T. H. Gandy, J. Appl. Phys. **68**, 3645 (1990).
- [38] P. W. May, D. F. Klemperer, and D. Field, J. Appl. Phys. **73**, 1634 (1993).
- [39] J. Lu and M. J. Kushner, J. Vac. Sci. Technol. A **19** 2652 (2001).

## 1.6 Figures

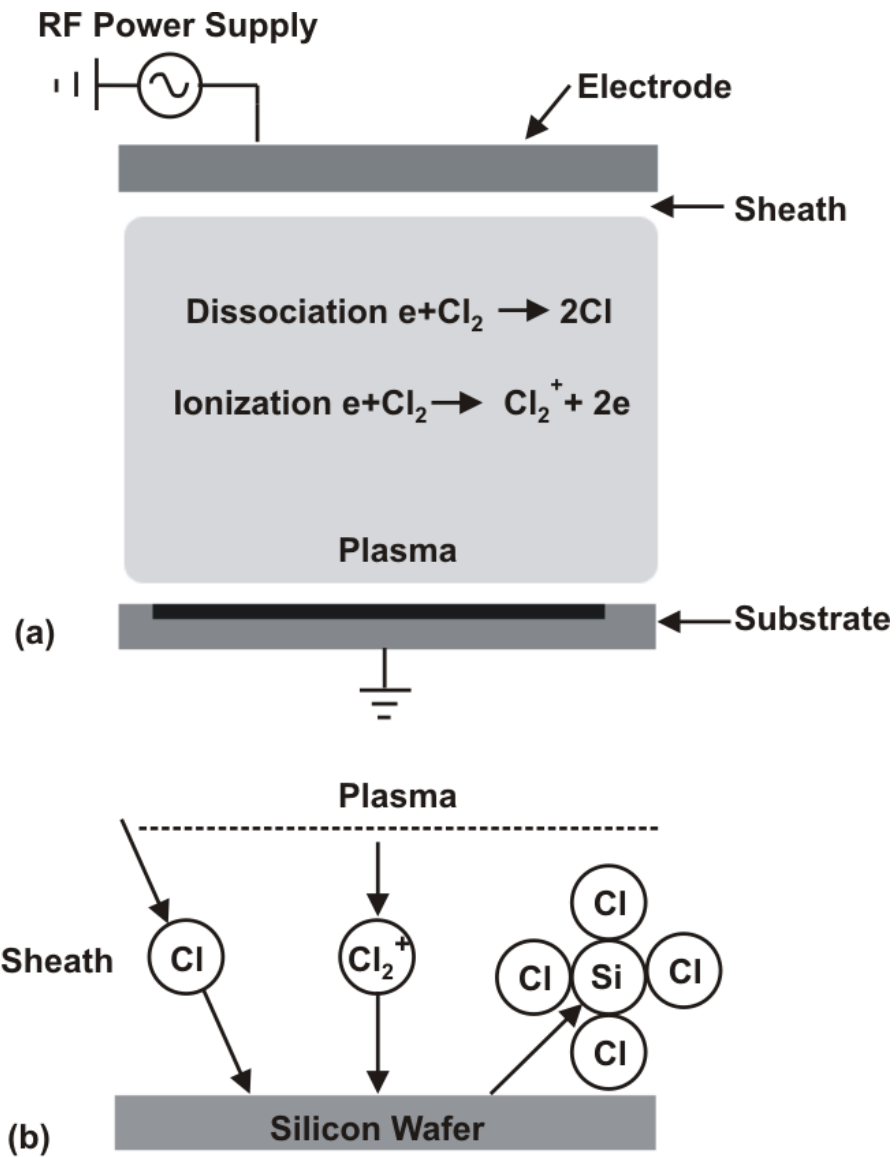


Fig. 1.1. Silicon etching with chlorine in a capacitively coupled plasma reactor. (a)  $\text{Cl}_2^+$  and  $\text{Cl}$  radicals are generated by electron impact of gas molecules, and (b) Ions accelerate in the sheath and etch the wafer to yield  $\text{SiCl}_4$ .

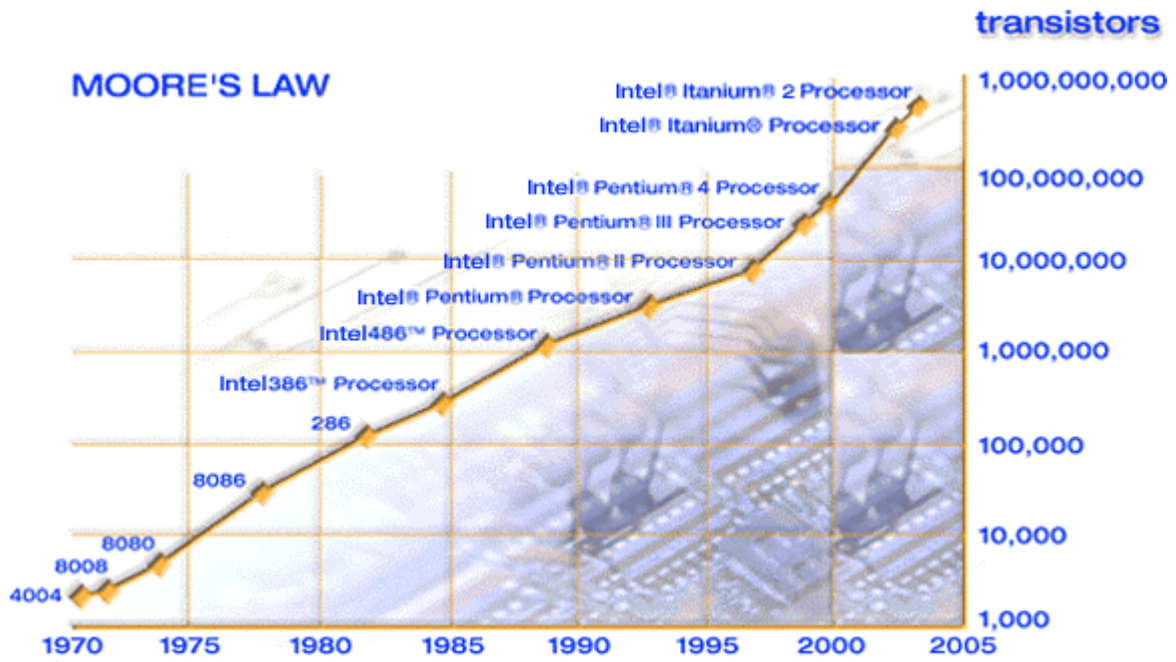


Fig. 1.2. Graphical depiction of Moore's law [11].

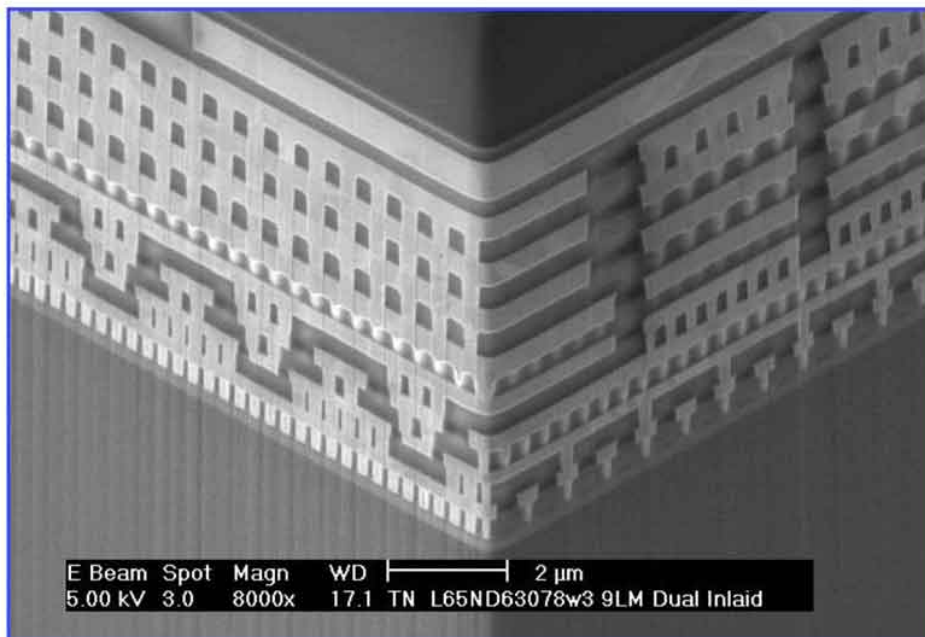


Fig. 1.3. Nine level copper interconnects with low-k ILD [14].

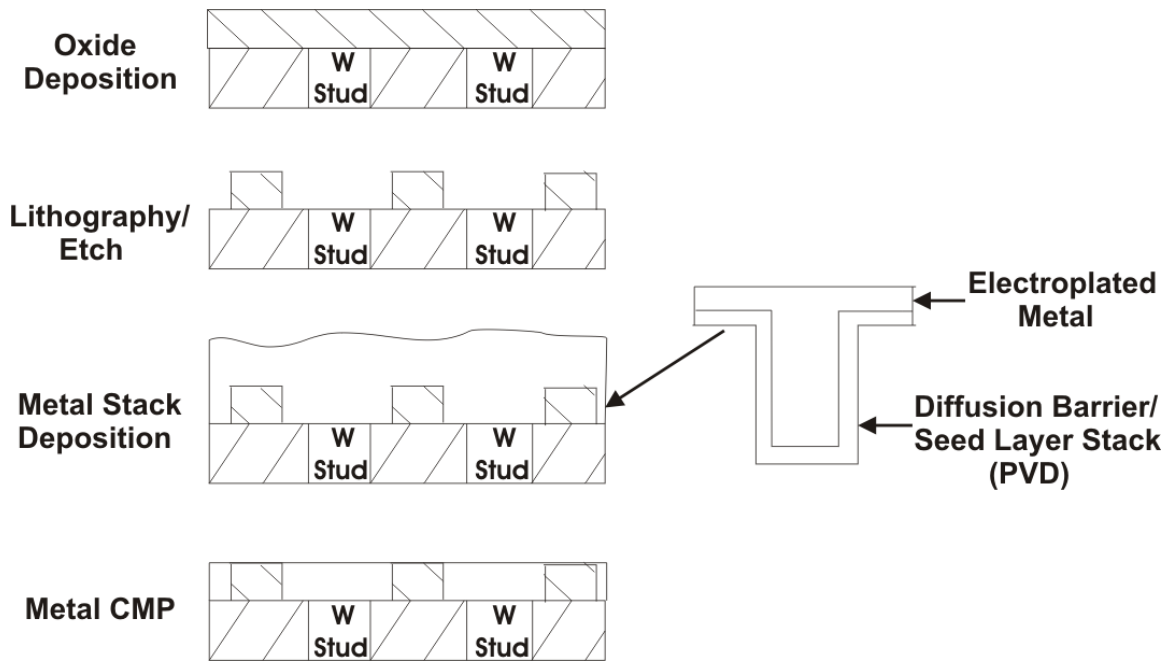


Fig. 1.4. Process steps for forming damascene wiring.

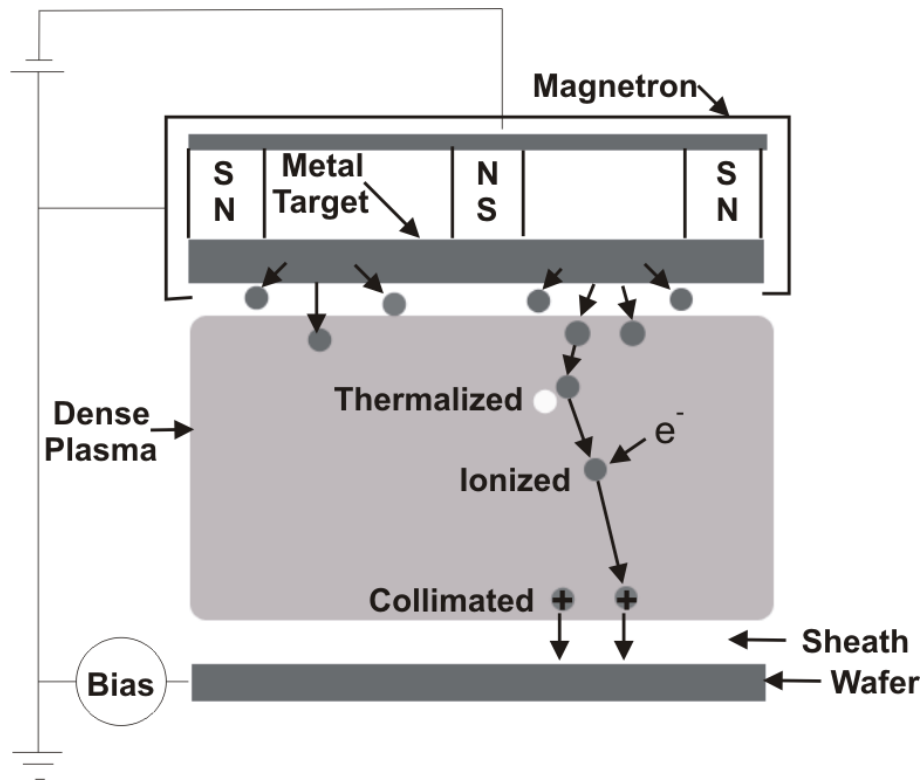


Fig. 1.5. Schematic of an IMPVD reactor showing ionization of metal atoms in an ICP.

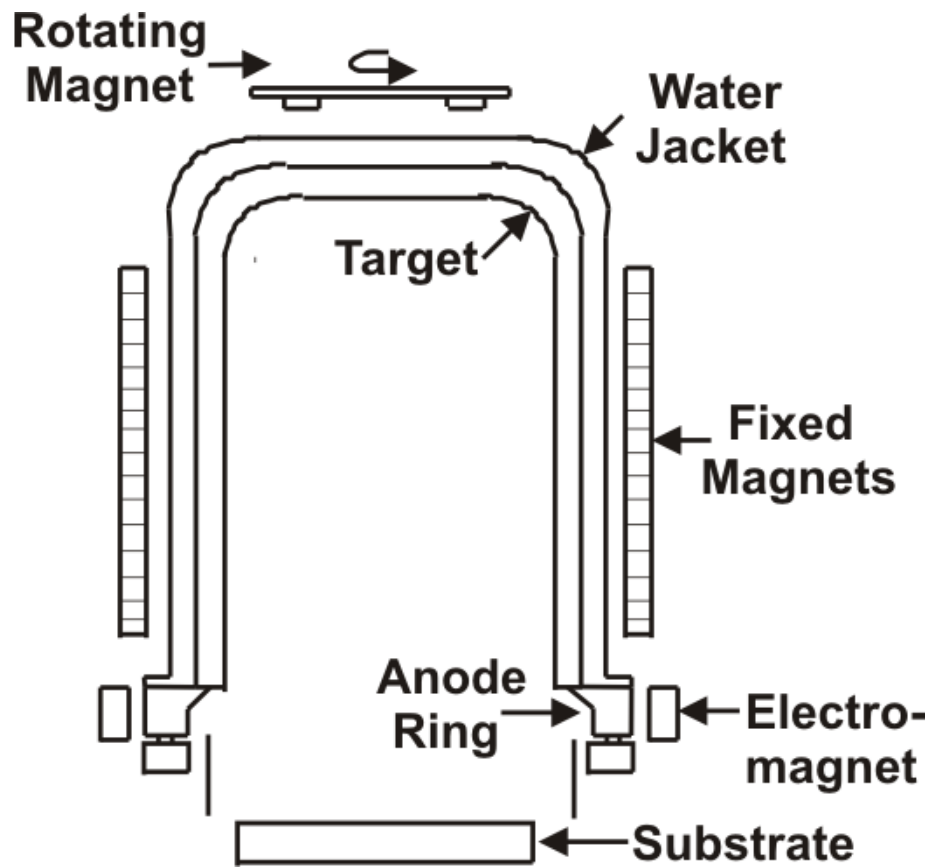


Fig. 1.6. Schematic of the HCM ionized PVD source and its components.

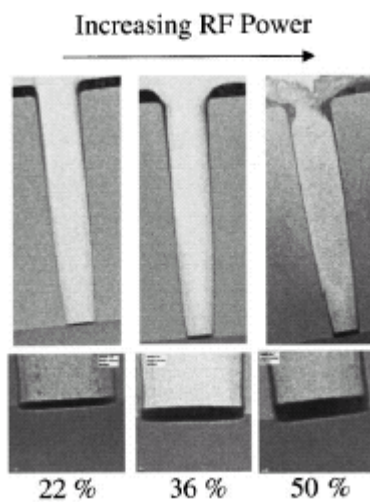


Fig. 1.7. HCM Ti bottom coverage vs applied table rf bias [22].

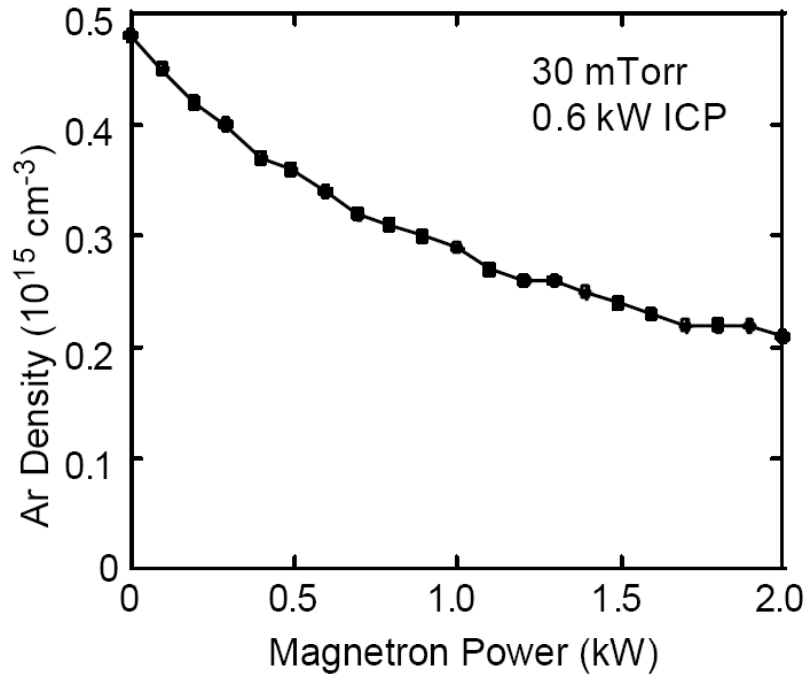


Fig. 1.8. Measured Ar density as a function of magnetron power at 30 mTorr and 0.6 kW ICP power. The Ar density decreases with magnetron power due to sputter heating [24].

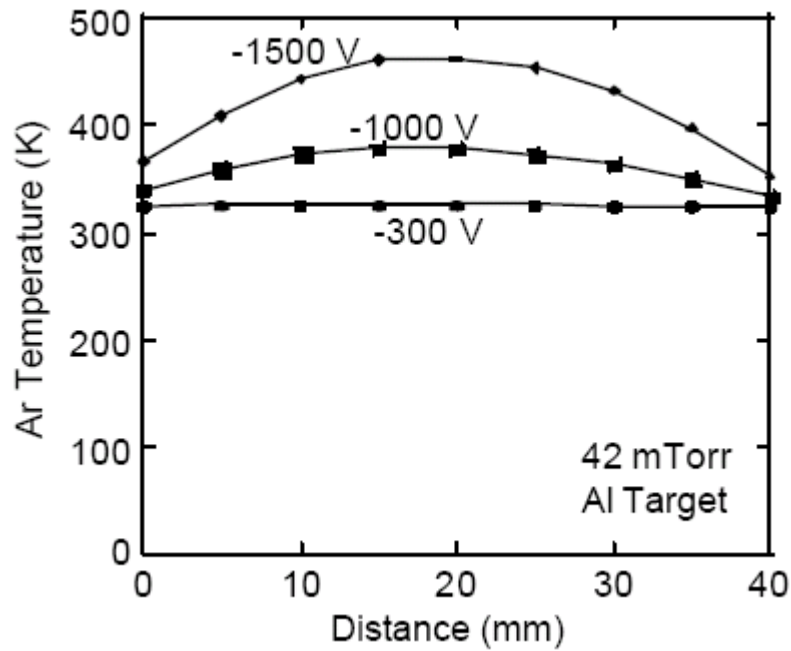


Fig. 1.9. Ar temperature as a function of distance from the Al target at 42 mTorr and three target biases. As the target bias increases, sputter heating increases and the Ar temperature increases [25].

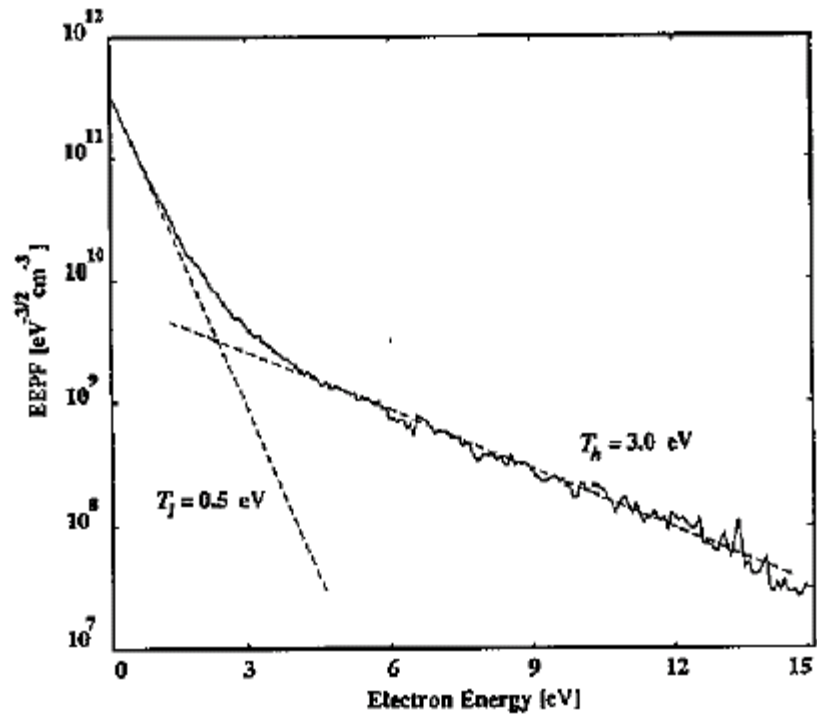


Fig. 1.10. The electron energy probability function (EEPF) in a 2 cm gap current-driven RF discharge at a gas pressure of 100 mTorr. The broken lines represent the two-temperature Maxwellian distribution of the discharge [33].

## **CHAPTER 2**

# **HYBRID PLASMA EQUIPMENT MODEL**

### **2.1 Introduction**

The HPEM has been developed at the University of Illinois for simulating low-temperature, low-pressure plasma processes [1-6]. The HPEM addresses plasma physics and chemistry in a modular fashion. There is a series of modules captured in three main blocks: The Electromagnetics Module (EMM), the Electron Energy Transport Module (EETM), and the Fluid-Chemical Kinetics Module (FKM). Starting with an initial guess of plasma properties, the EMM computes the inductively coupled electric fields determined by inductive coils, and the magnetostatic fields induced by permanent magnets or dc current loops. These fields are then passed to the EETM. Together with a database describing electron collision cross sections, the EETM calculates electron kinetic properties such as electron energy distribution function, electron temperature, and electron impact rate coefficients. Results of the EETM are transferred to the FKM to determine plasma source and sink terms. The FKM solves the fluid continuity equations for species densities and plasma conductivity. Electrostatic fields are also derived in the FKM by either solving Poisson's equation or assuming quasi-neutrality. The outputs of the FKM are then fed back to the EMM and EETM modules. The whole process iterates until the results reach a preset convergence criterion.

### **2.2 The Electromagnetics Module**

The EMM computes time-varying electric and magnetic fields for the HPEM. For an inductively coupled plasma, RF currents passing through the inductive coil generate azimuthal electric fields that are governed by Maxwell's equations. The EMM module calculates the

spatially dependent azimuthal electric fields by solving Maxwell's equation under time harmonic conditions. Assuming azimuthal symmetry, Maxwell's equation for electric field is reduced to

$$-\nabla \cdot \frac{1}{\mu} \nabla E_\phi = \omega^2 \varepsilon E_\phi - j\omega J_\phi \quad (2.1)$$

where  $\mu$  is the permeability,  $\varepsilon$  is the permittivity,  $\omega$  is the driving frequency, and the current  $J_\phi$  is the sum of the driving current  $J_o$  and the conduction current in the plasma. The conduction current is assumed to be of the form  $J_c = \sigma E_\phi$ . At pressures where the electrons are sufficiently collisional, the conductivity of the plasma is

$$\sigma = \frac{q_e^2 n_e}{m_e} \frac{1}{\nu_{me} + i\omega} \quad (2.2)$$

where  $q$  is the charge,  $n_e$  is the electron density,  $m$  is the mass, and  $\nu_m$  is the momentum transfer collision frequency. The azimuthal electric field solution is determined by the iterative method of successive over relaxation (SOR). The weighting coefficient and the convergence criterion for the SOR are adjustable simulation parameters.

The static magnetic fields in the axial and radial directions are also determined in the EMM. Assuming azimuthal symmetry allows the magnetic field to be represented by a vector potential  $A$  with only an azimuthal component.  $A$  can be solved using

$$\nabla \times \frac{1}{\mu} \nabla \times A = j, \quad B = \nabla \times A \quad (2.3)$$

where  $j$  is the source term due to closed current loops at mesh points representing permanent magnets or dc coils. This equation is also solved using SOR.

### 2.3 The Electron Energy Transport Module

Free electrons are accelerated to high energies by the electric fields. These electrons then inelastically collide with neutrals, leading to neutral dissociation, excitation, and ionization. The electron impact reaction rates strongly depend on the electron temperature  $T_e$ , which is related to the electron energy distribution (EED) as

$$T_e = \frac{2}{3} \int f(\varepsilon) \varepsilon d\varepsilon \quad (2.4)$$

where  $\varepsilon$  represents electron energy and  $f(\varepsilon)$  is the electron energy distribution. Inelastic collisions influence the EED by extracting energy from the electrons, resulting in a reduction of the high-energy tail of the EED. So for a collisional plasma, the EED does not behave as a Maxwellian. The EETM was designed to simulate these effects. There are two methods for determining these parameters. The first method determines the electron temperature by solving the electron energy conservation equation in the electron energy equation module (EEEM). The second method uses a Monte Carlo simulation to launch electron particles and collect statistics to generate the EEDF.

### 2.3.1 Electron energy equation method

For a plasma with weak interparticle collisions, the Boltzmann equation describes its kinetics:

$$\frac{\partial f_e}{\partial t} + v \cdot \nabla_r f_e - \frac{e(E + v \times B)}{m_e} \cdot \nabla_v f_e = \left( \frac{\delta f_e}{\delta t} \right)_{\text{collision}} \quad (2.5)$$

where  $f_e = f_e(t, r, v)$  is the electron distribution function,  $\nabla_r$  is the spatial gradient,  $\nabla_v$  is the velocity gradient,  $m_e$  is the electron mass, and  $\left( \frac{\delta f_e}{\delta t} \right)_{\text{collision}}$  represents the effect of collisions. The EEEM solves the zero-dimensional equation for a range of  $E/N$  (electric field divided by total gas density). The electron temperature and all its dependent quantities, like electron mobility and electron rate coefficients, are derived from the EED. This information is used in the solution of the electron energy equation

$$\nabla k \nabla T_e + \nabla \cdot (\Gamma T_e) = P_{\text{heating}} - P_{\text{loss}} \quad (2.6)$$

where  $k$  is the thermal conductivity,  $\Gamma$  is the electron flux determined by the FKM,  $T_e$  is the electron temperature, and  $P_{\text{heating}}$  is the power added due to conductive heating equal to  $j \cdot E$ . The current density and electric field are determined in the FKM. The electric field is the sum of the azimuthal field from the EMM and the radial and axial field found in the FKM.  $P_{\text{loss}}$  is the power loss due to collisions by the electrons.

### 2.3.2 Electron Monte Carlo simulation

The EMCS tracks the trajectories of electron pseudo particles in the electromagnetic fields obtained from the EMM module and the electrostatic fields obtained from the FKM. Statistics on electron energy distributions are gathered by tracking the particle motions and collisions. Initially, the electrons are given a Maxwellian distribution and randomly distributed in the reactor weighted by the current electron density. Particle trajectories are computed using the Lorentz equation:

$$\frac{d\bar{v}}{dt} = \frac{q_e}{m_e} (\bar{E} + \bar{v} \times \bar{B}) \quad (2.7)$$

where  $\bar{v}$ ,  $\bar{E}$ , and  $\bar{B}$  are the electron velocity, local electric field, and magnetic field, respectively. Equation (2.7) is updated using a second-order predictor corrector method. The electron energy range is divided into discrete energy bins. Within an energy bin, the collision frequency  $\nu_i$  is computed by summing all the possible collisions within the energy range,

$$\nu_i = \left( \frac{2\varepsilon_i}{m_e} \right)^{\frac{1}{2}} \sum_{j,k} \sigma_{ijk} N_j \quad (2.8)$$

where  $\varepsilon_i$  is the average energy within the bin,  $\sigma_{ijk}$  is the cross section at energy  $i$  for species  $j$  and collision process  $k$ , and  $N_j$  is the number density of species  $j$ . The free-flight time is randomly determined from the maximum collision frequency. After the free flight, the type of collision is determined by the energy of the pseudoparticle. The corresponding energy bin is referenced and

a collision is randomly selected from that energy bin, with a null reaction making up the difference between the maximum and actual collision frequency. Finally, the electron temperature, collision frequency, and electron impact rate coefficients are evaluated based on EEDs with the process cross section at the specified location.

## 2.4 The Fluid-Chemical Kinetics Module

In the FKM, fluid equations, together with chemical reactions, are solved to obtain plasma species, densities and fluxes. The FKM also computes electrostatic fields by either solving Poisson's equation or using an ambipolar field approximation.

The continuity equation that describes the density evolution rate for any species is

$$\frac{\partial N_i}{\partial t} = -\nabla \cdot \Gamma_i + S_i \quad (2.9)$$

where  $N_i$ ,  $\Gamma_i$ , and  $S_i$  are the species density, flux, and source for species  $i$ . The flux for each species can be determined by using a drift diffusion or a heavy body momentum equation. Electron densities are determined using the drift diffusion formulation,

$$\Gamma_i = \mu_i q_i N_i \bar{E}_s - D_i \nabla N_i \quad (2.10)$$

where  $\mu_i$  is the mobility of species  $i$ ,  $D_i$  is the diffusion coefficient,  $q_i$  is the species charge in units of elementary charge, and  $E_s$  is the electrostatic field. Alternately, the Scharfetter Gummel technique is used. Heavy ion and neutral fluxes can be determined by using the previous drift diffusion method or by using the heavy body momentum equation:

$$\frac{\partial \Gamma_i}{\partial t} = -\frac{1}{m_i} \nabla(N_i k T_i) - \nabla \cdot (N_i \bar{v}_i \bar{v}_i) + \frac{q_i}{m_i} N_i \bar{E} - \sum_j \frac{m_j}{m_i + m_j} N_i N_j (\bar{v}_i - \bar{v}_j) \nu_{ij} \quad (2.11)$$

where  $T_i$  is the species temperature,  $\bar{v}_i$  is the species velocity given by  $\Gamma_i / N_i$ , and  $\nu_{ij}$  is the collision frequency between species  $i$  and species  $j$ .

The gas and ion temperatures are determined from the energy equation for each species:

$$\begin{aligned} \frac{\partial N_i c_v T_i}{\partial t} = & \nabla \cdot \kappa_i \nabla T_i - P_i \nabla \cdot \bar{v}_i - \nabla \cdot (\bar{\phi}_i \varepsilon_i) + \frac{N_i q_i^2}{m_i \nu_i} E_s^2 + \frac{N_i q_i^2 \nu_i}{m_i (\nu_i^2 + \omega^2)} E^2 \\ & + \sum_j 3 \frac{m_{ij}}{m_i + m_j} N_i N_j R_{ij} k (T_j - T_i) \end{aligned} \quad (2.12)$$

where  $N_i$  is the density of species  $i$ ,  $c_v$  is specific heat,  $T_i$  is the species temperature,  $\kappa_i$  is the thermal conductivity of species  $i$ ,  $P_i$  is the partial pressure of species  $i$ ,  $\bar{v}_i$  is the species velocity,  $\bar{\phi}_i$  is the flux of species  $i$ ,  $\varepsilon_i$  is the internal energy of species  $i$ ,  $E_s$  is the electrostatic field,  $E$  is the RF field,  $m_i$  is the mass of species  $i$ ,  $m_{ij}$  is the reduced mass,  $\nu_i$  is the momentum transfer collision frequency for species  $i$ , and  $R_{ij}$  is the collision frequency for the collision process between species  $i$  and  $j$ .

In the FKM, the process of solving the continuity equation is coupled with the derivation of electrostatic fields. These fields determine the drift flux terms used in the continuity equation. There are two alternative ways for the FKM to calculate the electrostatic fields. The first option is to directly solve Poisson's equation. The time evolving electrostatic potential is related to the net charge density as

$$\nabla \cdot \varepsilon \nabla \Phi = -\rho \quad (2.13)$$

where  $\varepsilon$  is the permittivity,  $\Phi$  is the electrostatic potential, and  $\rho$  is the net charge density. The charge density is numerically estimated using a first-order Taylor series expansion:

$$\rho^{t+\Delta t} = \rho^t + \Delta t \cdot \left. \frac{\partial \rho}{\partial t} \right|^{t+\Delta t} \quad (2.14)$$

where  $\rho^t$  is the charge density at time  $t$  and  $\rho^{t+\Delta t}$  is the charge density at time  $t + \Delta t$ . The evolution rate of the charge density  $\frac{\partial \rho}{\partial t}$  is determined by the gradient of the total current density

$j$ :

$$\frac{\partial \rho}{\partial t} = -\nabla \cdot j + S \quad (2.15)$$

where  $S$  is the source function of charges. In the plasma region,  $j = \sum_i q_i (-D_i \nabla n_i + q_i n_i \mu_i (-\nabla \Phi))$ ; in materials,  $j = \sigma (-\nabla \Phi)$  where  $\sigma$  is the material conductivity.

The second option is to compute electrostatic fields using a quasi-neutrality approximation over the entire plasma region. Under such an assumption, the electron density is equal to the total ion charge density at all locations. At steady state, this requires that

$$-\nabla \cdot \Gamma_e + S_e = \sum_i q_i (-\nabla \cdot \Gamma_i + S_i) \quad (2.16)$$

or

$$\nabla \cdot (\mu_e n_e \nabla \Phi + D_e \nabla n_e) + S_e = \sum_i q_i (\nabla \cdot (-\mu_i n_i \nabla \Phi + D_i \nabla n_i) + S_i) \quad (2.17)$$

when using drift-diffusion equations for both electrons and ions.  $S_e$  and  $S_i$  represent electron and ion source functions, respectively.

## 2.5 Sputter Module

The sputtering and transport of metal atoms in the plasma are modeled using Monte Carlo techniques and is based on the work of Lu et al [7]. The source terms for the sputtered metal species are obtained and used to calculate the densities and fluxes of the metal species. Ion-energy dependent yields of sputtered atoms are obtained from a semi-empirical relationship whose parameters are determined from experimental data [8,9]. The kinetic energy of the emitted atoms is given by Thompson's theory of atomic collision cascades [10] for incoming ions of moderate energy (on the order of 100 eV). The normalized cascade distribution is [11-12]

$$F(E) = \begin{cases} 2 \left( 1 + \frac{U_s}{\Lambda E_i} \right)^2 \frac{U_s E}{(U_s + E)^3} & \text{for } E \leq \Lambda E_i. \\ 0 & \text{for } E > \Lambda E_i \end{cases} \quad (2.18)$$

where  $E$  is the kinetic energy of the sputtered atom,  $\Lambda E_i$  is the maximum recoil energy, and  $\Lambda = 4M_i M_t / (M_i + M_t)$ . The Thompson distribution peaks at half the surface binding energy. Due to the high-energy tail of the distribution, the average energy of the sputtered atoms is generally several eV. Under the operating conditions of interest, the sheath thickness is small compared to the ion mean free path, the dc sheath at the target is essentially collisionless. Hence the kinetic energy of the incoming ion is roughly equal to the sheath potential, which is computed in the semianalytical sheath model [13].

The energies of the reflected Ar neutral atoms from  $\text{Ar}^+$  incident on surfaces are obtained from TRIM simulations as a function of ion energy [14,15]. The average energy of the reflected Ar neutrals is curve-fitted into a thermal accommodation coefficient as a function of incident ion energy,

$$\alpha_T = \frac{E_i - E_r}{E_i - E_T} \quad (2.19)$$

where  $E_r$  is the kinetic energy of the reflected neutrals, and  $E_T$  is the kinetic energy of the reflected neutrals in thermal equilibrium with the target at 350 K. Under typical operating conditions,  $\alpha \approx 0.95$ . Since the energy distribution of the reflected neutrals is not monoenergetic, but also has a thermal component, it was assumed that 90% of the incident Ar ions are reflected with energy  $E_r$  and 10% are reflected thermally. The transport of reflected neutrals in the background gas is modeled in the same manner as the sputtered atoms.

A Monte Carlo simulation handles the transport of the sputtered and reflected atoms, where they are represented by computational pseudoparticles. Each pseudoparticle carries a

“weighting” which is used to determine its contributions to momenta, energy, and density in collisions with bulk gas atoms. The weighting of the  $i^{th}$  sputtered atom is

$$W_i = \frac{Y(E_i(\vec{r}))\Phi(\vec{r})A(\vec{r})}{N(\vec{r})V(\vec{r}')} \quad (2.20)$$

where  $Y$  is the energy-dependent yield of the target,  $E_i(\vec{r})$  is the incident ion energy at target location  $\vec{r}$ ,  $\Phi$  is the flux of ion and fast neutrals to the target (fast neutrals and ions of the same energy are considered equivalent with respect to sputtering),  $N$  is the number of Monte Carlo released from that location, and  $A$  is the surface area of the computational cell on the target. The term  $V$  is the volume of the computational cell at  $\vec{r}$  where the collision occurs.

The sputtered and reflected neutral atoms are emitted from the target surface with a cosine distribution in angle. Monte Carlo techniques are then used to follow the trajectories of the emitted atoms [16]. The mean free path of the sputtered atom is determined using null collision techniques [17] to account for spatially dependent gas properties (density and composition) that may occur as a consequence of both rarefaction and slowing of sputtered atoms.

Statistics are collected on the velocities of Monte Carlo particles before and after collisions to determine the net momentum and thermal energy transfer to the gas. The rate of change in momentum for the background gas atom (denoted by subscript  $g$ ) after the collision is

$$\frac{d}{dt}(n_g \Delta \vec{v}_g) = \frac{Wm_s}{m_g}(\vec{v}_s' - \vec{v}_s) \quad (2.21)$$

where  $\vec{v}_s$  is the velocity after the collision,  $\vec{v}'_s$  is its velocity before the collision,  $m$  is the mass of the atoms, subscript  $s$  denotes sputtered atoms, and  $W$  is the appropriate weighting for the sputtered atoms. The change in the background gas velocity is averaged over all collisions with the sputtered atoms, and the contribution is added as a source term to the momentum equation for the bulk fluid.

When the reactor pressure is low enough that the mean free path of the sputtered and reflected neutrals is comparable to the distance between the target and the substrate, the densities of the nonthermal (in-flight) species can be larger than those of thermal species. Under such conditions, electron impact excitation and ionization of the in-flight species become important. This mechanism is especially important in ionized hollow cathode magnetron sputtering devices, which typically operate below 10 mTorr. A probability array is constructed for collisions between the energetic neutrals and other species, including electrons. Since the momentum transferred to the gas atom during an electron impact is small, the pseudoparticle retains its original velocity following elastic and excitation electron collisions, and the particle is tracked until it thermalizes or strikes a surface. The rates of thermalization of neutral species are recorded into source terms for incorporation into the fluid continuity equations. For electron impact collisions producing ions, the pseudoparticles are removed from the sputter calculation. Ion source terms are generated at the location of ionization and incorporated into the fluid continuity equations. Due to the strong electrostatic forces in the plasma, the ions rapidly equilibrate with the bulk ions. The trajectories of the in-flight metal atoms are recorded to obtain the in-flight species densities.

## 2.6 Plasma Chemistry Monte Carlo Module

The energy and angular distributions of reactive species to the substrate are obtained using the Plasma Chemistry Monte Carlo Module [18]. The PCMCM calculates the trajectories of plasma species in the gas phase and their collisions with surfaces. The PCMCM is typically executed at the end of the HPEM after species densities, fluxes, and electrical properties have converged. Based on these quantities, a rate of generation of species  $i$  as a function of position,  $G_i(\vec{r})(cm^{-3}s^{-1})$  is computed based on all sources of species  $i$  on the right-hand side of reactions in the mechanism and on surfaces due to sputtering. A consumption rate  $C_i(\vec{r})(cm^{-3}s^{-1})$  is computed based on all reactions containing species  $i$  on the left-hand side of reactions in the mechanism. A local elastic collision frequency with each species is also computed. These elastic frequencies are added to the local consumption frequency  $C_i(\vec{r})\Delta V(\vec{r})$  ( $\Delta V(\vec{r})$  is the volume of computational cell at location  $\vec{r}$ ) to yield a total interaction frequency  $\nu_T(\vec{r})$ . Null collision techniques are used at each spatial location to provide a reactorwide collision frequency  $\nu_i$  for each species  $i$ .

Pseudoparticles of species  $i$  are launched from each computational cell at a time randomly chosen in the rf cycle with a weighting (or total number) proportional to  $G_i(\vec{r})\Delta V(\vec{r})$ . The velocity is randomly chosen from a Maxwell-Boltzmann distribution having a local temperature  $T_i(\vec{r})$  for volumetric sources where the spatially dependent temperature for each species is computed by HPEM. For sputter sources from surfaces, the pseudoparticle velocity is determined by the energy and identity of incident ion. The trajectories of the pseudoparticles are integrated for the time

$$\Delta t = -\frac{1}{v_i} \ln(r), \quad (2.22)$$

where  $\Delta t$  is the time step for movement of the pseudoparticle and  $r$  is a random number distributed on (0,1). For ions, acceleration by the local electric field is accounted for. In the case of sputtered species having initial energies of a few eV, additional considerations, such as in-flight electron impact excitation, are accounted for. The time step used to increment the trajectory is limited by the time required to cross a specified fraction of the cell. For ions, additional constraints are applied including a specified fraction of the sheath width (typically 0.01).

At the end of the time step, Monte Carlo techniques are used to determine if the collision is real or null. If real, another random number is used to determine if the collision is elastic or consuming. The particle is removed from the simulation if the collision is a consuming one. If elastic, the collision partner is identified using another random number and the velocity of the pseudoparticle is changed appropriately using standard elastic collision frequencies. If an ion undergoes a charge exchange collision, its identity is changed to the neutral counterpart and the trajectory is retained. The trajectories are advanced until the pseudoparticles reach the vicinity of a surface. If the surface is chosen as one for which statistics on incident species are desired, ions are then integrated through the sheath. For nonselected surfaces, the particles are removed from the simulation. A similar process is followed for the neutrals, except for integration through the sheath.

## 2.7 References

[1] P. L. G. Ventzek, R. J. Hoekstra, and M. J. Kushner, *J. Vac. Sci. Technol. B* **12**, 416 (1993).

- [2] W. Z. Collison and M. J. Kushner, *Appl. Phys. Lett.* **68**, 903 (1996).
- [3] M. J. Kushner, W. Z. Collison, M. J. Grapperhaus, J. P. Holland, and M. S. Barnes, *J. Appl. Phys.* **80**, 1337 (1996).
- [4] M. J. Grapperhaus and M. J. Kushner, *J. Appl. Phys.* **81**, 569 (1997).
- [5] S. Rauf and M. J. Kushner, *J. Appl. Phys.* **81**, 5966 (1997).
- [6] R. L. Kinder and M. J. Kushner, *J. Vac. Sci. Tech. A* **19**, 76 (2001).
- [7] J. Lu and M. J. Kushner, *J. Appl. Phys.* **89**, 878 (2001).
- [8] N. Masunami, Y. Yamamura, Y. Itikawa, N. Itoh, S. Kazumata, S. Miyagawa, K. Morita, R. Shimizu, and H. Tawara, *At. Data Nucl. Data Tables* **31**, 1 (1984).
- [9] Y. Yamamura, N. Matsunami, and N. Itoh, *Radiat. Eff.* **71**, 65 (1983).
- [10] M. W. Thompson, *Philos. Mag.* **18**, 377 (1968).
- [11] V. V. Serikov and K. Nanbu, *J. Vac. Sci. Technol. A* **14**, 3108 (1996).
- [12] M. A. Lieberman and A. J. Lichtenberg, *Principles of Plasma Discharges and Material Processing* (Wiley, New York 1994), p 253.
- [13] M. J. Grapperhaus and M. J. Kushner, *J. Appl. Phys.* **81**, 569 (1997).
- [14] D. N. Ruzic (private communication).
- [15] D. N. Ruzic, *Nucl. Instrum. Methods B* **47**, 118 (1990).
- [16] A. Bogaerts, M. van Straaten, and R. Gijbels, *J. Appl. Phys.* **77**, 1868 (1995).
- [17] M. J. Grapperhaus, Z. Krivokapic, and M. J. Kushner, *J. Appl. Phys.* **83**, 35 (1998).
- [18] R. J. Hoekstra, M. J. Grapperhaus, and M. J. Kushner, *J. Vac. Sci. Technol. A* **15**, 1913 (1997).

# **CHAPTER 3**

## **MONTE CARLO FEATURE PROFILE MODEL**

### **3.1 Introduction**

The Monte Carlo Feature Profile Model (MCFPM) is used for self-consistent determination of topographical feature evolution for semiconductor processing in plasma reactors [1-3]. The energy and angular distributions (EADs) produced by the Plasma Chemistry Monte Carlo Module in HPEM are used to simulate processes such as etching, stripping and deposition at different locations on the substrate.

### **3.2 Description of the Model**

The MCFPM resolves wafer features (masks, photoresists, semiconductors) on the submicron scale utilizing a rectilinear mesh. The mesh spacing is typically  $\approx 1 \times 1$  nm, which is  $\approx 4 \times 4$  or fewer atoms. Each cell is assigned a material identity (e.g., poly-Si, photoresist, SiO<sub>2</sub>, plasma), which may change during the simulation. Solid species, including adsorbates or passivation, are represented by the identity of the computational cell. Gas phase species (i.e., radicals and ions) are represented by computational pseudoparticles. Pseudo-particles are launched towards the surface from random locations above the trench with energies and angles sampled from the EADs obtained from the Plasma Chemistry Monte Carlo Module (PCMCM), which has described in detail in Chapter 2.

The pseudoparticles are launched with a frequency computed from the total flux of radicals or ions incident onto the substrate so that each pseudoparticle represents a fraction of the number of atoms in a mesh cell based on the gas-to-material weighting ratio. The pseudoparticle

trajectories are advanced in time where the calculation of position and velocity are separated allowing solution of two linear equations:

$$v_i = v_{i-1} + \frac{qE}{m} \Delta t \text{ and } x_i = x_{i-1} + v_i \Delta t \quad (3.1)$$

where  $v$  and  $x$  represent the velocity and position of the particle, and the subscripts indicate the former or current velocity and position;  $q$  and  $m$  indicate the charge and mass of the particle, respectively; and  $\Delta t$  indicates the time-step taken by the particle. This method is used because under the majority of cases the effects of charging are ignored and the electric field  $E$  is set to zero, allowing solution of the second linear equation only. At any instant of the particle's motion, the time step for its current move is determined by the time required to move the minimum distance to a surface or a fraction of the mesh cell size if its an ion.

The effects of surface charging on the profile evolution can be addressed. Electron trajectories can be simulated as low-temperature isotropic fluxes, which impinge upon the feature during the low-potential swing of the sheath. This macroscopically balances the current due to the ions. To resolve the electric fields due to the charged surfaces of the feature, an iterative explicit solution of Poisson's equation is determined utilizing successive overrelaxation (SOR).

$$\nabla \cdot \epsilon \nabla \phi^{t+\Delta t} = -\rho^t \quad (3.2)$$

SOR is used to accelerate solution by multiplying the calculated  $\Delta\phi$  by an overrelaxation factor greater than one. Neumann boundary conditions are used at the top and bottom of the feature by assuming that the electric field above the feature matches the sheath field from the Fluid Kinetics Module (FKM) and that the electric field below the feature is approximately zero. The left and right boundaries are assumed to follow a periodic Dirichlet condition.

The interaction of energetic particles with surface species is determined by the energy and angular distributions (EADs). The source of energetic particles is ions accelerated through the sheath, with energies of up to 100s eV and angular spreads  $<1-25^\circ$  from the vertical. In the model, ions neutralize upon interaction with the surface and the energetic neutrals thus formed have the same effect as energetic ions. Energetic particles can either specularly or diffusively reflect from surfaces, with an energy loss which is larger for diffusive scattering and small for specular.

A generalized reaction scheme for interaction of the ions and neutrals with the surface is used which allows for any reactant-product combination and energy dependence of reaction. The classes of reaction in the model include adsorption, passivation, ion activated etching, thermal etching, sputtering, ion or neutral reflection, and re-emission.

The reaction probability for a particle of energy  $E$  incident onto a surface at an angle  $\theta$  from the local vertical of the surface is [4,5]

$$p(\theta) = p_0 \left[ \frac{E^n - E_{th}^n}{E_r^n - E_{th}^n} \right] f(\theta) \quad (3.3)$$

where  $E_{th}$  is the threshold energy of the process,  $E_r$  is reference energy,  $p_0$  is the probability for normal incidence at  $E_r$  and  $f(\theta)$  is the relative probability at angle of incidence  $\theta$ .  $f(\theta)$  is an empirical function typical of chemically enhanced sputtering with a maximum value near  $\theta = 60^\circ$  [5].

The reflection of particles from surfaces was given both specular and diffusive character. To account for surface roughness on spatial scales not resolved by our model, we specified that a fraction  $f_d = 0.25$  was diffusively scattered. The energy of specularly reflected particle was scaled such that forward scattered particles retain the majority of their energy. The specularly reflected particle energy for incident energy  $E_I$  is

$$E_s(\theta) = E_I \left( \frac{E_I - E_c}{E_{ts} - E_c} \right) \left( \frac{\theta - \theta_c}{90^\circ - \theta_c} \right) \quad (3.4)$$

for  $\theta > \theta_c$ ,  $E_c < E_I < E_{ts}$ . Particles having  $\theta < \theta_c$  or  $E_I < E_c$  are said to diffusively scatter. Particles having  $E_I > E_{ts}$  are said to retain all of their energy subject to the angular correction. We used  $E_{ts} = 100$  eV,  $E_c = 0$  eV and  $\theta_c = 60^\circ$ . The final reflected energy of the particle is a weighted sum of the specularly reflected energy and diffusively reflected energy.

Surface diffusion is an important phenomenon, which significantly affects deposition profiles. In the absence of surface diffusion, one observes unphysical dendritic growth due to line-of-sight algorithm employed for sticking of incident species. The surface diffusion capability was incorporated in the MCFPM by Lu et al [3]. The depositing metal atoms are first physisorbed and are treated differently from the underlying material even if they have the same composition. The physisorbed atoms diffuse on the surface before they are chemisorbed onto the

underlying material. An adsorbed cell can diffuse into any unoccupied adjacent cell in the mesh. The probability that an adsorbed cell  $i$  moves to another cell  $j$  is dependent on their potential energy values, which are based on effective Morse potentials.

$$\Phi_{ij} = \Phi_0 \left\{ \exp\left(-2 \frac{r_{ij} - r_0}{a_0}\right) - 2 \exp\left(-\frac{r_{ij} - r_0}{a_0}\right) \right\} \quad (3.5)$$

where  $r_{ij}$  is the distance between the center of the cells.  $\Phi_0$  was set to 0.3 eV based on the predictions by Lu *et al* [3].  $r_0$  and  $a_0$  were set to 1.6 nm and 5 nm based on mesh scale lengths as opposed to atomic lengths. The probability of diffusion to all possible locations is summed and normalized. The final diffusion path is then chosen randomly. Based on the chosen value of the activation energy for diffusion from  $i$  to  $j$  ( $E_{ij}$ ), the adsorbed cell either chemisorbs or diffuses. The frequency of such trials is governed by the jump frequency  $\nu$ ,

$$\nu = -\nu_{ij} \ln(r) \quad (3.6)$$

where

$$\nu_{ij} = \nu_0 \exp\left(-\frac{E_{ij}}{k_b T_s}\right) \quad (3.7)$$

and

$$\nu_0 = 2k_b T_s/h \quad (3.8)$$

where  $h$  is the Planck's constant,  $k_b$  is the Boltzman's constant, and  $T_s$  is the substrate temperature. At 393 K,  $\nu_0 = 1.6 \times 10^{12} \text{ s}^{-1}$ . Based on the specified threshold jump frequency ( $\nu_t$ ), the cell chemisorbs if  $\nu < \nu_t$ .

### 3.3 Surface Reaction Mechanism for Cu IMPVD

Surface reaction mechanisms are an intrinsic property of the gas phase reactant species and are independent of the process conditions, such as the plasma source or the gas chemistry. The process conditions influence the energies and magnitudes of the incident reactant fluxes; however, the reaction mechanism should not change. For the purposes of modeling Cu seed layer deposition, the reaction mechanism developed by Lu et al. has been used and is listed in Appendix A [3]. The primary ions,  $\text{Ar}^+$  and  $\text{Cu}^+$ , sputter Cu and  $\text{SiO}_2$  surfaces with an energy dependence given by Eq. (3.5). The angular dependence of sputtering has energy dependence similar to chemically enhanced sputtering reaction with a maximum near  $\approx 60^\circ$ . In addition to sputtering, deposition also occurs with  $\text{Cu}^+$  bombardment. All ions not deposited are converted to hot neutrals at the surface and are treated similarly to ions in the reaction mechanism. Cu ground state and  $\text{Cu}^*$  [ $\text{Cu}(^2D_{5/2})$ ] deposit on  $\text{SiO}_2$  and Cu surfaces. The sticking probability of Cu and  $\text{Cu}^*$  was estimated to be 0.70 on  $\text{SiO}_2$  and 0.95 on Cu.

### 3.4 References.

- [1] R. J. Hoekstra, M. J. Grapperhaus, and M. J. Kushner, *J. Vac. Sci. Technol. A* **15**, 1913 (1997).
- [2] R. J. Hoekstra and M. J. Kushner, *J. Vac. Sci. Technol. B* **16**, 2102 (1998).
- [3] J. Lu and M. J. Kushner, *J. Vac. Sci. Technol. A* **19**, 2652 (2001).
- [4] C. C. Cheng, K. V. Guinn, V. M. Donnelly, and I. P. Herman, *J. Vac. Sci. Technol. A* **12**, 2630 (1994).
- [5] C. F. Abrams and D. B. Graves, *J. Appl. Phys.* **86**, 2263 (1999).

# CHAPTER 4

## ION/NEUTRAL MONTE CARLO SIMULATION

### 4.1 Introduction

Plasma simulations can be classified into three categories: fluid, kinetic, and hybrid. Fluid simulations integrate moments of the Boltzmann's equations describing species density, momentum, and energy conservation [1]. Kinetic simulations, such as Particle-In-Cell with Monte Carlo Simulations [2-3] (PIC-MCC) or Direct Simulation Monte Carlo [4-5] (DSMC) follow the motion of a number of superparticles accounting for their collisions using Monte Carlo techniques. They are more accurate than fluid simulations as they can be used at low pressures (mean free path comparable to or longer than the characteristic length scale) or for highly nonequilibrium situations. Kinetic simulations are computationally intensive compared to fluid simulations. Hybrid simulations [6-7] preserve the accuracy of kinetic simulations and are less expensive computationally. Although the overall structures of plasma discharges are well described by continuum equations, they do not necessarily account for changes in the velocity-distribution functions, as they are usually assumed to be Maxwellian. If the distribution functions are known, the equations should be valid even at low pressures. In this regard, a hybrid modeling approach has been developed in which the ion and neutral transport coefficients are kinetically derived and implemented in fluid equations.

In this work, a Monte Carlo simulation for ion and neutral transport (IMCS) has been developed and integrated with HPEM to improve the capabilities to address lower pressures. The ion/neutral energy distribution functions obtained from the IMCS are used to obtain transport coefficients for use in heavy particle momentum conservation equations. The consequences of

varying power, pressure, and gas chemistries have been investigated for several low-pressure tools and comparison has been made with experiments.

## 4.2 Description of the Model

The computational platform for this investigation is the Hybrid Plasma Equipment Model, which has been described in detail in Chapter 2. A schematic of the modular HPEM is shown in Fig. 4.1. The Electromagnetics Module (EMM) computes the inductively coupled electric fields and the magnetostatic fields. The Electron Energy Transport Module (EETM) uses these fields to calculate electron kinetic properties. The Fluid Kinetics Module (FKM) solves the fluid continuity equations for species densities and plasma conductivity. The electron impact source functions, and time and position dependent fields, and the advective flow field are exported to the Ion/Neutral Monte Carlo Simulation (IMCS). A schematic description of the IMCS is shown in Fig. 4.2. Pseudoparticles representing the ions and neutral species are launched during the rf cycle from locations weighted by the electron impact source functions obtained from the HPEM. The trajectories of the pseudoparticles are followed in a time dependent fashion using interpolated electric fields (position and phase). Surface reactions are represented by reactive sticking coefficients. Particle-mesh algorithms are used to represent ion-ion, ion-radical and radical-radical collisions. Statistics are collected during the flight of the pseudoparticles and transferred to the mesh. The species temperatures and transport coefficients are fed back to the FKM for updated computations. The whole process is iterated until results reach a preset convergence criterion.

Pseudoparticles for each species  $j$  are launched in the reactor in accordance with the spatial distribution of the electron impact source functions  $S_j(r, z)$  obtained from the HPEM.

Particles representing the injected species are also launched from inlets based on flow rates. The number of pseudoparticles of species  $j$  launched from a given computational cell centered on  $(r,z)$  having volume  $V(r,z)$  is

$$N_j(r,z) = N_t \frac{S_j(r,z)V(r,z)W_j(r,z)}{\int [\sum_i S_i(r,z)V(r,z)W_i(r,z)] d^3r} \quad (4.1)$$

where  $N_t$  is the total number of pseudoparticles being launched, the sum in the denominator over all the species being initialized, and  $W_i$  is the weighting function. The dynamic range of electron impact source functions may span many orders of magnitude. To launch a statistically relevant number of pseudoparticles, the number of particles launched from each cell is weighted by

$$W_j(r,z) = \frac{\log[S_j(r,z)]}{\log[S_m]} \quad (4.2)$$

where  $S_m$  is the maximum value of all electron impact source functions. The  $i^{\text{th}}$  particle of species  $j$  is then “tagged” as representing

$$m_{ij} = \frac{S_j(r,z)V_j(r,z)}{N_j(r,z)} \quad (4.3)$$

actual particles, with  $m_{ij}$  having units of  $s^{-1}$ . The pseudoparticles are launched with velocities

$$v(r,z) = v_t + v_a(r,z) \quad (4.4)$$

where  $v_t$  is a thermal velocity randomly selected from a Maxwell-Boltzmann distribution having the gas temperature, and a local advective velocity  $v_a$  obtained from the HPEM. Statistics on the volumetric densities  $N_j(r,z)$  of each species are then obtained by integrating the time each particle spends in a given computational cell.

Trajectories are advanced by direct integration of velocities between collisions. For neutral species, the trajectories are free flight. For ions, accelerations are included as specified by the local electric and magnetic fields. These fields are obtained by performing a three-dimensional interpolation ( $r$ ,  $z$ , and time during the rf phase) of the electric fields imported from the HPEM. The flight time is determined by

$$\Delta t = \min(\Delta t_r, \Delta t_z, \Delta t_c, \tau) \quad (4.5)$$

where  $\Delta t_r$  and  $\Delta t_z$  are the times to cross a specified fraction of the computational cell in the  $r$  and  $z$  directions,  $\Delta t_c$  is the time to the next collision, and  $\tau$  is a specified fraction of the rf cycle. The time to next collision for species  $j$  is

$$\Delta t_{col} = -\left(\sum_k v_{j,k}\right)^{-1} \ln(1-r) \quad (4.6)$$

where  $v_{j,k}$  is the collision frequency of species  $j$  for process  $k$  and  $r$  is a random number evenly distributed on (0,1). If a particle collides with a surface during a flight (which results in the

particle “appearing” in a solid) the point of intersection of the particle with the surface is back calculated. The particle is then placed at the surface.

Collision dynamics are accounted for by constructing probability arrays for each species  $j$ . The arrays are

$$P_{ij} = \frac{\sum_{m=1}^i k_{mj} N'_{mj}}{\sum_{m=1}^{i-\max} k_{mj} N'_{mj}} \quad (4.7)$$

where  $k_{ij}$  is the effective two-body rate coefficient for the  $i^{\text{th}}$  heavy particle collision of species  $j$  and  $N'_{ij}$  is the density of its collision partner. The prime indicates that the maximum density of the collision partner throughout the reactor is used to construct these arrays, thereby implementing a modified null cross section.

When a particle reaches the randomly selected time for a collision, the collision that occurs is determined by selection of another random number  $r$ . The collision, which occurs satisfies  $P_{i-1,j} < r \leq P_{i,j}$ . Given this choice of collision, the actual occurrence of the reaction is denoted by the choice of a third random number  $r$ ,

$$r \leq \frac{N_{ij}(r, z)}{N'_{ij}} \quad (4.8)$$

where  $N_{ij}(r, z)$  is the actual local density of the collision partner. This technique allows for null collisions to account for transport of the particle between locations having different densities of the collision partners.

If the collision is an identity changing collision, the particle characteristics are changed. In the case of thermal chemical reactions in the bulk plasma, the velocities of the products are randomly chosen from a Maxwell-Boltzmann distribution having the local gas temperature. For charge exchange collisions, the hot neutral retains the original ion's velocity. The rate coefficients for elastic collisions are calculated using Lennard-Jones parameters to simulate hard sphere collisions.

Surface reactions are included using reactive sticking coefficient  $r_s$ , which specifies the probability that the pseudoparticle reacts with the surface (and is removed from the gas phase). When a particle collides with the surface, a random number is chosen. If  $r \leq r_s$ , a reaction occurs. If the inequality does not hold, the particle is diffusively reflected from the surface with a speed randomly chosen from a Maxwell-Boltzmann distribution having the wall temperature. If the reaction occurs, a second random number is chosen to determine disposition of the particle in accordance with the surface reaction mechanism. The particles that are returned to the gas leave from the surface with polar angle based on a modified cosine or Lambertian distribution. In the case of ions, the neutralized particle is allowed to return to the plasma with a specified fraction of its incident energy, which allows for spectral scattering from the surface.

In general, species (electrons, ions, neutrals) transport can be described by the Boltzmann equation

$$\frac{\partial f(\vec{r}, \vec{v}, t)}{\partial t} + \mathbf{v} \cdot \nabla_r f(\vec{r}, \vec{v}, t) + \mathbf{a} \cdot \nabla_v f(\vec{r}, \vec{v}, t) = \frac{\delta f(\vec{r}, \vec{v}, t)}{\delta t} \quad (4.9)$$

where  $f$  is the velocity distribution,  $r$  is the spatial location,  $v$  is the velocity, and  $a$  is the acceleration. The right-hand side of Eq. 4.9 is the collision integral, which accounts for the effect

of collisions on the  $f$ . Kinetic simulations solve for the species distribution function by directly integrating the Boltzmann equation. The fluid equations are obtained by taking moments of the Boltzmann equation. The number density continuity equation is the zeroth moment of Boltzmann's equation:

$$\frac{\partial N_i}{\partial t} = -\nabla \cdot \Gamma_i + S_i \quad (4.10)$$

where  $N_i$ ,  $\Gamma_i$ , and  $S_i$  are the species density, flux, and source for species  $i$ . The flux for each species can be determined from the heavy body momentum equation, which is the first moment of Boltzmann's equation:

$$\frac{\partial \Gamma_i}{\partial t} = \frac{1}{m_i} \nabla (N_i k T_i) - \nabla \cdot (N_i \bar{v}_i \bar{v}_i) + \frac{q_i}{m_i} N_i \bar{E} - \sum_j \frac{m_j}{m_i + m_j} N_i N_j (\bar{v}_i - \bar{v}_j) \nu_{ij} \quad (4.11)$$

where  $T_i$  is the species temperature,  $v_i$  is the species velocity given by  $\Gamma_i/N_i$ , and  $\nu_{ij}$  is the collision frequency between species  $i$  and species  $j$ . The gas and ion temperatures are determined from the energy equation for each species,

$$\begin{aligned} \frac{\partial N_i c_v T_i}{\partial t} = & \nabla \cdot \kappa_i \nabla T_i - P_i \nabla \cdot \bar{v}_i - \nabla \cdot (\bar{\phi}_i \epsilon_i) + \frac{N_i q_i}{m_i v_i} E_s^2 + \frac{N_i q_i^2}{m_i v_i} E_s^2 + \\ & \frac{N_i q_i^2 v_i}{m_i (v_i^2 + \omega^2)} E^2 + \sum_j 3 \frac{m_j}{m_i + m_j} N_i N_j R_{ij} k (T_j - T_i) \end{aligned} \quad (4.12)$$

where  $N_i$  is the density of species  $i$ ,  $c_v$  is the specific heat,  $T_i$  is the species temperature,  $\kappa_i$  is the thermal conductivity of species  $i$ ,  $P_i$  is the partial pressure,  $v_i$  is the species velocity,  $\bar{\varphi}_i$  is the flux,  $\varepsilon_i$  is the internal energy,  $E_S$  is the electrostatic field,  $E$  is the rf field,  $m_i$  is the mass of species,  $m_{ij}$  is the reduced mass,  $\nu_l$  is the momentum transfer collision frequency, and  $R_{ij}$  is the collision frequency for the collision process between species  $i$  and  $j$ .

When the IMCS is used, gas phase statistics of the particle temperatures and collision frequencies are updated as the particles traverse the reactor using finite-sized particle techniques [8]. This is done by first finding the number of particles near a mesh point and then calculating the fraction of the particle's properties, which should be assigned to it. This is usually a function of the distance of a particle from that point. The temperatures computed using the IMCS are then used instead of the ones calculated using the energy equation. The collision frequencies and temperatures are additionally used in the momentum equation to compute the heavy particle fluxes. Using the fluid equations necessitates some assumptions regarding the species distribution functions, which may be invalid under nonequilibrium conditions. Use of the species distribution functions and transport coefficients obtained using the IMCS, extends the applicability of the fluid equations to lower pressures. If the distribution functions were exactly known, fluid equations would be valid under all conditions.

### 4.3 Validation

The model was validated by comparison with experiments performed by Hebner et al. [9] in a GEC reference cell reactor, schematically shown in Fig. 4.3. A five-turn planar coil couples inductive power to the chamber. The lower electrode was grounded and a pump port surrounds the lower electrode. Absorption spectroscopy was used to measure the temperature of neutrals.

Laser-induced fluorescence was used to confirm the neutral temperatures and to measure argon metastable ion temperatures. The gas phase reaction mechanism is given in Appendix B. A comparison of the Ar neutral temperatures as a function of pressure in the center of the discharge at a height 1.6 cm above the lower electrode is shown in Fig. 4.4(a). The temperatures predicted using the IMCS increase from 600 K to 1270 K as the pressure increased from 4 to 20 mTorr. This agrees well with the experimentally measured temperatures, which increased from 600 K to 1000 K. The temperatures obtained using the fluid model did not show appreciable change in this pressure regime and were approximately 400 K. In Ar plasmas, neutral-neutral collisions and ion-neutral collisions lead to exchange of energy between these species. The most important gas heating mechanism for Ar neutrals is symmetric charge exchange with energetic Ar<sup>+</sup> ions. The spatial distribution of temperature of Ar neutrals is shown in Fig. 4.4(b). The temperature peaks in the center of the reactor in agreement with experimental results. The higher plasma density in the center of the reactor results in a higher symmetric charge exchange rate, resulting in higher temperatures. For example, the Ar<sup>+</sup> density drops from  $3.0 \times 10^{11} \text{ cm}^{-3}$  in the center of the reactor to  $1.67 \times 10^{11} \text{ cm}^{-3}$  at  $r = 6 \text{ cm}$ . A comparison of the spatial distribution of Ar<sup>+</sup> ion temperatures is shown in Fig. 4.4(c). Ar<sup>+</sup> ions gain energy from the static electric fields. The large electric fields at the periphery of the reactor result in higher temperatures in those locations. For example, the radial electric field increases from 0.35 V/cm in the center of the reactor to 1.67 V/cm at  $r = 6 \text{ cm}$ . The IMCS results are a closer match to the experimentally observed trends than those obtained using the fluid model.

#### 4.4 Comparative Study of the IMCS and the Fluid Model

Parameterizations were performed in the ICP reactor geometry shown in Fig. 4.5. A three-turn coil couples inductive power to the reactor. The lower electrode is grounded and a pump port surrounds it. Temperatures computed using the IMCS and the fluid equations are compared in Figs. 4.6 and 4.7. The temperature of Ar neutrals peaks in the center of the reactor corresponding to the peak in Ar<sup>+</sup> density. Temperature of Ar<sup>+</sup> ions peaks at the periphery. The temperatures predicted by the IMCS are higher than those predicted using the fluid equations.

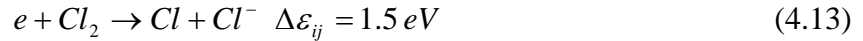
At a constant pressure, a higher Ar neutral temperature translates to a lower Ar density with the IMCS. For example, the temperature and density for Ar neutrals are 549 K and  $3.9 \times 10^{13} \text{ cm}^{-3}$ , respectively, when using the IMCS, and 344 K and  $5.7 \times 10^{13} \text{ cm}^{-3}$ , respectively when using fluid equations. The electron temperature is determined by the balance between the power deposited in electrons by the electric fields and the power loss due to collisions. The lower Ar density, when using the IMCS, in turn, translates into a lower electron-neutral collision frequency resulting in a higher electron temperature, as shown in Fig. 4.8. The electron temperatures peak near the coils and are 5.0 eV and 5.2 eV when using the fluid equations and the IMCS, respectively. The higher electron temperature results in more ionization, hence a higher Ar<sup>+</sup> density occurs on using the IMCS, as shown in Fig. 4.9. The peak Ar<sup>+</sup> densities are  $5.8 \times 10^{10} \text{ cm}^{-3}$  and  $8.8 \times 10^{10} \text{ cm}^{-3}$  when using the fluid equations and the IMCS, respectively. The flatter electron temperature profile in the center of the reactor, when using the IMCS, results in a flatter Ar<sup>+</sup> density profile in the center of the reactor. The higher Ar<sup>+</sup> densities when using the IMCS results in an increase in the charge exchange collision rate, which in turn results in even higher particle temperatures.

The consequences of power deposition the plasma properties were investigated. The base case conditions were Ar at 10 mTorr, and at a flow rate of 100 sccm. The temperature of Ar neutrals increases with power, as shown in Fig. 4.10. With the IMCS, the peak  $\text{Ar}^+$  density in the center of the reactor increases from  $2.1 \times 10^{10} \text{ cm}^{-3}$  at 100 W to  $6.2 \times 10^{10} \text{ cm}^{-3}$  at 300 W. The higher symmetric charge exchange rate results in a higher Ar neutral temperature at higher powers.  $T_{\text{Ar}^+}$  is mainly determined as a balance between the net heating by electrostatic fields and loss of energy through charge exchange collisions. The higher Ar neutral temperature, at higher powers results in a smaller Ar neutral density at constant pressure. The Ar neutral density in the center of the reactor decreases from  $1.5 \times 10^{14} \text{ cm}^{-3}$  to  $1.1 \times 10^{14} \text{ cm}^{-3}$  as the power increases from 100 to 300 W. The resulting reduction in charge exchange collisions is responsible for the higher  $T_{\text{Ar}^+}$  at higher powers. The temperatures predicted using the IMCS are higher than those predicted using the fluid equations.

The radially averaged Ar neutral energy distributions (NED) and ion energy distributions (IED) in the center of the reactor are shown for 100 W and 300 W, respectively in Fig. 4.11 and Fig. 4.12. The distributions are twin-sloped, indicating a bi-Maxwellian distribution. The high-energy tail in the NED corresponds to the energetic neutrals formed as a result of charge exchange collisions with more energetic ions. The high-energy tail of the distribution is overpopulated relative to a Maxwellian distribution. The fluid model, which assumes Maxwellian NED and IED, therefore underpredicts the particle temperatures.

The plasma properties in an Ar/ $\text{Cl}_2$  mixture were investigated. The gas phase reaction mechanism is given in Appendix C. The base case conditions were Ar /  $\text{Cl}_2$  = 80 / 20 mixture at 10 mTorr, a flow rate of 100 sccm, and an ICP power deposition of 300 W. The temperatures of Cl and  $\text{Cl}_2$  neutrals are shown in Fig. 4.13. In molecular gases, which undergo electron impact

dissociation, such as chlorine, the Franck-Condon effect is an important additional heating source. The Franck-Condon effect occurs when an electron strikes a neutral molecule with sufficient energy to raise the molecule to a dissociative state. This energy is generally greater than the dissociation energy, which results in the dissociated fragments acquiring extra energy. Franck Condon (FC) heating was included for [10]



A higher symmetric charge exchange rate causes the neutral temperatures to peak in the center of the reactor. The Cl and Cl<sub>2</sub> NED are shown in Fig. 4.14. The distributions are non-Maxwellian with significant overpopulation of the high-energy tail relative to a Maxwellian distribution. Consequently, the temperatures predicted by the IMCS are higher than those predicted using fluid equations. The temperature of Cl neutrals is higher than that of Cl<sub>2</sub> because of a higher charge exchange collision frequency and the Franck-Condon effect. The Cl<sup>+</sup> ion density was compared at different pressures for a constant power deposition of 300 W. When using fluid equations, [Cl<sup>+</sup>] increases with increase in pressure. With the IMCS, [Cl<sup>+</sup>] decreases with increase in pressure, as shown in Fig. 4.15(a). Hebner et al. used laser-induced fluorescence to measure metastable chlorine ion densities in a modified GEC reference reactor [11]. They also observed that the density of Cl<sup>+</sup>\* decreased substantially as the pressure was increased from 7 to 40 mTorr. The [Cl<sub>2</sub><sup>+</sup>] density increases with pressure when using either the IMCS or the fluid equations as shown in Fig. 4.15(b). This behavior is ultimately linked to the electron density, which increases with pressure when using fluid equations, but shows a decreasing trend

when using the IMCS, as shown in Fig. 4.16(a). The plasma properties for an Ar/Cl<sub>2</sub> = 80/20 discharge at 2 and 20 mTorr when using fluid equations and the IMCS are compared in Table 4.1. The rate of generation of electrons depends on the gas density and electron temperature. When using the fluid equations, the increase in neutral densities with pressure offsets the decrease in electron temperature. As a result, electron densities increase with pressure. However, when using the IMCS, the higher neutral temperatures predicted result in smaller neutral densities. The higher electron temperatures do not offset this decrease in neutral densities and as a result, electron densities decrease with increasing pressure.

When using the IMCS, a lower electron density, at higher pressure, results in a lower production of Cl (alternately, lower dissociation of Cl<sub>2</sub>) as shown in Fig. 4.16(b), and consequently a smaller [Cl<sup>+</sup>] density. When using the IMCS, [Cl<sub>2</sub><sup>+</sup>] increases with pressure because of the reduced dissociation of Cl<sub>2</sub>. The higher electron density, when using fluid equations, compensates for the increased dissociation of Cl<sub>2</sub>, and consequently [Cl<sub>2</sub><sup>+</sup>] increases with pressure.

Ionized metal physical vapor deposition is increasingly being used to deposit diffusion barriers and Cu seed layers onto high aspect ratio trenches. In a typical IMPVD reactor shown in Fig. 4.17, a dc bias applied to the magnetron target accelerates ions into the target, causing sputtering. A secondary plasma, generated using an rf driven antenna, ionizes the sputtered material as it moves towards the substrate. The base case conditions were Ar at 10 mTorr, an ICP power of 1 kW, and a magnetron power of 300 W. The temperatures of Ar ions and neutrals obtained using the IMCS and the fluid equations are shown in Figs. 4.17 and 4.18. When using the IMCS, the Ar neutral temperature peaks in the center of the reactor, because of higher collisional heating in that region. The Ar neutral temperature profile obtained using fluid

equations is significantly different exhibiting peaks near the target surface and the substrate. The ion temperatures peak in the sheath regions at the periphery of the reactor and near the coils due to the larger electric fields in those regions.

The disparity in the mobilities of electrons and ions results in sheaths developing adjacent to surfaces exposed to the plasma. The higher ion temperatures, when using the IMCS, result in a smaller voltage drop across the sheath. The dc bias is  $-55$  V when using the IMCS, and  $-58$  V when using the fluid equations. The reduced acceleration of ions, when using the IMCS, results in less sputtering. Consequently, the nonthermal Cu densities are smaller when using the IMCS, as shown in Fig. 4.19. The peak nonthermal Cu densities at the target surface are  $1.9 \times 10^{11} \text{ cm}^{-3}$  and  $1.6 \times 10^{11} \text{ cm}^{-3}$  when using the fluid equations and the IMCS respectively. The non-thermal Cu fluxes incident on the substrate are  $3.5 \times 10^{15} \text{ cm}^{-2}\text{s}^{-1}$  and  $4.1 \times 10^{15} \text{ cm}^{-2}\text{s}^{-1}$  when using the fluid equations and the IMCS, respectively. The neutral temperatures predicted using the IMCS are higher than those predicted using fluid equations, and consequently the neutral densities are lower at a given pressure. The less collisional plasma, when using the IMCS, results in fewer thermalizing collisions as the Cu travels from the target to the substrate.

#### **4.5 Summary**

A hybrid modeling approach has been developed in which the ion and neutral temperatures are kinetically derived and implemented in fluid equations, thereby extending their applicability to low-pressure systems. An ion/neutral Monte Carlo simulation has been developed to obtain transport coefficients and temperatures for use in the fluid equations. A comparison of the temperatures obtained using the fluid equations and the ion/neutral Monte Carlo simulation has been done. The species temperatures significantly affect the plasma

properties such as densities, electron temperatures, and sputter rates. Obtaining the right species temperatures and distribution functions is therefore imperative to better model plasma processing systems. The consequences of varying power, pressure, and gas chemistries have been investigated for several low-pressure tools and comparison has been made with experiments.

#### 4.6 References

- [1] E. Gogolides, H. H. Sawin, J. Appl. Phys. **72**, 3971 (1992).
- [2] C. K. Birdsall, IEEE Trans. Plasma Sci. **19**, 65 (1991).
- [3] V. Vahedi, G. DiPeso, C. K. Birdsall, M. D. Lieberman, and T. D. Ronglien, Plasma Sources Sci. Technol. **2**, 261 (1993).
- [4] D. J. Economou, T. Bartel, R. S. Wise, and D. P. Lymberopoulos, IEEE Trans. Plasma Sci. **23**, 581 (1995).
- [5] M. D. Kilgore, H. M. Wu, and D. B. Graves, J. Vac. Sci. Technol. B **12** 494 (1994).
- [6] P. L. G. Ventzek, T. J. Sommerer, R. J. Hoekstra, and M. J. Kushner, Appl. Phys. Lett. **62**, 3247 (1993).
- [7] R. L. Kinder and M. J. Kushner, J. Vac. Sci. Tech. A **19**, 76 (2001).
- [8] K. Birdsall and A. B. Langdon, *Plasma Physics via Computer Simulation* (McGraw Hill, New York, 1985).
- [9] G. A. Hebner, J. Appl. Phys. **80**, 2624 (1996).
- [10] J. D. Bukowski, D. B. Graves, and P. Vitello, J. Appl. Phys. **80**, 2614 (1996).
- [11] G. A. Hebner, J. Appl. Phys. **80**, 3215 (1996).

## 4.7 Tables

Table 4.1. Plasma Properties in an Ar / Cl<sub>2</sub> (80:20) discharge (300 W, 100 sccm).

Pressure (mTorr)		T <sub>Ar</sub> (K)	[Ar] (cm <sup>-3</sup> )	T <sub>e</sub> (eV)	n <sub>e</sub> (cm <sup>-3</sup> )
2	FLUID	345	$4.3 \times 10^{13}$	4.32	$5.4 \times 10^{10}$
	IMCS	642	$3.3 \times 10^{13}$	4.75	$7.6 \times 10^{10}$
20	FLUID	382	$4.0 \times 10^{14}$	2.84	$8.0 \times 10^{10}$
	IMCS	764	$1.8 \times 10^{14}$	3.15	$5.1 \times 10^{10}$

## 4.8 Figures

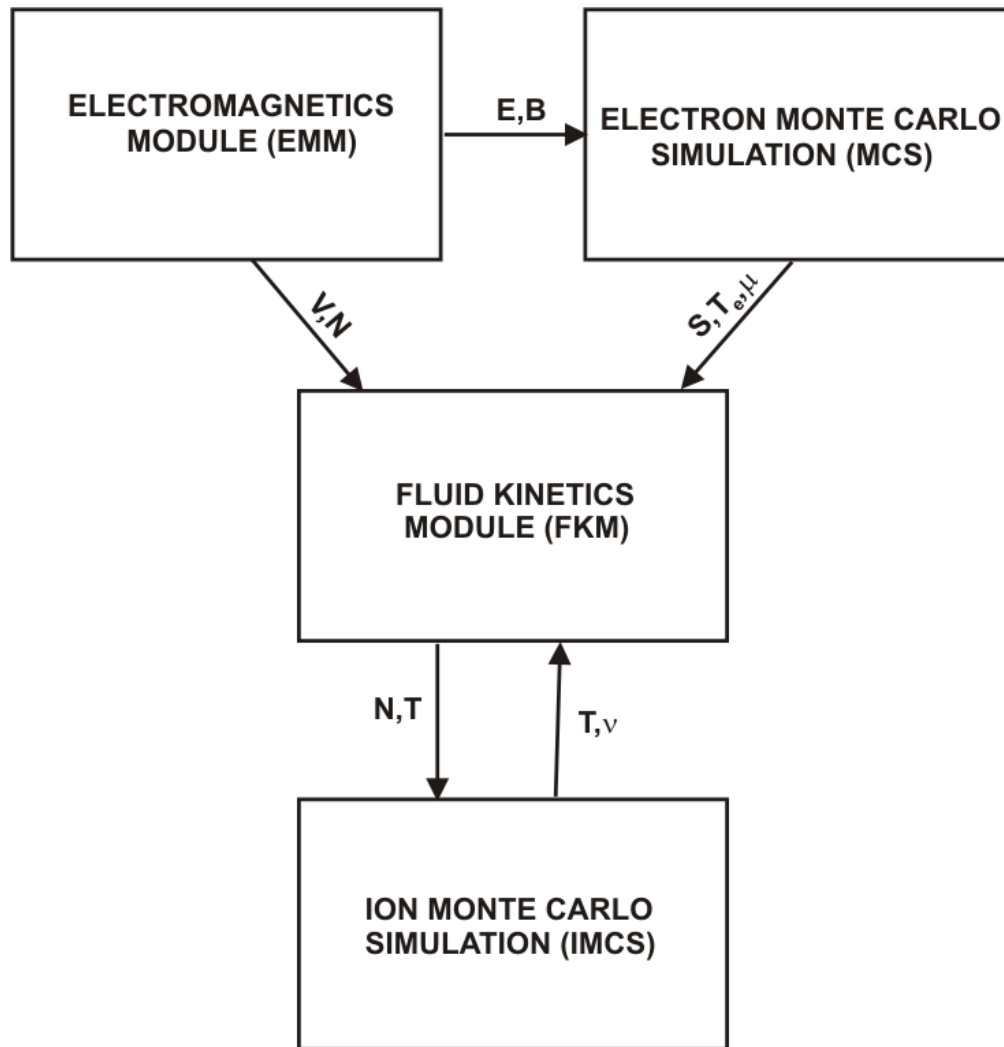


Fig. 4.1. Schematic of the modular Hybrid Plasma Equipment Model (HPEM).



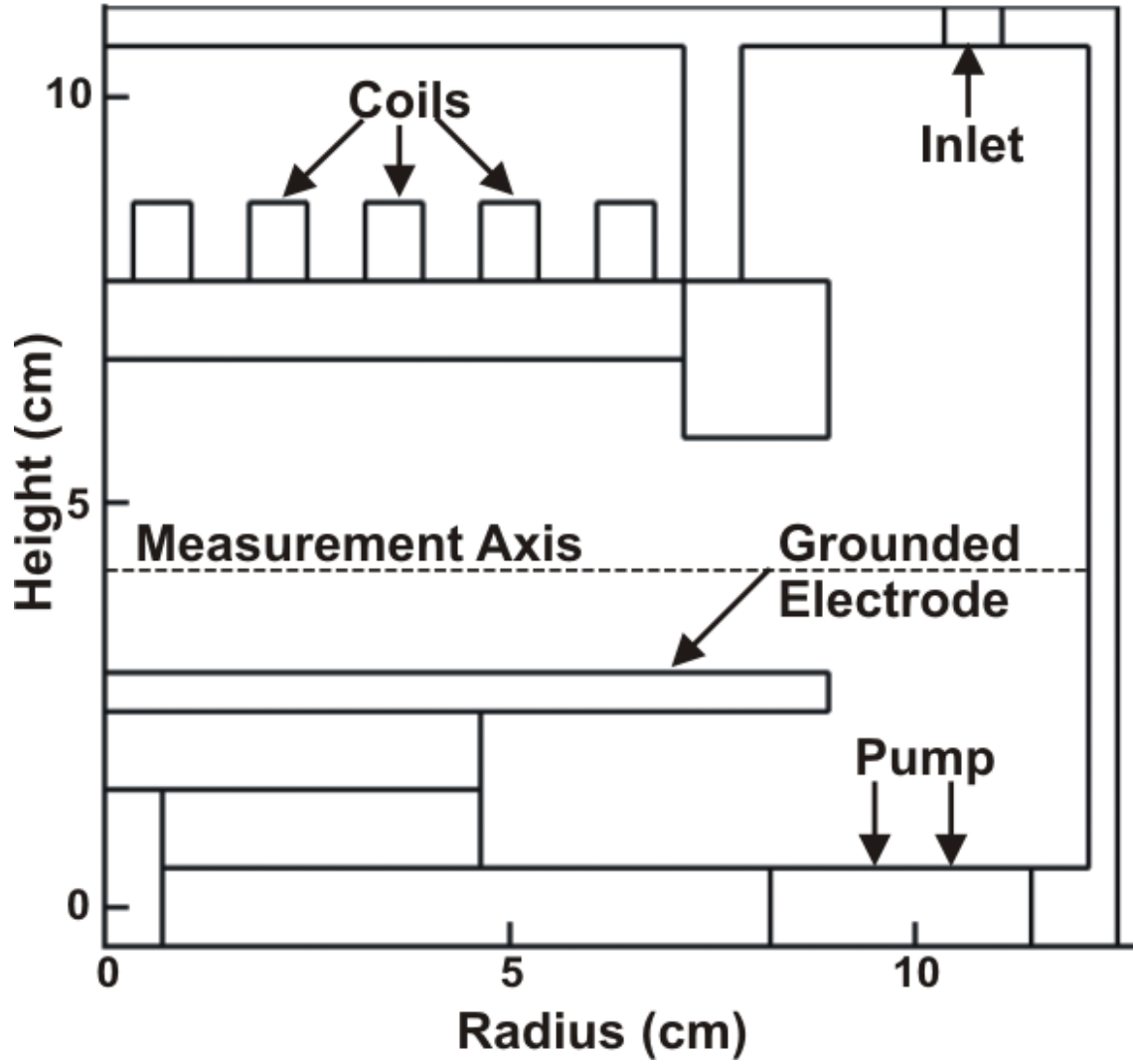


Fig. 4.3. Schematic of the modified GEC reference cell reactor used in the simulations for comparison with experiments. The measurement axis is 1.6 cm above the lower grounded electrode.

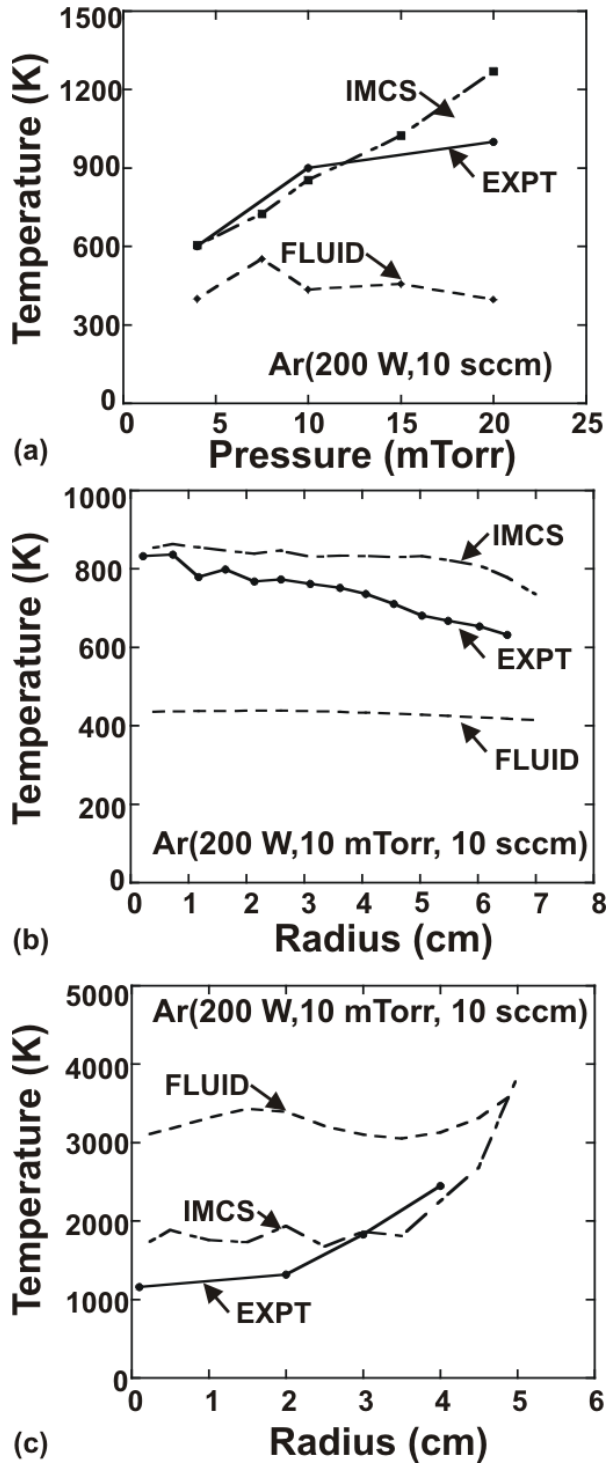


Fig. 4.4. Comparison of neutral and ion temperatures obtained using the fluid model and the IMCS in an Ar discharge (10 sccm, 200 W). (a) Ar neutral temperatures as a function of pressure, (b) Ar neutral temperatures at 10 mTorr as a function of radius, and (c) Ar<sup>+</sup> ion temperatures at 10 mTorr as a function of radius.

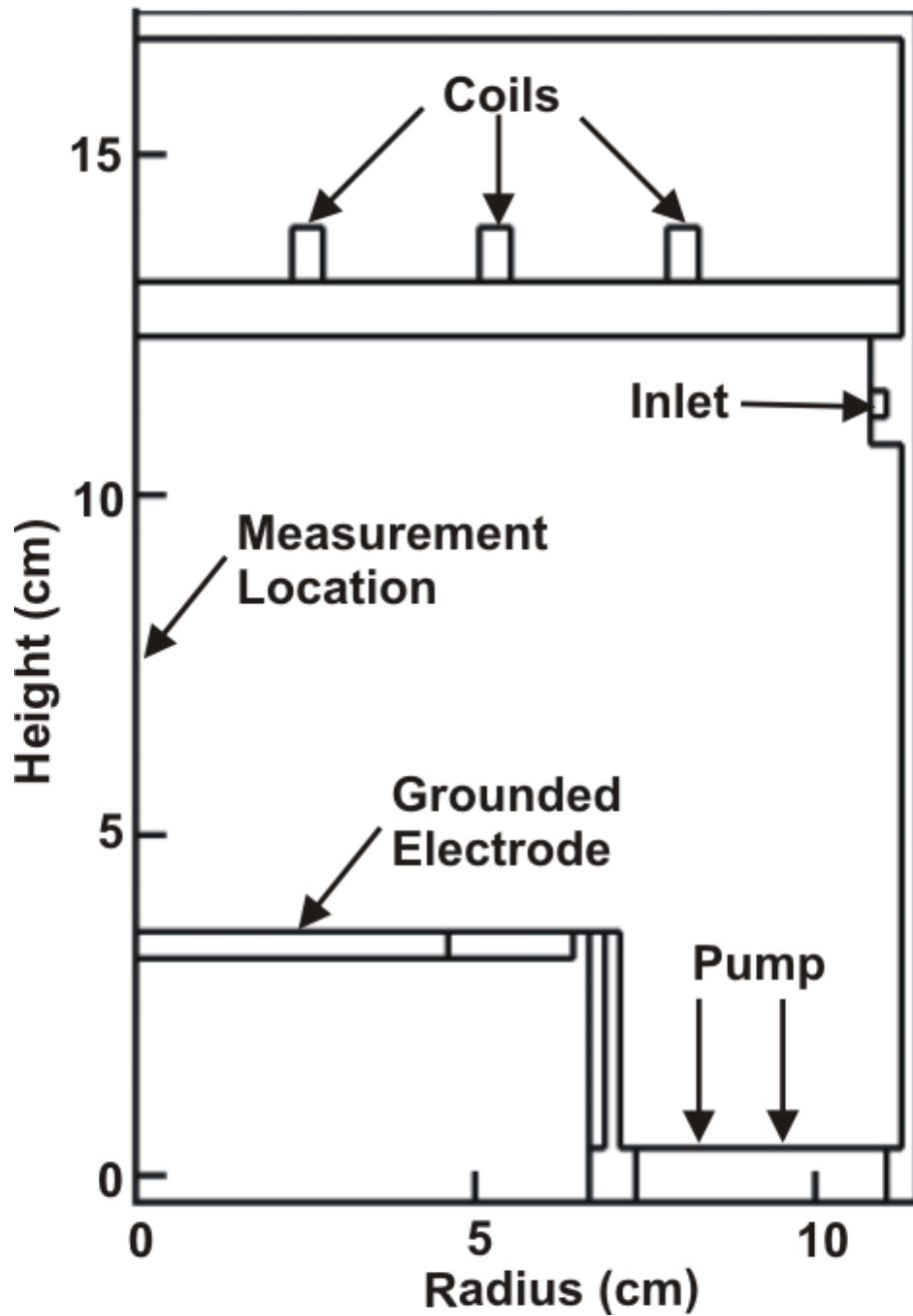


Fig. 4.5. Schematic of the ICP reactor used for parameterizations. A three-turn coil couples inductive power to the chamber. The lower electrode is grounded.

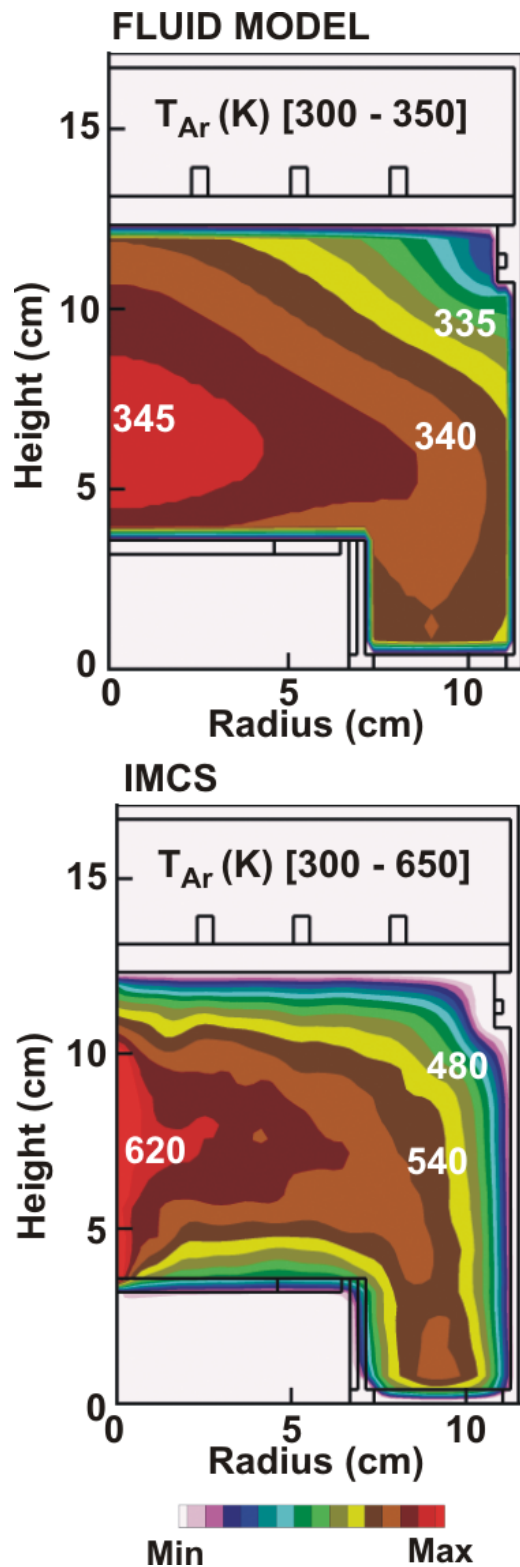


Fig. 4.6. Comparison of the neutral temperatures in an Ar discharge (300 W, 2 mTorr, 100 sccm). The temperatures predicted using the IMCS are higher than those obtained using fluid equations.

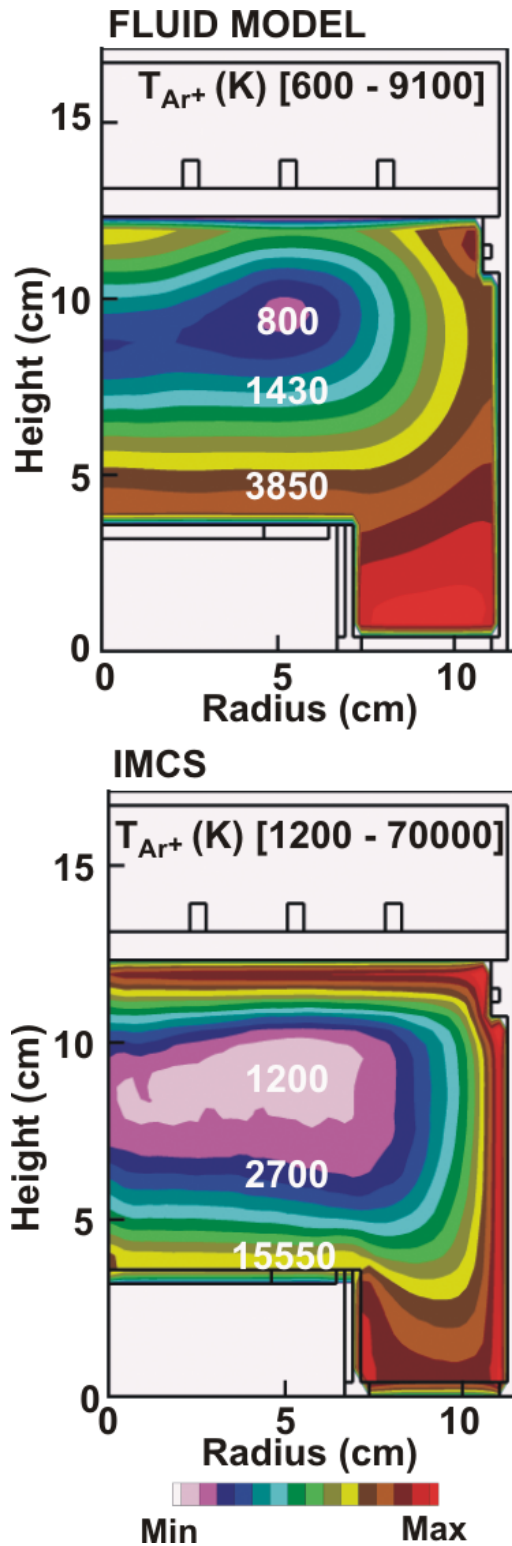


Fig. 4.7. Comparison of the ion temperatures in an Ar discharge (300 W, 2 mTorr, 100 sccm). The temperatures predicted using the IMCS are higher than those obtained using fluid equations.

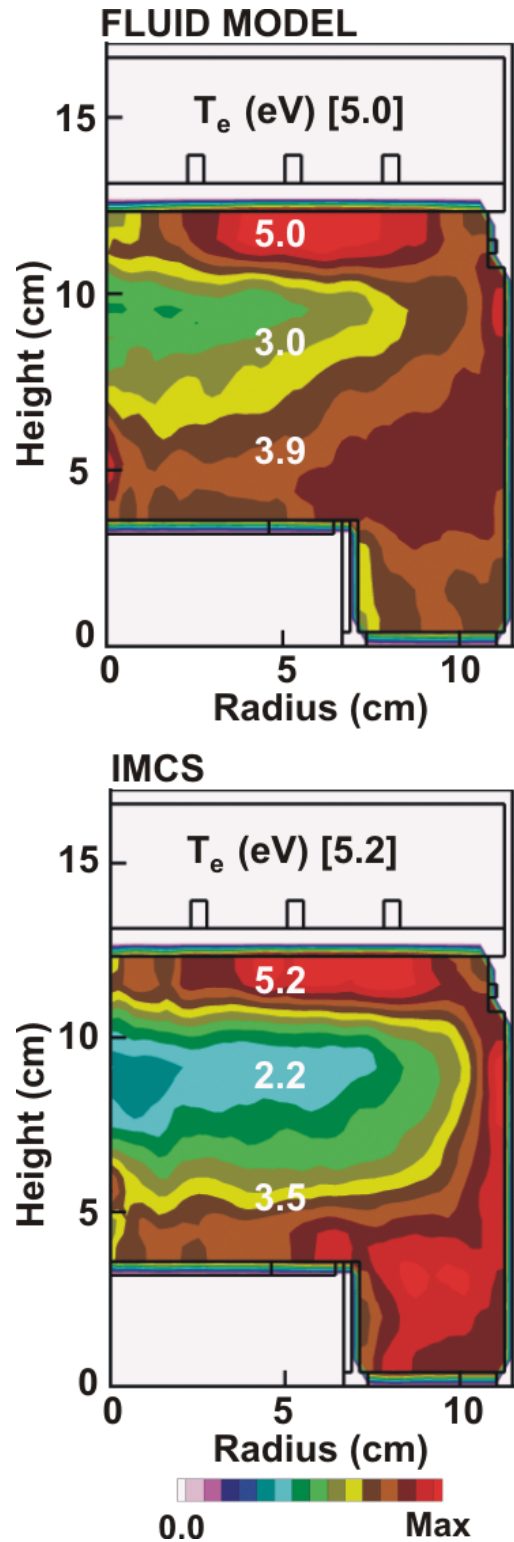


Fig. 4.8. Comparison of electron temperatures in an Ar discharge (300 W, 2 mTorr, 100 sccm). The peak temperatures predicted using the IMCS are higher than those obtained using fluid equations.

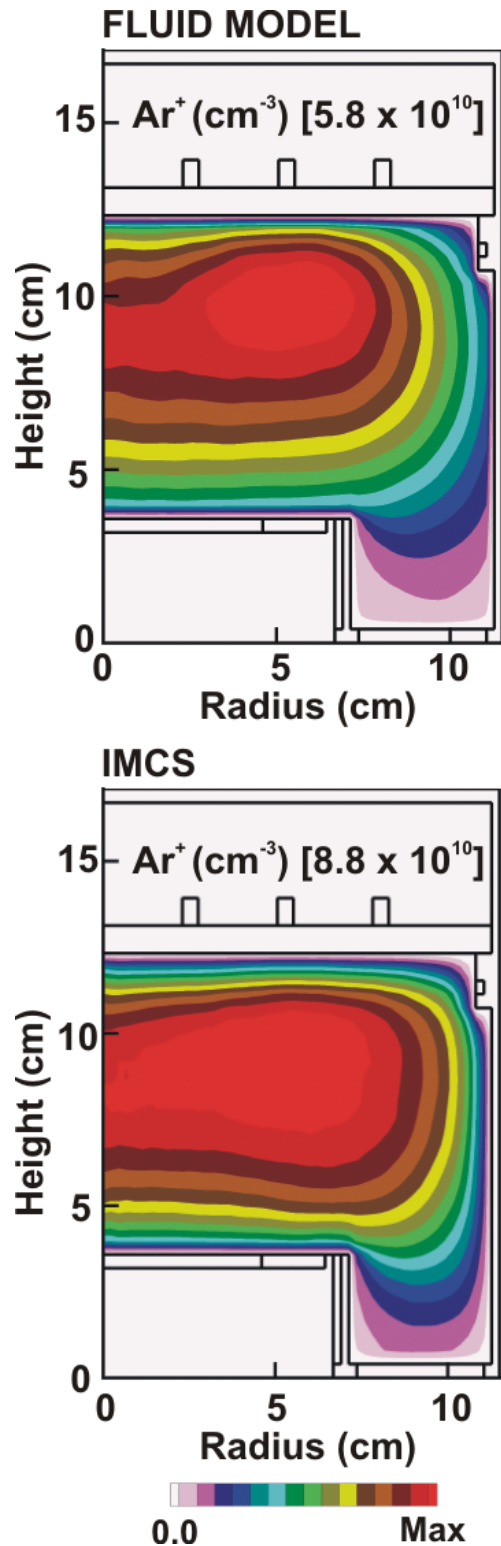


Fig. 4.9. Comparison of Ar<sup>+</sup> ion densities in an Ar discharge (300 W, 2 mTorr, 100 sccm). The densities predicted using the IMCS are higher and the profiles flatter than those obtained using fluid equations.

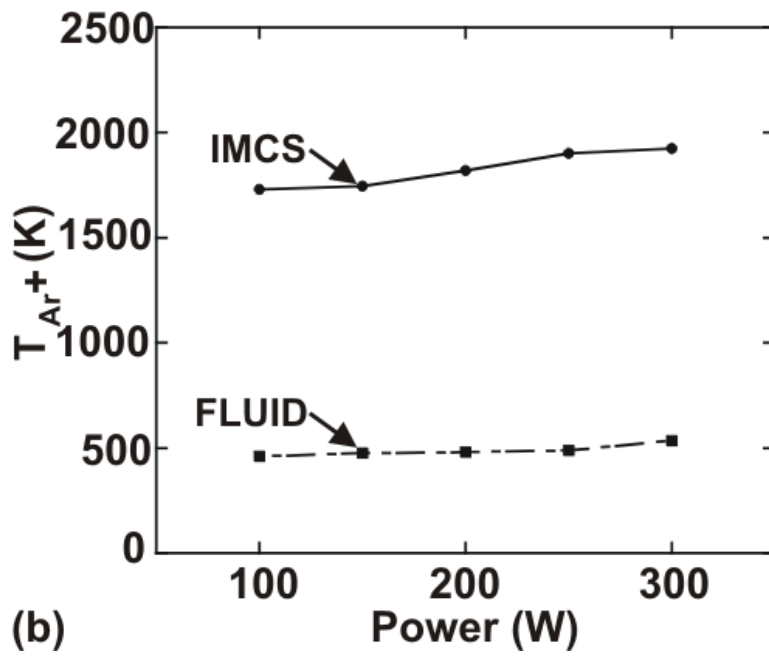
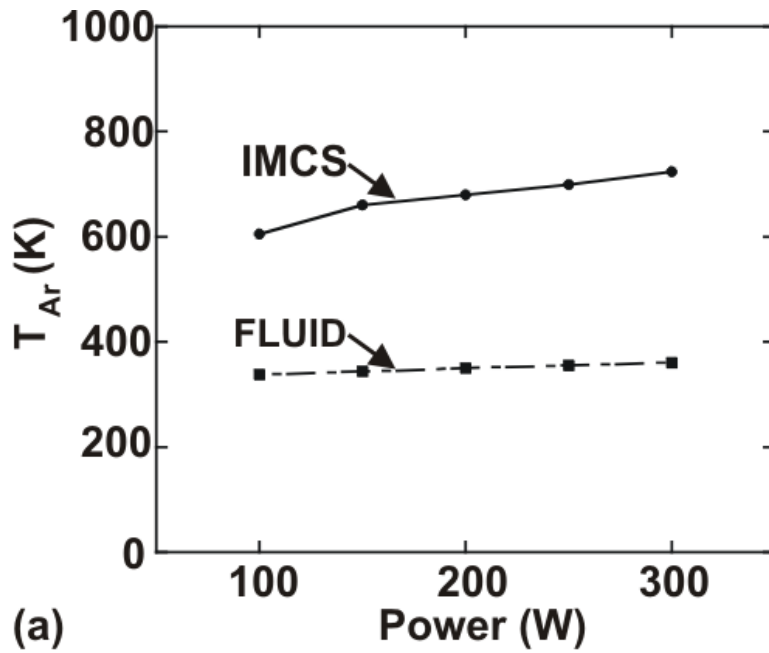


Fig. 4.10. Comparison of neutral and ion temperatures in an Ar discharge (300 W, 2 mTorr, 100 sccm) as a function of power.

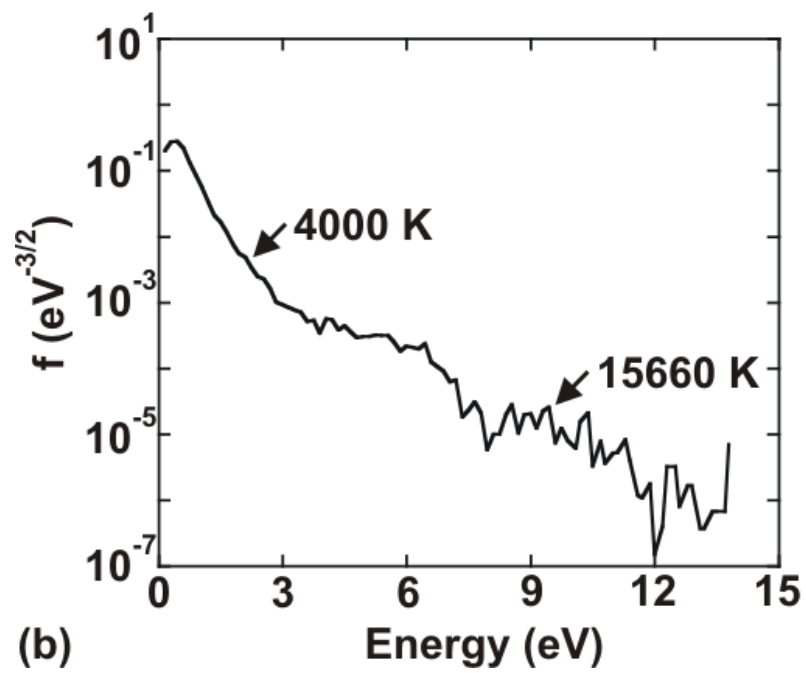
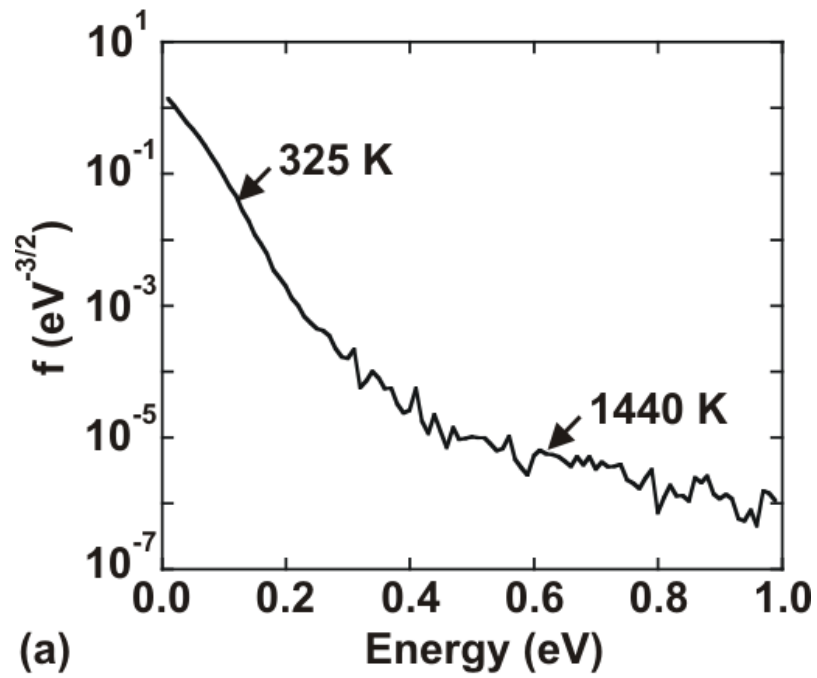


Fig. 4.11. ED in an Ar discharge (100 W, 10 mTorr, 100 sccm) for (a) Ar, and (b) Ar<sup>+</sup>.

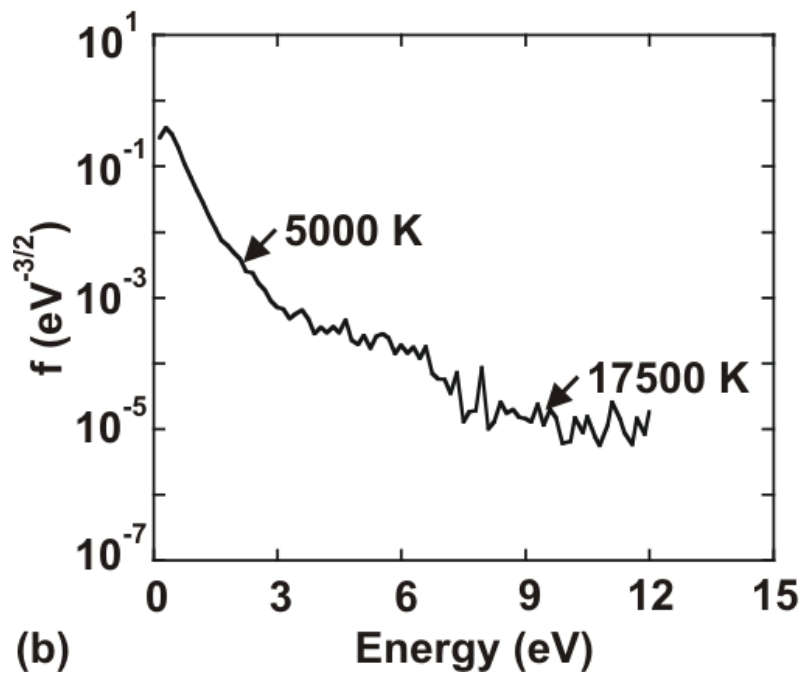
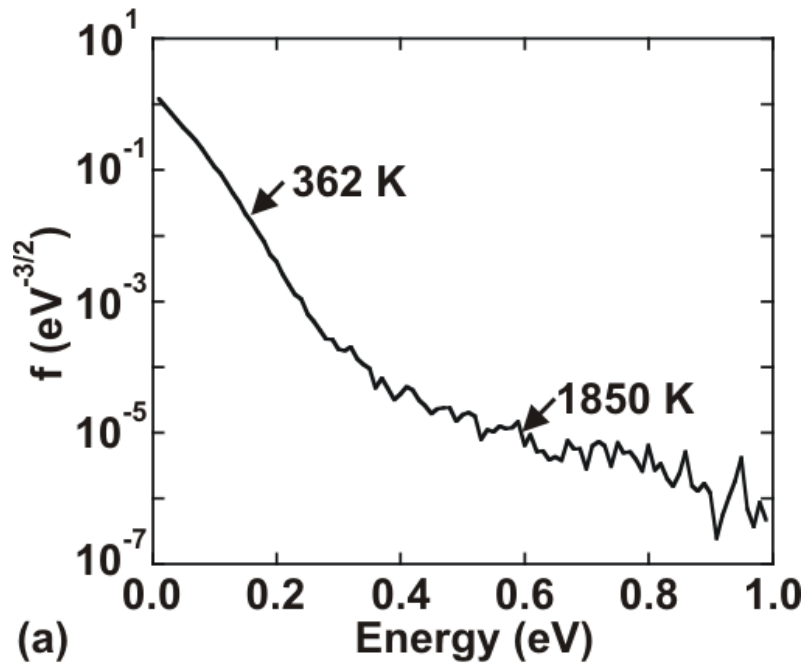


Fig. 4.12. ED in an Ar discharge (300 W, 10 mTorr, 100 sccm) for (a) Ar, and (b) Ar<sup>+</sup>.

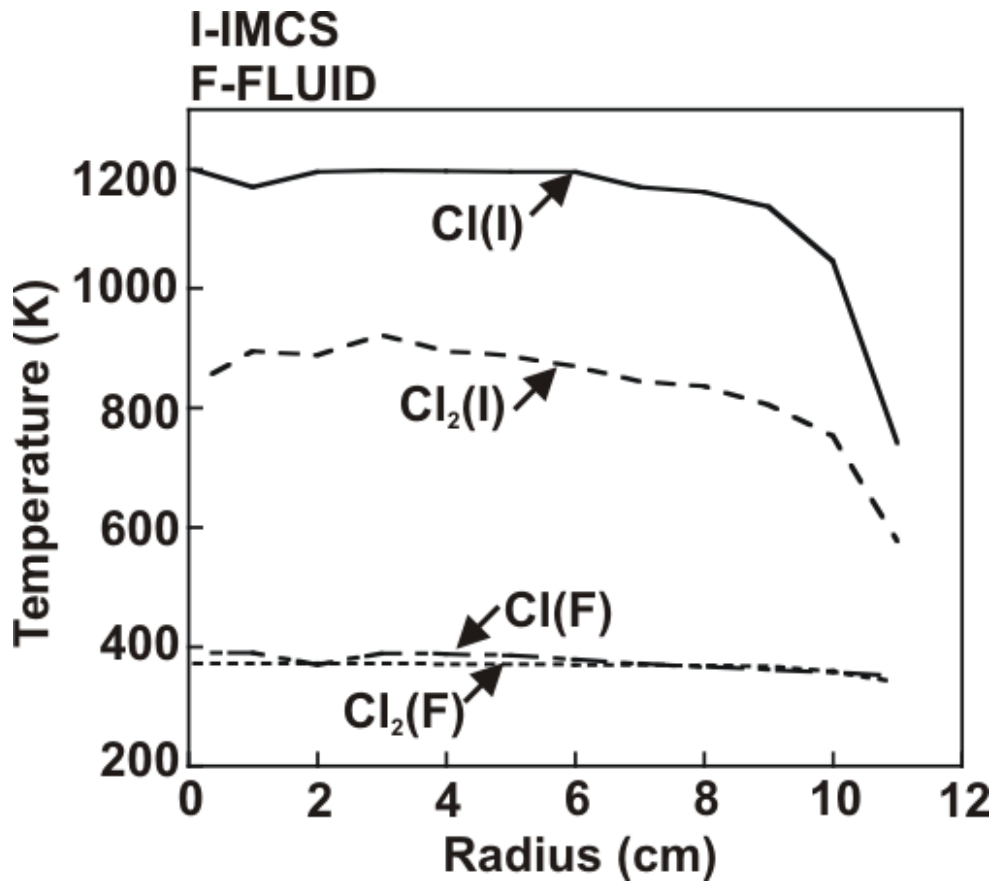
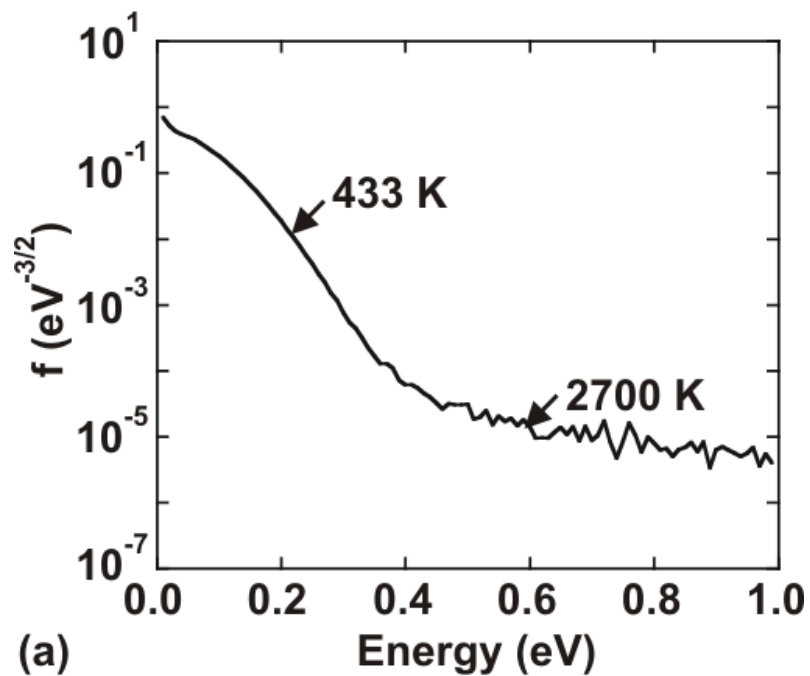
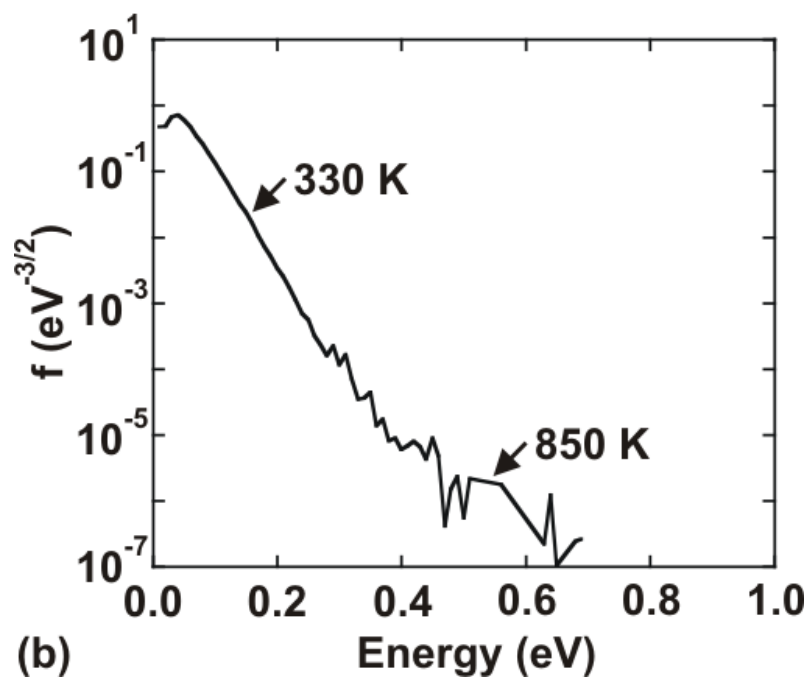


Fig. 4.13. Comparison of the neutral temperatures in an Ar/Cl<sub>2</sub> = 80/20 discharge (300 W, 10 mTorr, 100 sccm). The temperatures peak in the center of the reactor and are higher for Cl neutrals.



(a)



(b)

Fig. 4.14. ED in an  $\text{Ar}/\text{Cl}_2 = 80/20$  discharge (300 W, 10 mTorr, 100 sccm) for (a) Cl, and (b)  $\text{Cl}_2$ .

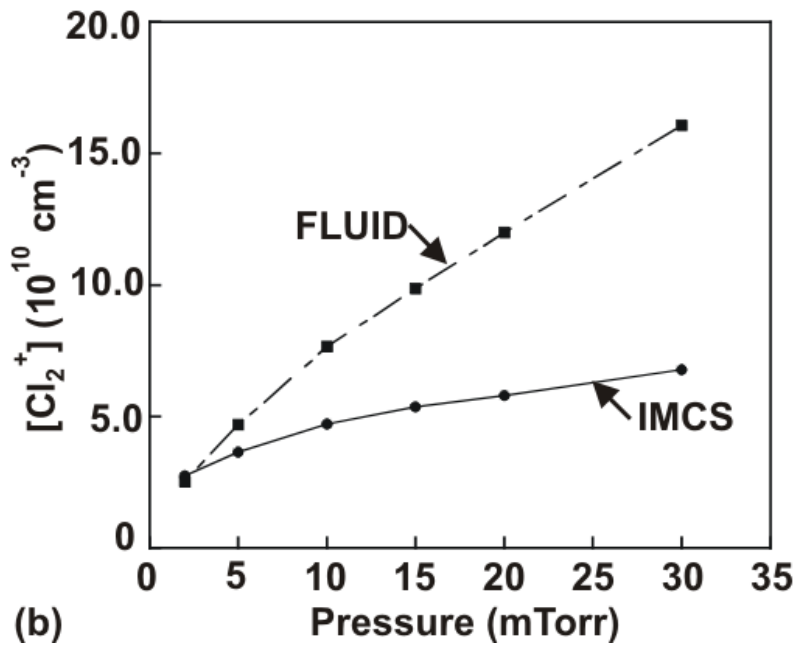
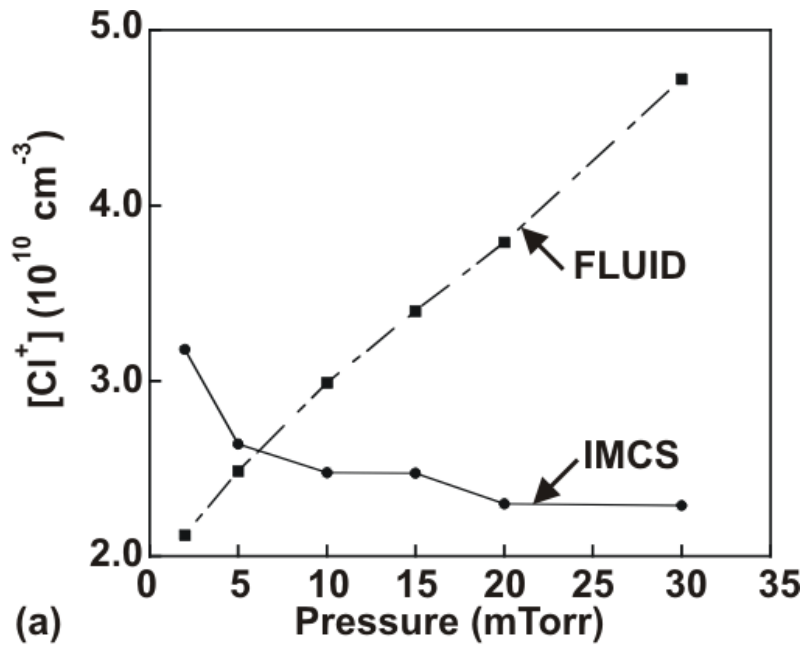
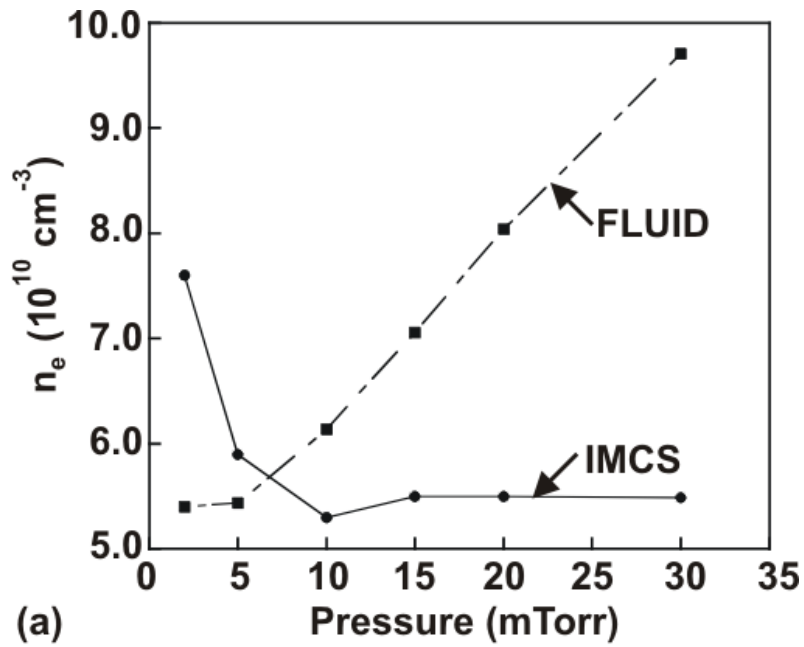
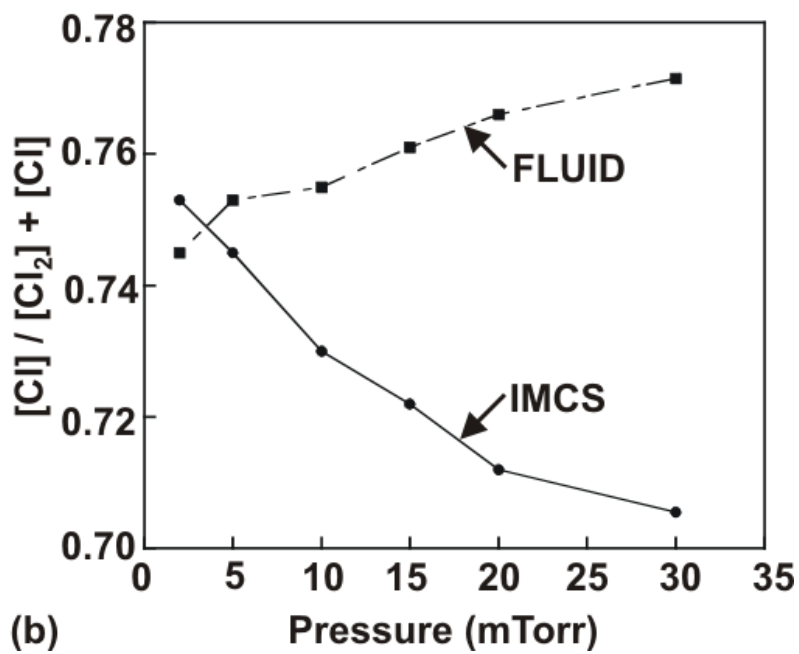


Fig. 4.15. Comparison of the chlorine ion densities in an Ar/Cl<sub>2</sub> = 80/20 discharge (300 W, 100 sccm) as a function of pressure. (a)  $[Cl^+]$  increases with pressure when using fluid equations; the opposite trend is obtained on using the IMCS. (b)  $[Cl_2^+]$  increases with pressure for both cases.



(a)



(b)

Fig. 4.16. Plasma properties in an Ar/Cl<sub>2</sub> = 80/20 discharge (300 W, 100 sccm) as a function of pressure. (a) Electron density, and (b) [Cl] / [Cl + Cl<sub>2</sub>].

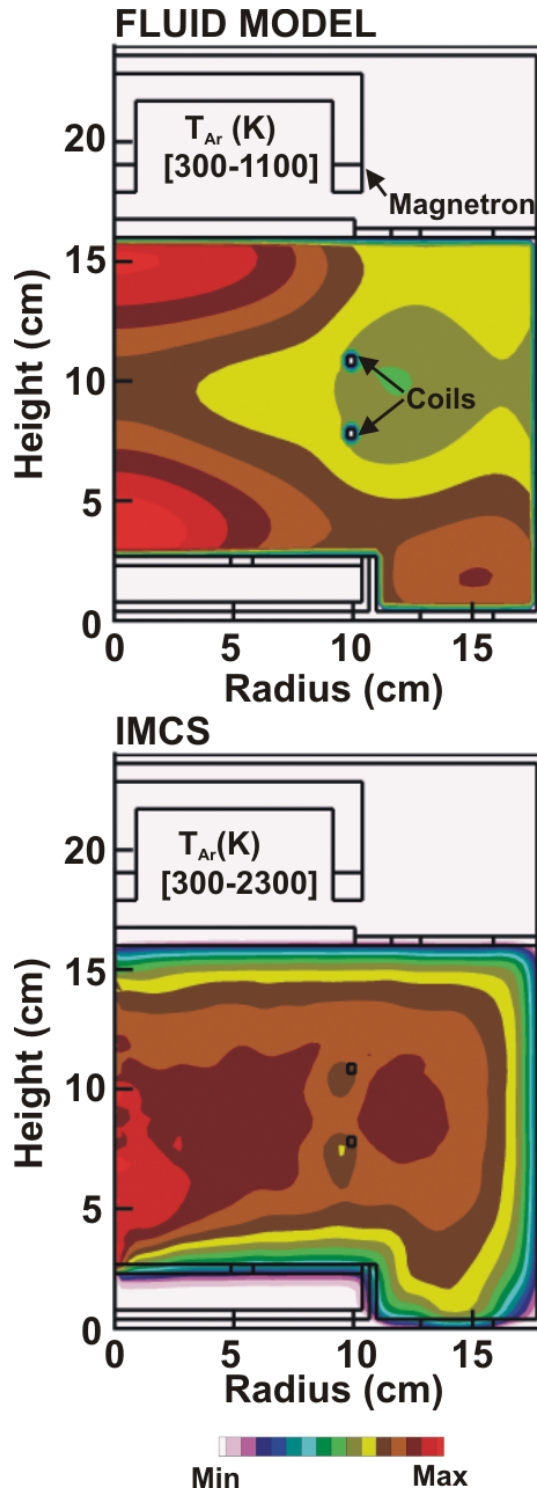


Fig. 4.17. Comparison of Ar neutral temperatures in an ionized metal physical vapor deposition reactor (Ar, 1-kW ICP power, 300-W magnetron power, 10 mTorr). The temperatures predicted using the IMCS are higher than those predicted using fluid equations

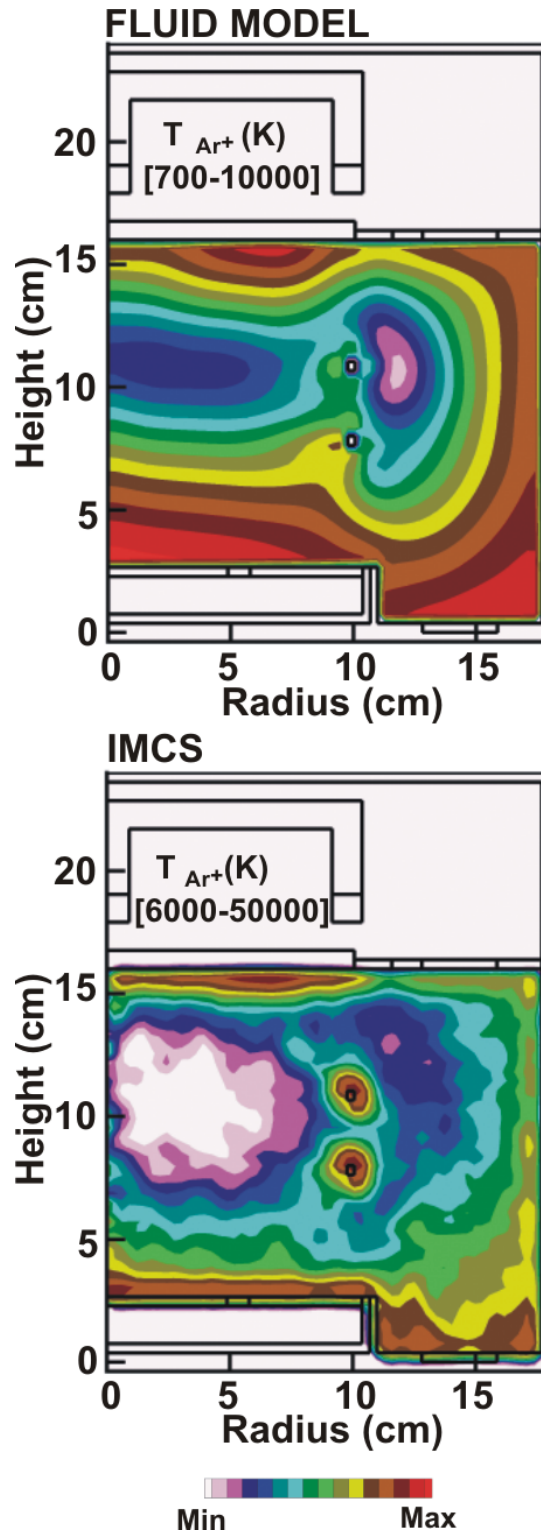


Fig. 4.18. Comparison of  $Ar^+$  ion temperatures in an ionized metal physical vapor deposition reactor (Ar, 1 kW ICP power, 300 W magnetron power, 10 mTorr). The temperatures predicted using the IMCS are higher than those predicted using fluid equations.

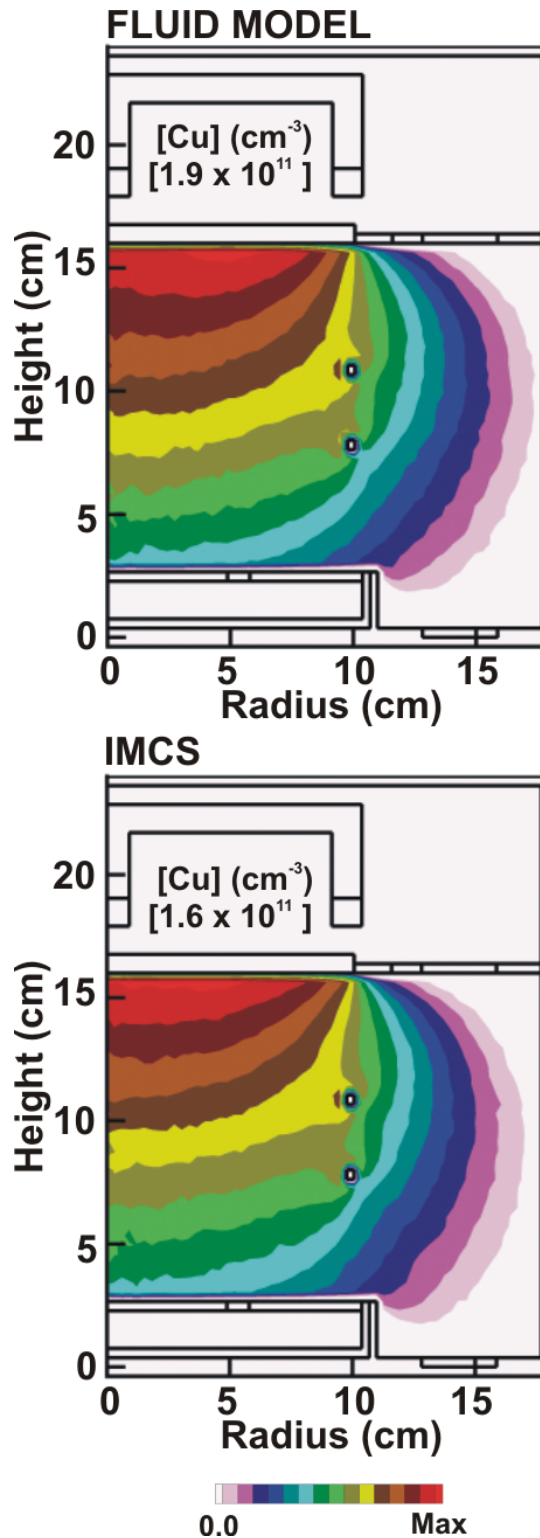


Fig. 4.19. Comparison of non-thermal Cu densities in an ionized metal physical vapor deposition reactor (Ar, 1 kW ICP power, 300 W magnetron power, 10 mTorr). The densities predicted using the IMCS are lower than those predicted using fluid equations.

# **CHAPTER 5**

## **IONIZED METAL PHYSICAL VAPOR DEPOSITION**

### **5.1 Introduction**

Ionized Metal Physical Vapor Deposition (IMPVD) at pressures of a few mTorr is being increasingly used to deposit diffusion barriers and Cu seed layers into high aspect ratio trenches. At these pressures, conventional fluid or hybrid simulations are of questionable validity as transport is highly nonequilibrium and a kinetic approach may be warranted. A Monte Carlo simulation for ion and neutral transport (IMCS) has been developed and integrated with a plasma equipment model to improve the capabilities to address lower pressures. The consequences of varying process parameters such as power, pressure, and magnetic fields have been investigated for a hollow cathode magnetron source and comparison has been made with experiments. A parametric study of the Cu seed layer deposition process has been carried out using a feature scale profile model.

### **5.2 Description of the Model**

The computational platform used for the equipment scale modeling is the 2D Hybrid Plasma Equipment Model (HPEM), which has been described in detail in Chapter 2. The Ion/Neutral Monte Carlo Simulation (IMCS), described in Chapter 4, has been used to obtain the transport coefficients for use in the HPEM. The Cu seed layer deposition processes have been modeled using the Monte Carlo Feature Profile Model (MCFPM), which has been described in Chapter 3. The transport of sputtered neutrals is modeled using Monte Carlo techniques. The ion and neutral energy and angular distributions (EADs) are obtained using the Plasma

Chemistry Monte Carlo Module. The details of the sputter module and the Plasma Chemistry Monte Carlo Module have been listed in Chapter 2.

The Ar/Cu plasma chemistry employs the reaction mechanism assembled by Grapperhaus et al. [1], as shown in Appendix D. The majority of the reactions belong to either electron-impact reactions or charge-exchange reactions. The electron-argon chemistry includes electron impact excitation of Ar from ground state to excited states 4s and 4p (which are lumped into Ar<sup>\*</sup>) and electron impact ionization (from Ar ground state to Ar<sup>\*</sup>). The electron-copper chemistry includes electron impact excitation of Cu from ground state [<sup>2</sup>S<sub>1/2</sub>] to higher excited states [<sup>2</sup>D<sub>5/2</sub>], [<sup>2</sup>D<sub>3/2</sub>], [<sup>2</sup>P<sub>1/2</sub>], [<sup>2</sup>P<sub>3/2</sub>] (which are lumped into Cu<sup>\*</sup>) and electron impact ionization (from Cu ground state and Cu<sup>\*</sup>). The Cu<sup>\*</sup> is quenched by collisions with Cu, Cu<sup>\*</sup>, and Ar. The Ar<sup>\*</sup> reacts with Ar<sup>\*</sup> to produce Ar<sup>+</sup> and with Cu or Cu<sup>\*</sup> to produce Cu<sup>+</sup> through Penning processes. Charge exchange reactions play an important role in generating fast neutral fluxes to the target and ionizing Cu atoms before they reach the substrate. The charge exchange reactions also include resonant exchange among the Ar species or the Cu species, which contributes to gas heating, as well as the resonant exchange between Ar<sup>+</sup> and Cu species.

### 5.3 Cu IMPVD in a Hollow Cathode Magnetron Source

Parameterizations were carried out in the reactor shown in Fig. 5.1, which is our interpretation of the Novellus 200-mm reactor [2]. The source consists of a cup-shaped Cu target, fixed magnets at the side and at the top, a floating anode ring and substrate, and a pump port surrounding the substrate. The pressure in the reactor was varied from 1 to 30 mTorr and the power was varied from 10 to 80 kW. The DC bias applied to the target was correspondingly varied from -150 to -500 V to achieve the desired target power. The Ar flows in the reactor were

25 to 750 sccm. The species for which the temperatures and transport coefficients were computed using the IMCS were Ar, Ar<sup>+</sup>, Cu, and Cu<sup>+</sup>.

The radially averaged Cu neutral energy distributions (NED) in the center of the reactor (12 cm above the substrate) for a Cu HCM (10 kW) as a function of pressure are shown in Fig. 5.2(a). At 30 mTorr, the high-energy neutrals are fairly Maxwellian with a temperature of 2050 K. At 5 mTorr, we see two slopes, indicating a bi-Maxwellian distribution. The high-energy tail of the distribution corresponds to a temperature of 1550 K. The more collisional plasma at high pressures results in a higher charge exchange reaction rate with more energetic ions, resulting in higher temperatures and a more Maxwellian distribution of energies. The Cu NED 2.5 cm above the substrate are shown in Fig. 5.2(b). At 30 mTorr, the temperatures are higher than in the reactor center as the propensity for a neutral to exchange energy with the high-energy ions is greater due to the greater distance traversed. The higher temperature of neutrals at higher pressures is again a consequence of the higher charge exchange collision rate. The twin-sloped IED at 5 mTorr indicates the nonequilibrium at low pressures.

The radially averaged Cu ion energy distributions (IED) in the center of the reactor are shown in Fig. 5.3(a). The distributions are non-Maxwellian at lower pressures indicating nonequilibrium. The IED appear more Maxwellian near the substrate. As the ions traverse through the reactor, the chance of undergoing collisions increases resulting in a Maxwellian distribution. The decrease in the ion temperatures at 30 mTorr near the substrate is indicative of the ions having undergone thermalizing collisions.

The electron densities in the reactor for different pressures are shown in Fig 5.4. The peak electron densities in the reactor increase with pressure and are  $2.1 \times 10^{12} \text{ cm}^{-3}$  and  $2.4 \times 10^{12} \text{ cm}^{-3}$  for 1 and 30 mTorr, respectively. The peak in electron density shifts from the center of

the reactor to the target surface as pressure is increased from 1 to 30 mTorr. The mean free path and conductivity of electrons decrease with pressure, and as a consequence, the electrons are more confined to the target surface, coinciding with the peak in the source function for secondary electrons. The radially averaged total Cu flux incident on the substrate decreases from  $3.6 \times 10^{16} \text{ cm}^{-2}\text{s}^{-1}$  at 1 mTorr to  $1.8 \times 10^{16} \text{ cm}^{-2}\text{s}^{-1}$  as shown in Fig 5.5(a). At 1 mTorr, the non-thermal and thermal Cu fluxes are  $2.6 \times 10^{16} \text{ cm}^{-2}\text{s}^{-1}$  and  $1.8 \times 10^{15} \text{ cm}^{-2}\text{s}^{-1}$ , respectively. At 30 mTorr, the nonthermal and thermal Cu fluxes are  $5.9 \times 10^{15} \text{ cm}^{-2}\text{s}^{-1}$  and  $5.3 \times 10^{13} \text{ cm}^{-2}\text{s}^{-1}$ , respectively. The decrease in the total Cu flux is due to the reduction in the incident nonthermal and the loss of Cu neutrals to other surfaces as a consequence of increased diffusion and backscattering into the target. The scattering also results in a longer dwell time for Cu in the plasma, and therefore higher Cu ionization. The total ion flux increases from  $3.9 \times 10^{16} \text{ cm}^{-2}\text{s}^{-1}$  at 1 mTorr to  $7.4 \times 10^{16} \text{ cm}^{-2}\text{s}^{-1}$  at 30 mTorr, respectively.  $\text{Ar}^+$  ions are the dominant species in the flux and the ratio of  $\text{Ar}^+$  ions to  $\text{Cu}^+$  ion flux is 3.3 and 5 at 1 mTorr and 30 mTorr respectively. The fraction of Cu incident on the wafer as ions is shown in Fig. 5.5(b) increases from 0.25 at 1 mTorr to 0.67 at 30 mTorr. As the pressure increases, the mean free path for Cu neutrals (2 cm at 20 mTorr, 1000 K) decreases. A larger fraction of Cu neutrals are thermalized and have a higher probability of undergoing ionizing collisions. Hence, the ionization fraction of the incident metal increases with pressure. The spatial variation of fluxes incident on the substrate is shown in Fig. 5.6.  $\text{Ar}^+$  is the dominant species in the ion flux and is a maximum in the reactor center for low pressures and off-axis for higher pressures. This is a consequence of the ionization peak shifting from the reactor center to the target surface at high pressures. The nonuniform  $\text{Cu}^+$  flux at high pressures is due to a sharp centrally peaked  $\text{Cu}^+$  density profile.

A key metric in successful trench filling using electroplating is the requirement of low overhang, the ratio of lateral overburden of Cu deposit at the mouth of the trench to Cu thickness in the field. A large value for overhang can result in incomplete filling and void formation in the subsequent electroplating step. A diffuse angular distribution of the incident neutral flux results in the neutrals preferentially depositing at the top of the trench due to the larger solid angle of the plasma viewed from those locations. The ion and neutral EADs on the substrate are shown in Fig. 5.7. The Cu neutrals have a larger angular spread at higher pressures due to there being more collisions. The substrate floating potential increases from  $-0.2$  V to  $-11$  V as the pressure increases from 1 mTorr to 30 mTorr. Consequently the ion energies increase and the EADs narrow with pressure. The Cu seed layer deposition profiles for a feature with critical dimension of 65 nm and an aspect ratio ( $\beta$ ) of 2.5 predicted using MCFPM are shown in Fig. 5.8. The overhang decreases from 0.92 at 1 mTorr to 0.60 at 30 mTorr. Cheng et al. observed smaller overhangs with increasing pressure in a conventional magnetron cathode system [3]. The ionized fraction of Cu incident on the substrate increases with pressure and is more anisotropic resulting in less overhang formation at the mouth of the trench.

The hollow cathode magnetron sources rely on magnetic fields to generate a high-density plasma within the volume of the cathode. The magnetic field contours and the magnetic flux vectors in the reactor are shown in Fig. 5.9. A strong  $E \times B$  force along the target surface captures secondary electrons emitted from the target surface resulting in efficient sputtering of target material. As compared to planar cathodes where there is a large loss of primary electrons to the anode and walls of the chamber around the target, the unique target geometry of HCM allows for strong electrostatic (target negative bias) and magnetic confinement within the source volume. The HCM magnetic field is set up such that a magnetic cusp is generated near the target

opening. The cusp acts as an aperture to extract plasma from within the target volume. Klawuhn et al. made Langmuir probe measurements, which indicated a high on-axis plasma density and a sharp drop-off in the radial direction taking an almost Gaussian shape [4]. The extracted plasma beam is responsible for additional ionization of sputtered metal in the downstream of the chamber.

The location of the magnetic field cusp C was varied in order to optimize the Cu seed layer deposition process. The peak of the source function for electrons is more diffuse when the magnetic cusp is located near the target opening, as shown in Fig. 5.10. The electric and magnetic fields being parallel at the target opening allows electrons to escape the hollow cathode region. The electron flux vectors indicate that the cusp acts as an aperture to extract the plasma from within the target area, and the closer the cusp to the target area, the more electrons escape to the center of the reactor. The peak electron density in the reactor increases from  $1.7 \times 10^{12} \text{ cm}^{-3}$  for  $C = 12 \text{ cm}$  to  $2.3 \times 10^{12} \text{ cm}^{-3}$  for  $C = 20 \text{ cm}$ . The ion densities in the reactor are shown for different cusp locations in Fig. 5.10. The  $\text{Cu}^+$  and  $\text{Ar}^+$  densities in the reactor are shown in Fig 5.11, and they mirror the electron densities. The higher threshold Ar ionization process (15.7 eV) primarily takes place adjacent to the target surface, corresponding to the peak in the electron temperature at those locations. As the location of the cusp (C) is moved closer to the target opening, the ionization peak increases and shifts from the target surface to the center of the reactor. Cu has a lower ionization potential of 7.49 eV and the existence of a low ionization potential  $\text{Cu}^*$  metastable state allows electrons with lower energy to ionize Cu. Consequently, we observe  $\text{Cu}^+$  peaking closer to the reactor center than  $\text{Ar}^+$ .

The Cu NED do not show appreciable variation with cusp location as shown in Fig 5.12. The temperatures are 2090 K and 2270 K in the center of the reactor and substrate, respectively.

The higher temperatures near the substrate are a consequence of a greater probability for charge exchange collisions as the neutrals traverse from the target to the substrate. The Cu IED exhibits deviation from Maxwellian behavior for low cusp locations as shown in Fig. 5.13. The peak in the source function for  $\text{Cu}^+$  shifts from the center of the reactor to the target surface as the cusp is moved to lower locations. The larger fraction of ions originating in the high-energy target region is responsible for the high-energy tail obtained for lower cusp locations. The ion temperatures in the center of the reactor are 3.3 eV, 2.4 eV, and 2.3 eV when the cusp is located at 11 cm, 16 cm, and 20 cm, respectively. The magnetron voltage and, consequently the electric fields, decrease with cusp location, resulting in higher ion temperatures. The magnetron voltages are -280 V, -210 V, and -190 V when the cusp is located at 11 cm, 16 cm, and 20 cm respectively. The ion temperatures near the substrate were 4.3 eV, 2.5 eV, and 3.0 eV when the cusp is located at 11 cm, 16 cm, and 20 cm, respectively.

The total Cu flux incident on the substrate peaks for intermediate cusp locations, as shown in Fig. 5.14(a). This behavior is ultimately linked to the  $\text{Cu}^+$  flux incident on the substrate, which is  $6.8 \times 10^{15} \text{ cm}^{-2}\text{s}^{-1}$ ,  $1.2 \times 10^{16} \text{ cm}^{-2}\text{s}^{-1}$ , and  $6.5 \times 10^{15} \text{ cm}^{-2}\text{s}^{-1}$  for  $C = 12 \text{ cm}$ ,  $C = 16 \text{ cm}$ , and  $C = 20 \text{ cm}$ , respectively. The total ion flux is a minimum for  $C = 16 \text{ cm}$ , coinciding with a minimum in the  $\text{Ar}^+$  ion flux, the dominant species, at that location. For intermediate cusp locations, the total Cu flux is at its maximum. A larger fraction of electrons are lost in the ionization of Cu. As a result  $\text{Cu}^+$  flux peaks at the location, though the total ion flux is at its minimum. The ionized fraction of Cu incident on the substrate peaks for intermediate cusp locations as shown in Fig. 5.14(b). The spatial variation of fluxes incident on the substrate mirror the ion density profiles, as shown in Fig. 5.15. The increased nonuniformity in the  $\text{Cu}^+$

flux for  $C = 20$  cm is a consequence of the sharply peaked  $\text{Cu}^+$  density in the center of the reactor.

The ion and neutral EADs on the substrate are shown in Fig. 5.16. The collisionality of the plasma strongly influences the EADs. The neutral density in the reactor scales inversely with temperature at a given pressure. The neutral temperatures and densities do not vary significantly with cusp location, and the peak value in the reactor center was  $\sim 1000$  K. Consequently, the ion and neutral EADs do not change significantly with cusp location. Cu seed layer deposition profiles for various cusp locations are shown in Fig. 5.17. The overhangs are 0.18, 0.5, and 0.26 for  $C = 11$  cm,  $C = 16$  cm, and  $C = 20$  cm. The smaller total ion flux for the intermediate cusp locations results in less resputtering and consequently a larger overhang.

The model was validated with comparisons to Langmuir probe measurements of electron density and temperature in a commercial 200-mm HCM source [2]. The pressure in the reactor varied from 1 to 12 mTorr and the power varied from 20 to 36 kW. The DC bias applied to the target was correspondingly varied from -300 to -500 V to achieve the desired target power. The relative strengths of the side magnets were varied to alter the location of the magnetic field cusp. The electron density as a function of height above the substrate when the magnetic field cusp is located away from the target is shown in Fig. 5.18(a). The electron density peaks 12.5 cm above the substrate and has a peak value of  $9.0 \times 10^{11} \text{ cm}^{-3}$ . The model predicts the electron density peaking at a height of 22 cm above the substrate and having a peak value of  $1.2 \times 10^{12} \text{ cm}^{-3}$ . The electron densities as a function of height above the substrate when the magnetic field cusp is located at the target opening are shown in Fig. 5.18(b). The electron density peaks in the center of reactor and has a maximum value of  $1.6 \times 10^{12} \text{ cm}^{-3}$ , higher than that obtained when the cusp is away from the target. The peak electron density predicted by the model is  $2.2 \times 10^{12} \text{ cm}^{-3}$  15

cm above the substrate. At locations closer to the substrate, the electron density decreases steadily in the center of the reactor, but increases at off-axis locations.

When the cusp is located away from the target, the electron temperatures increase as a function of height and peak in the hollow cathode region, as shown in Fig. 5.19(a). The model also predicts a similar trend. The electron temperatures do not change appreciably as a function of radius. When the cusp is located at the target opening, the electron temperature increases with height in the center of the reactor, as shown in Fig. 5.19(b). The model results agree well with the experimental observations. However, at off-axis locations, electron temperature decreases with height indicative of a diverging plasma beam. Hot electrons in the center cool as the beam diverges, heating up the electrons near it off-axis. The model predicts qualitatively similar trends.

The effect of magnetic field strength at the target surface,  $B$ , was investigated for a constant target bias of  $-200$  V and an Ar pressure of 10 mTorr. The nonthermal Cu densities are shown in Fig. 5.20. The nonthermal Cu density peaks at the Cu target sidewall and moves progressively to higher locations as  $B$  is increased from 25 to 2000 G. The peak value for the nonthermal Cu density is  $2.9 \times 10^{12} \text{ cm}^{-3}$ ,  $1.6 \times 10^{13} \text{ cm}^{-3}$ , and  $1.2 \times 10^{13} \text{ cm}^{-3}$  for  $B = 25$  G,  $B = 500$  G, and  $B = 2000$  G respectively. The electron densities and the ion momentum flux vectors in the target region are shown in Fig. 5.21. The peak in the ion-momentum flux corresponds to the peak in the nonthermal Cu densities at locations of maximum sputtering. The peak electron density increases from  $8.9 \times 10^{11} \text{ cm}^{-3}$  for  $B = 25$  G to  $5.4 \times 10^{12} \text{ cm}^{-3}$  for  $B = 500$  G as a result of increased magnetic confinement. The Larmor radius decreases from 0.25 cm for 25 G to 0.03 mm for 2000 G. A stronger  $E \times B$  force along the target surface for higher magnetic fields captures secondary electrons emitted from the target surface, resulting in efficient sputtering of

target material. However, increased confinement at very high magnetic fields results in ionization peaking in a very narrow region adjacent to the target surface. As a result, the electron density and the sputtering rates decrease for higher magnetic field strengths. The electron density peak is more diffuse at lower magnetic field strengths. For  $B = 25$  G,  $[\text{Cu}^+]$  peaks in the center of the reactor; for higher magnetic field strengths we obtained peaks near the target surface representative of the peaks in the electron density.

The Cu NED as a function of magnetic field at the target surface is shown in Fig. 5.22. The Cu neutral temperatures in the center of the reactor are 1773 K, 2030 K, and 1940 K, respectively, for magnetic field strengths of 25G, 500 G, and 2000 G, a consequence of the  $\text{Cu}^+$  densities and the sputter rates being the largest for intermediate magnetic field strengths. The same trend occurs for the NED near the substrate and the temperatures are 1700 K, 1990 K, and 1860 K respectively for magnetic field strengths of 25G, 500 G, and 2000 G. The Cu IED show departure from Maxwellian distribution for a magnetic field strength of 25 G, as shown in Fig 5.23. The much lower nonthermal Cu density and the consequent nonequilibrium in the plasma for low magnetic fields is responsible for the non-Maxwellian characteristics. In the center of the reactor, the temperatures obtained from the high-energy tail of the IED are 1.42 eV, 3.09 eV, and 2.79 eV for magnetic field strengths of 25 G, 500 G, and 2000 G respectively. The ion temperatures near the substrate are 1.75 eV, 3.88 eV, and 3.71 eV for magnetic field strengths of 25 G, 500 G, and 2000 G, respectively. The increase in temperatures is a consequence of acceleration of the ions in the presheath region.

The total Cu flux incident on the wafer shows the same trend as the non-thermal Cu densities and is a maximum for  $B = 500$  G. The  $\text{Cu}^+$  flux incident on the substrate is  $6.9 \times 10^{15}$   $\text{cm}^{-2}\text{s}^{-1}$ ,  $1.5 \times 10^{16}$   $\text{cm}^{-2}\text{s}^{-1}$ , and  $1.4 \times 10^{16}$   $\text{cm}^{-2}\text{s}^{-1}$  for  $B = 25$  G,  $B = 500$  G, and  $B = 2000$  G,

respectively. Though the  $\text{Cu}^+$  ion flux peaks at  $B = 500$  G, the nonthermal Cu flux peaks at the same location and consequently, the ionized fraction of Cu incident on the wafer is the smallest, as shown in Fig 5.24. The reduced magnetic confinement at  $B = 25$  G results in electron density peaking in the center of the reactor resulting in increased ionization of Cu neutrals as they traverse from the target to the substrate, and consequently, a higher ionized Cu fraction on the substrate. The total ion flux peaks at  $B = 500$  G.

The ion and neutral EADs on the substrate are shown in Fig. 5.25. The neutral temperatures peak in the center of the reactor and are 800 K, 2000 K, and 1500 K for magnetic field strengths of 25 G, 500 G, and 2000 G, respectively. The consequent gas rarefaction at higher magnetic fields results in a less collisional plasma and narrower spread in the Cu EADs. The substrate floating potential increases from  $-3$  V at 25 G to  $-15$  V at 2000 G, resulting in narrower ion EADs. The Cu seed layer deposition profiles are shown in Fig. 5.26. The overhang is a maximum for  $B = 25$  G, a consequence of the broad EADs and also the minimum in the ion flux incident on the substrate.

The spatial variation of flux incident on the substrate is shown in Fig. 5.27.  $\text{Ar}^+$  is the dominant species in the ion flux and has a minimum at the edge of the substrate. The Cu flux consists of the thermal and nonthermal fluxes. The increase in the Cu flux with magnetic field is due to the increased contribution of nonthermal Cu flux due to enhanced sputtering. The greater spatial nonuniformity in the nonthermal Cu densities is reflected in the Cu flux profiles, which peak in the reactor center. The neutral temperatures peak in the center of the reactor. The associated gas rarefaction results in a reduced angular spread for Cu neutral EADs in the center of the reactor, as shown in Fig. 5.28. The substrate floating potential and, consequently, the ion EADs do not change appreciably with spatial location, as shown in Fig. 5.29. The Cu seed layer

deposition profiles are shown in Fig. 5.30. The overhang is smaller for higher magnetic fields due to the narrower ion and neutral EADs. There are slight spatial variations in the overhang, and the minimum occurs 4.5 cm from the center of the reactor. We speculate that a maximum in the total ion flux relative to the Cu neutral flux along with the gradual broadening of the neutral EADs with radius is responsible for this trend.

The effect of power on Cu seed layer deposition was investigated. The target bias was dynamically adjusted to get the desired power deposition. The target biases applied to get a target power deposition of 10, 40, and 70 kW were  $-210$  V,  $-470$  V, and  $-550$  V, respectively. The electron densities in the reactor increase with power and the peak moves towards the top of the target. The  $\text{Cu}^+$  and  $\text{Ar}^+$  densities in the reactor are shown in Fig 5.31, and they mirror the electron densities. The higher threshold Ar ionization process (15.7 eV) primarily takes place adjacent to the target surface, corresponding to the peak in the electron temperature at those locations. The peak nonthermal Cu density increases from  $6.9 \times 10^{12} \text{ cm}^{-3}$  to  $4.1 \times 10^{13} \text{ cm}^{-3}$  as the power is increased from 10 to 70 kW, a consequence of the much larger ion flux on the target at higher powers. The total Cu flux incident on the wafer increases from  $2.0 \times 10^{16} \text{ cm}^{-2}\text{s}^{-1}$  to  $1.2 \times 10^{17} \text{ cm}^{-2}\text{s}^{-1}$  as the power is increased from 10 to 70 kW as shown in Fig. 5.32. However, the  $\text{Cu}^+$  flux increase is less; from  $1.1 \times 10^{16} \text{ cm}^{-2}\text{s}^{-1}$  to  $1.5 \times 10^{16} \text{ cm}^{-2}\text{s}^{-1}$ ; consequently, the ionized Cu fraction incident on the wafer decreases from 0.56 to 0.12 as the power increases from 10 to 70 kW. The total ion flux increases from  $4.5 \times 10^{16} \text{ cm}^{-2}\text{s}^{-1}$  to  $1.3 \times 10^{17} \text{ cm}^{-2}\text{s}^{-1}$ . The spatial variation of fluxes on the substrate as a function of power mirrors is shown in Fig. 5.33.  $\text{Ar}^+$  density peaks near the target surface and the nonuniformities are evened out at the substrate level.  $\text{Cu}^+$  density has a more diffuse peak, which translates into spatial nonuniformities at the substrate.

The Cu NED for Cu HCM (10 mTorr) in the center of the reactor as a function of power exhibit Maxwellian behavior, as shown in Fig. 5.34. The temperatures are 1600 K and 3600 K for 10kW and 70 kW, respectively. The higher charge exchange rate at higher powers results in higher temperatures. The same trend is obtained for the NED near the substrate. The IED show a departure from a Maxwellian distribution and the distribution is twin-sloped for both 10 kW and 70 kW, as shown in Fig. 5.35. The magnetron voltage and, consequently, the electric fields increase with power, resulting in larger ion temperatures. For example, the magnetron voltages are  $-210$  V and  $-500$  V respectively for 10 kW and 70 kW, respectively. Near the substrate, the distribution is closer to a Maxwellian indicative of the thermalization, which occurs as the ions traverse from the target to the substrate.

The ion and neutral EADs on the substrate are shown in Fig. 5.36. The neutral temperatures peak in the center of the reactor and are 1000 K and 4000 K for 10 and 70 kW, respectively. The subsequent gas rarefaction results in narrower neutral EADs. The substrate floating potential increases from  $-0.2$  V at 10 mTorr to  $-8$  V at 30 mTorr, resulting in narrower ion EADs. The Cu seed layer deposition profiles are shown in Fig. 5.37. The overhang decreases from 0.95 to 0.83 as the power increases from 10 kW to 70 kW, a consequence of the narrower EADs and an increase in the ion flux.

## 5.4 Summary

A hybrid modeling approach has been developed in which the ion and neutral temperatures are kinetically derived and implemented in fluid equations, thereby extending their applicability to low-pressure systems. The consequences of varying power, pressure, and magnetic fields have been investigated for a hollow cathode magnetron source and comparison

has been made with experiments. The fluxes incident on the wafer are strongly influenced by the magnetic field configuration and strength. The ion flux incident on the wafer increases with pressure due to larger number of ionizing collisions. A Monte Carlo Feature Profile Model has been used to investigate the Cu seed layer deposition process. The effect of process conditions on the energy and angular distributions has been investigated. The lateral overburden at the mouth of features or “overhang” is strongly correlated to the ion and neutral energy and angular distributions and the ion flux incident on the substrate.

## 5.5 References

- [1] M. J. Grapperhaus, Z. Krivokapic, and M. J. Kushner, *J. Appl. Phys.* **83**, 35 (1998).
- [2] D. B. Hayden, M. Ow, K. A. Ashtiani, K. F. Lai, K. Levy, E. Klawuhn, and M. Danek, *AVS 47'th International Symposium*, October 2004.
- [3] P. F. Cheng, S. M. Rossnagel, and D. N. Ruzic, *J. Vac. Sci. Technol. B* **13**, 203 (1995).
- [4] E. Klawuhn, G. C. D'Cuoto, K. A. Ashtiani, P. Rymer, M. A. Biberger, and K. B. Levy, *J. Vac. Sci. Technol. A* **18**, 1546 (2000).

## 5.6 Figures

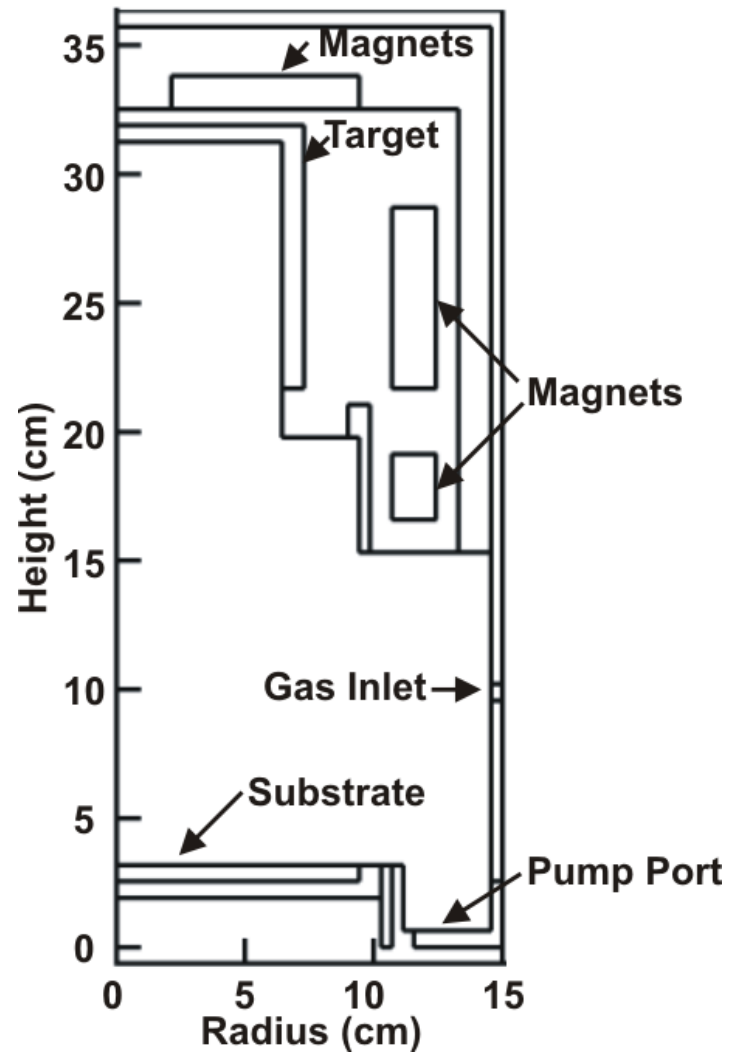


Fig. 5.1. Schematic of the hollow cathode magnetron source. The source consists of a cup-shaped Cu target with fixed magnets at the side and the top.

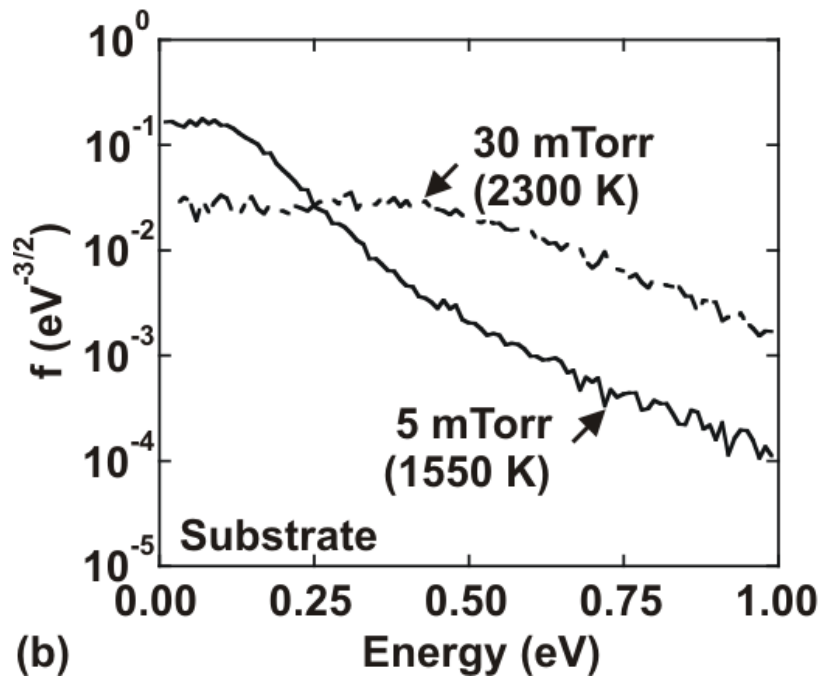
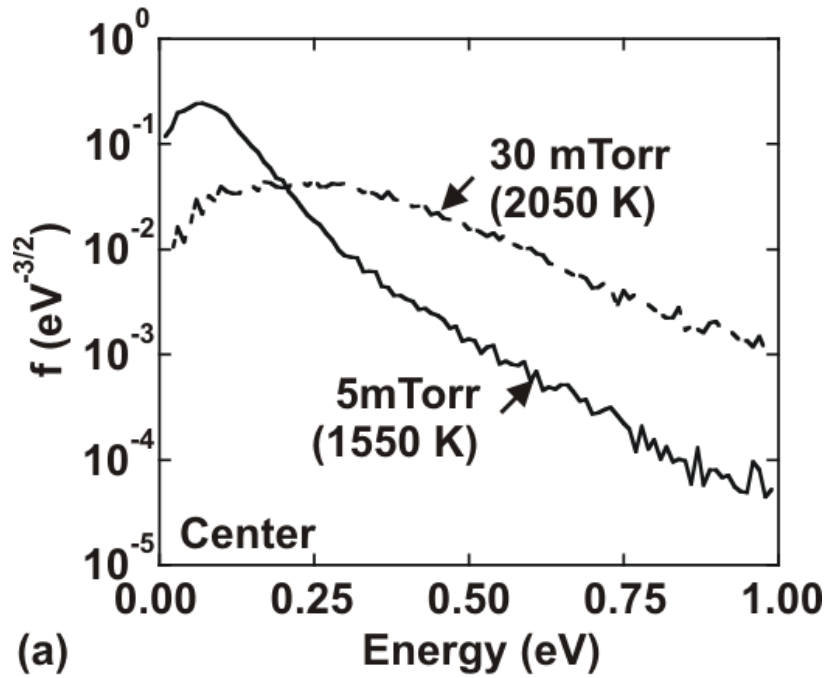


Fig. 5.2. Cu NED as a function of pressure in a Cu HCM (Ar, 10 kW) at the (a) center of the reactor, and (b) near the substrate.

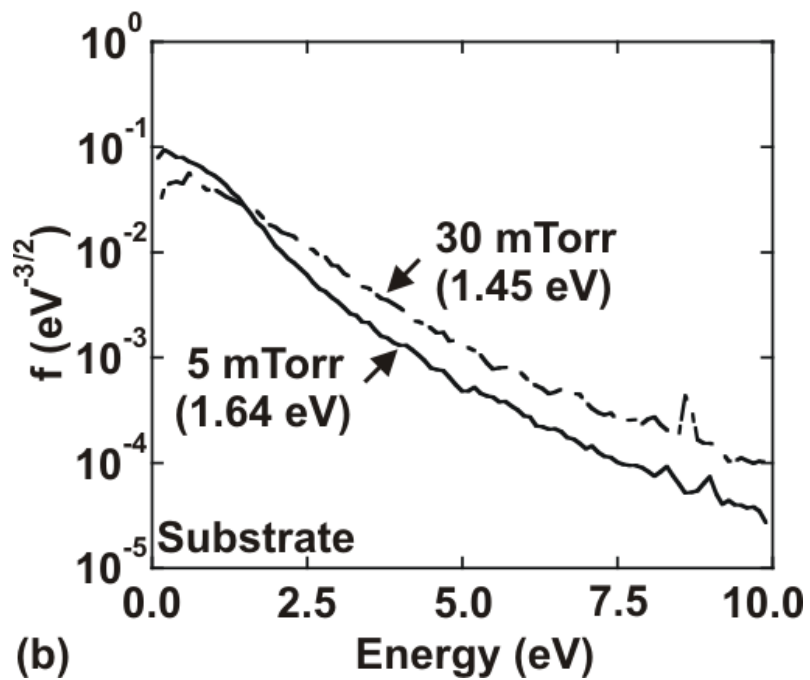
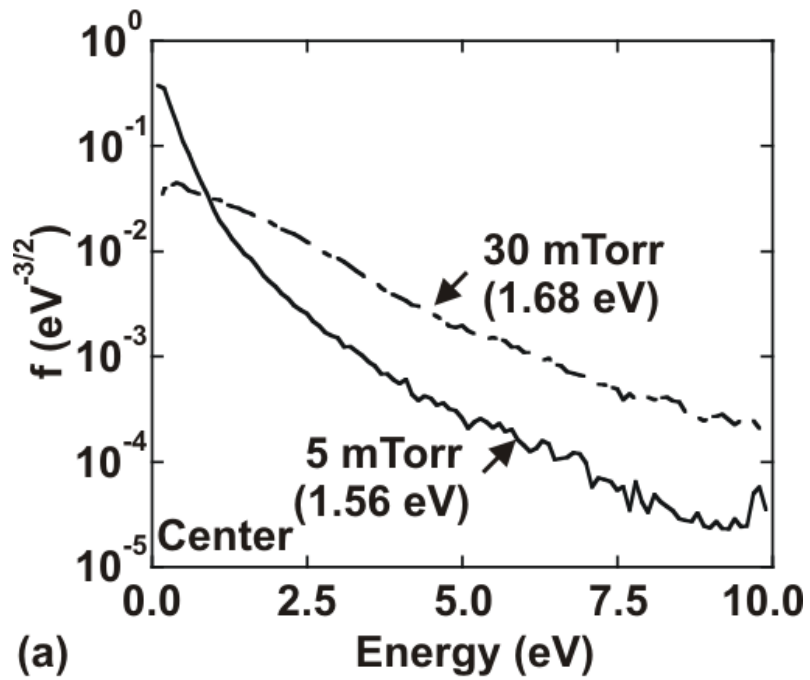


Fig. 5.3. Cu IED as a function of pressure in a Cu HCM (Ar, 10 kW) at the (a) center of the reactor, and (b) near the substrate.

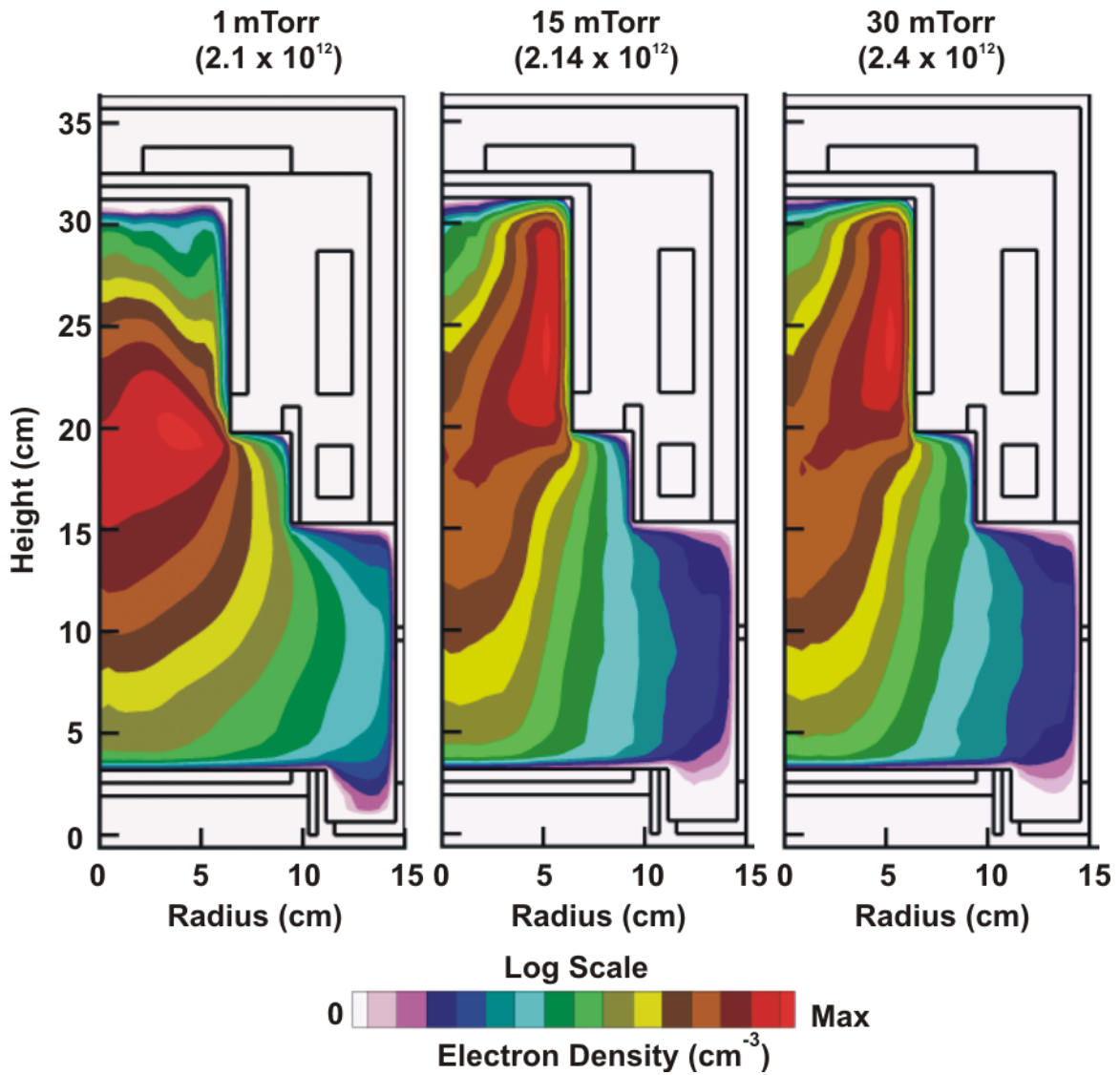


Fig. 5.4. Electron density in a Cu HCM (Ar, 10 kW) at different pressures. The peak in electron density increases and shifts from the reactor center to the target surface with increase in pressure.

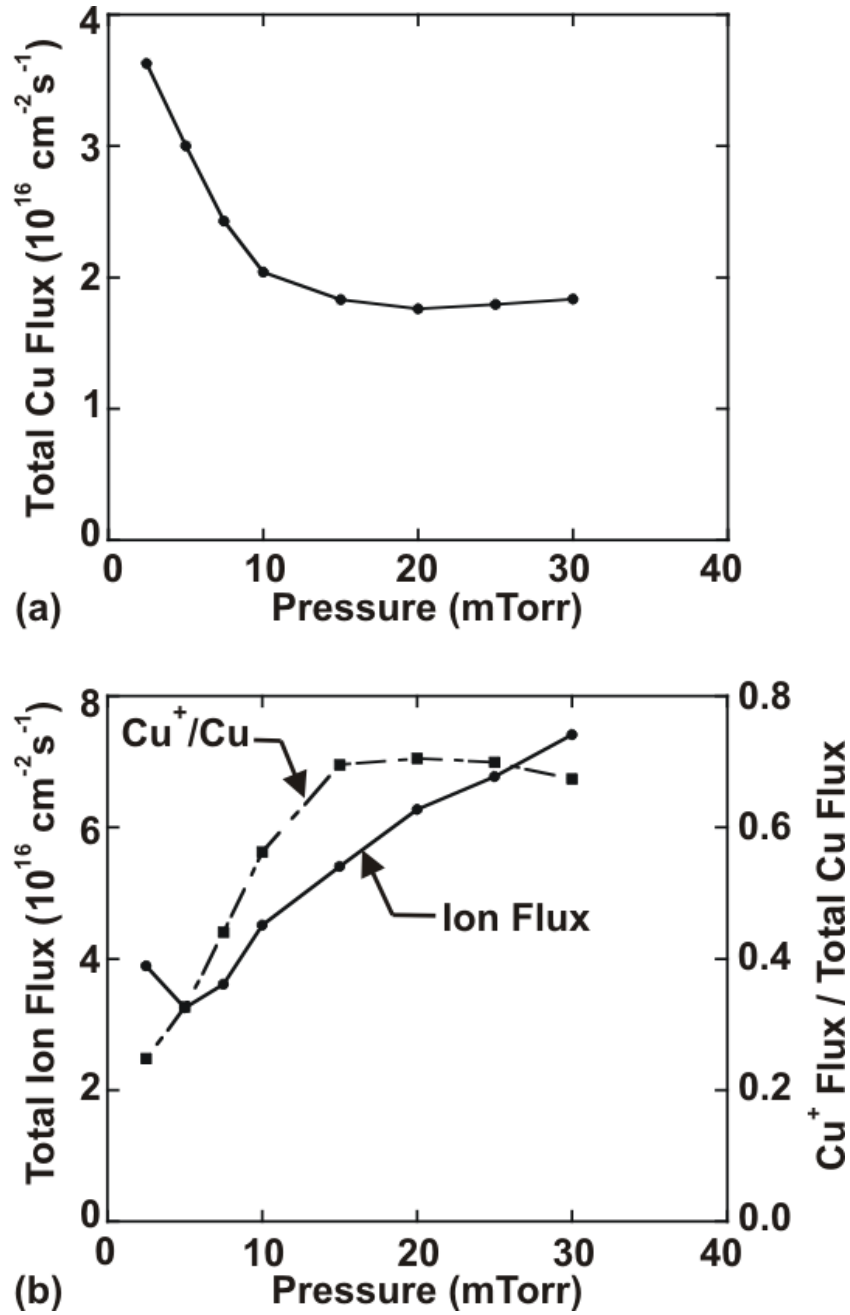


Fig. 5.5. Fluxes incident on the substrate as a function of pressure in a Cu HCM (10 kW).  
 (a) Total Cu flux, and (b) total ion flux and the ionized fraction of Cu.

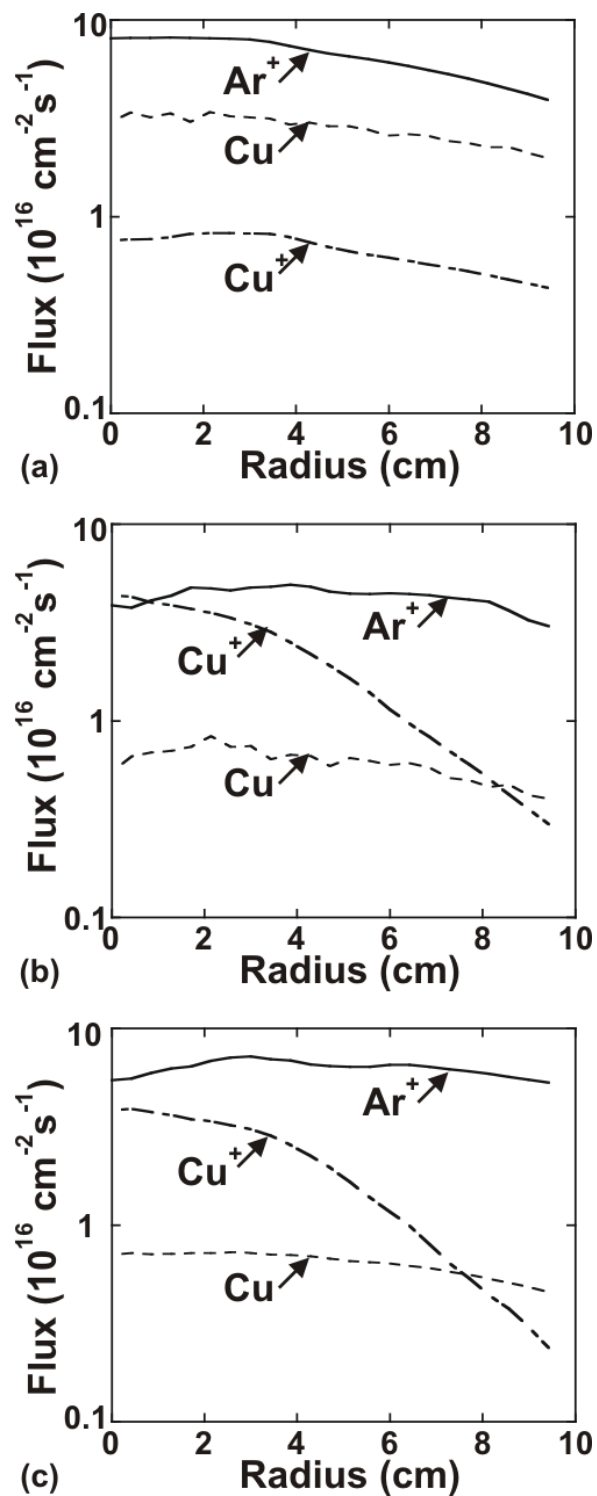


Fig. 5.6. Fluxes incident on the substrate as a function of radius in a Cu HCM (10 kW) for a pressure of (a) 1 mTorr, (b) 15 mTorr, and (c) 30 mTorr.

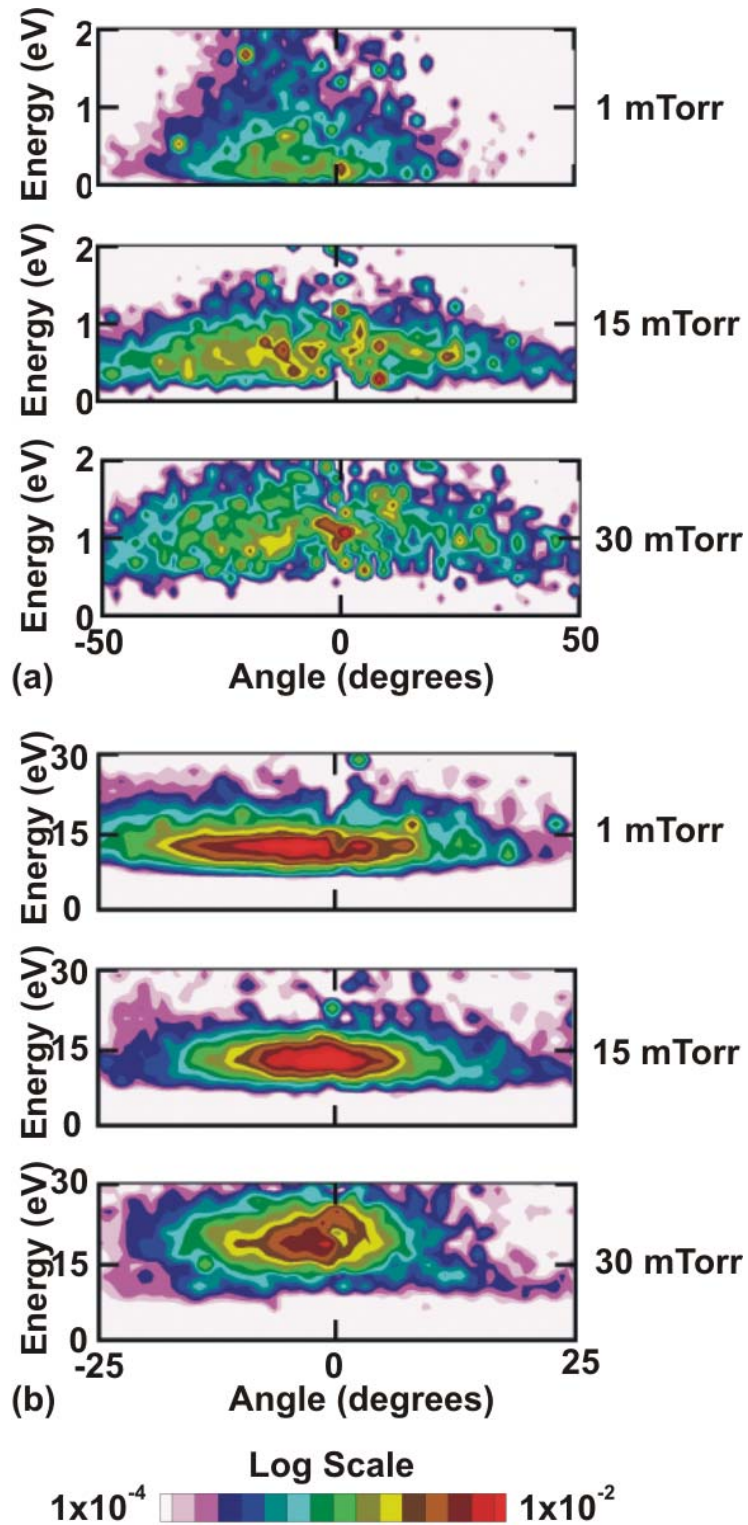


Fig. 5.7. ED incident on and averaged over the wafer as a function of pressure in a Cu HCM (10 kW) for (a) Cu neutral flux, and (b) Total ion flux.

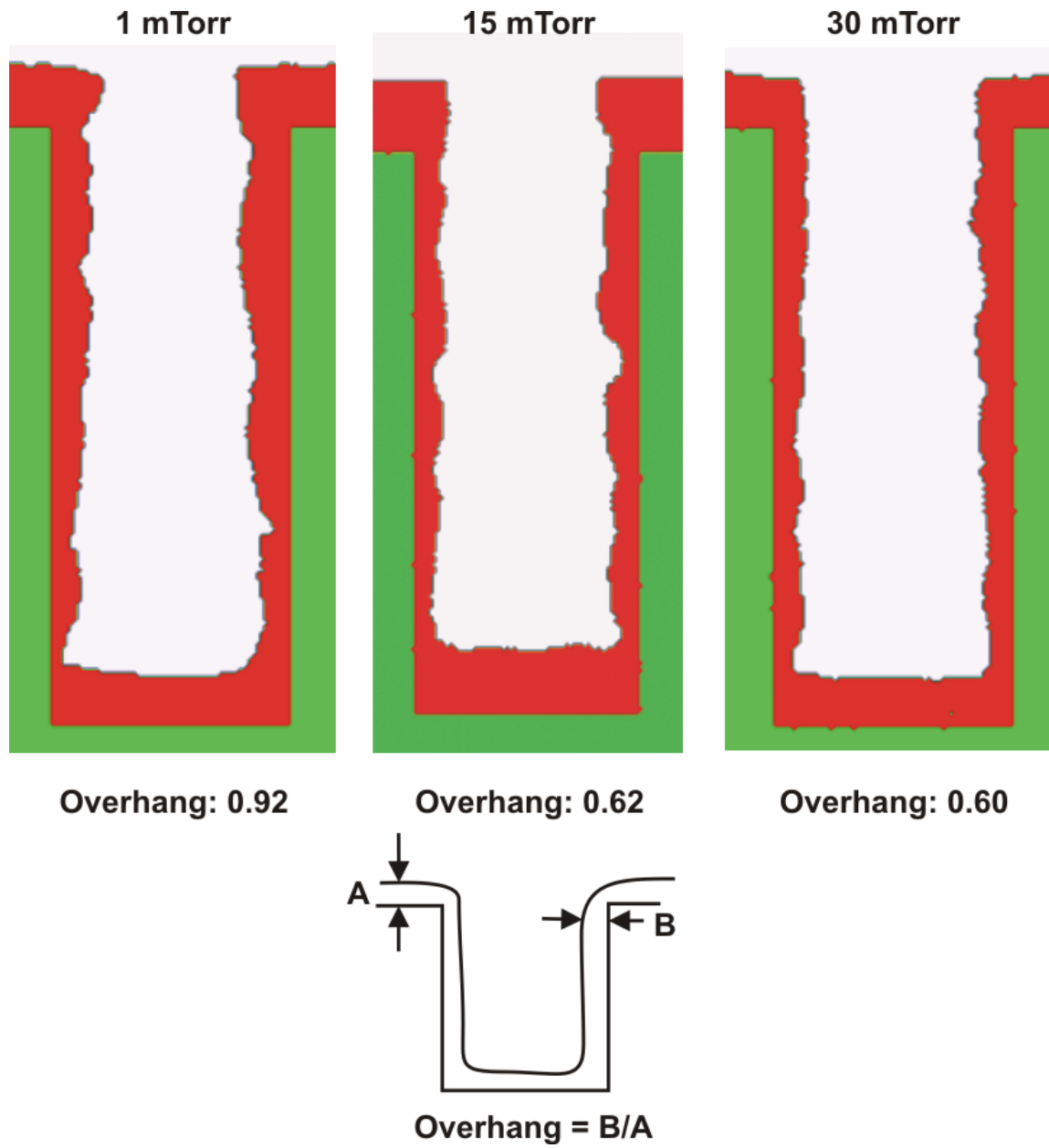


Fig. 5.8. Deposition profiles for a 65-nm feature ( $\beta = 2.5: 1$ ) in a Cu HCM (10 kW) as a function of pressure. The overhang decreases from 0.92 to 0.6 as the pressure increases from 1 to 30 mTorr.

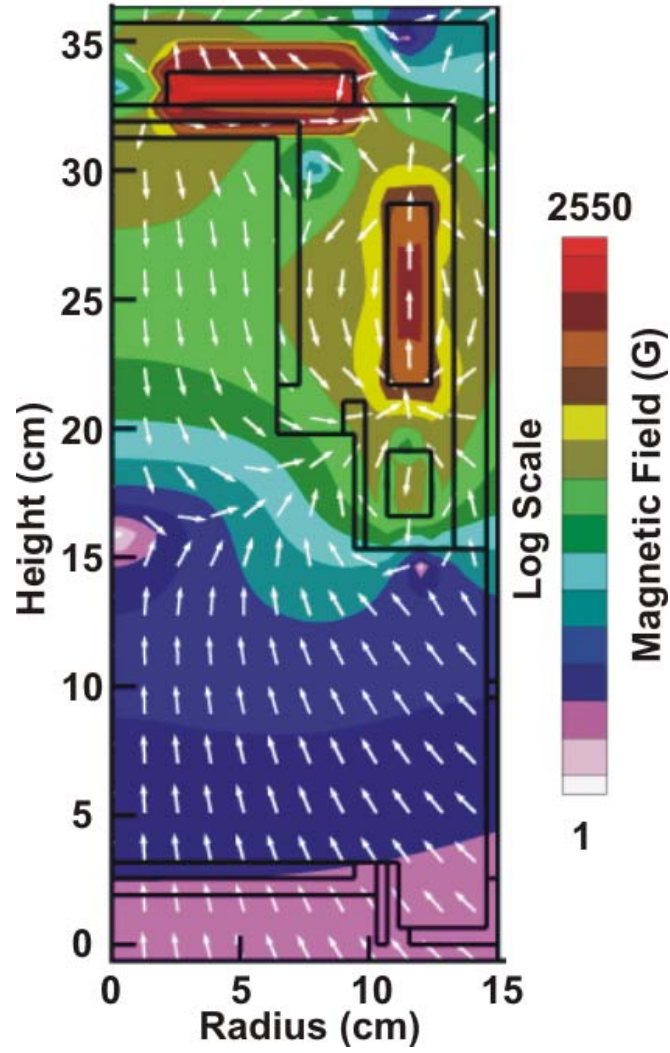


Fig. 5.9. Magnetic field strengths and magnetic flux vectors in a Cu HCM. The presence of magnetic cusp near the target opening helps extract plasma from within the target volume.

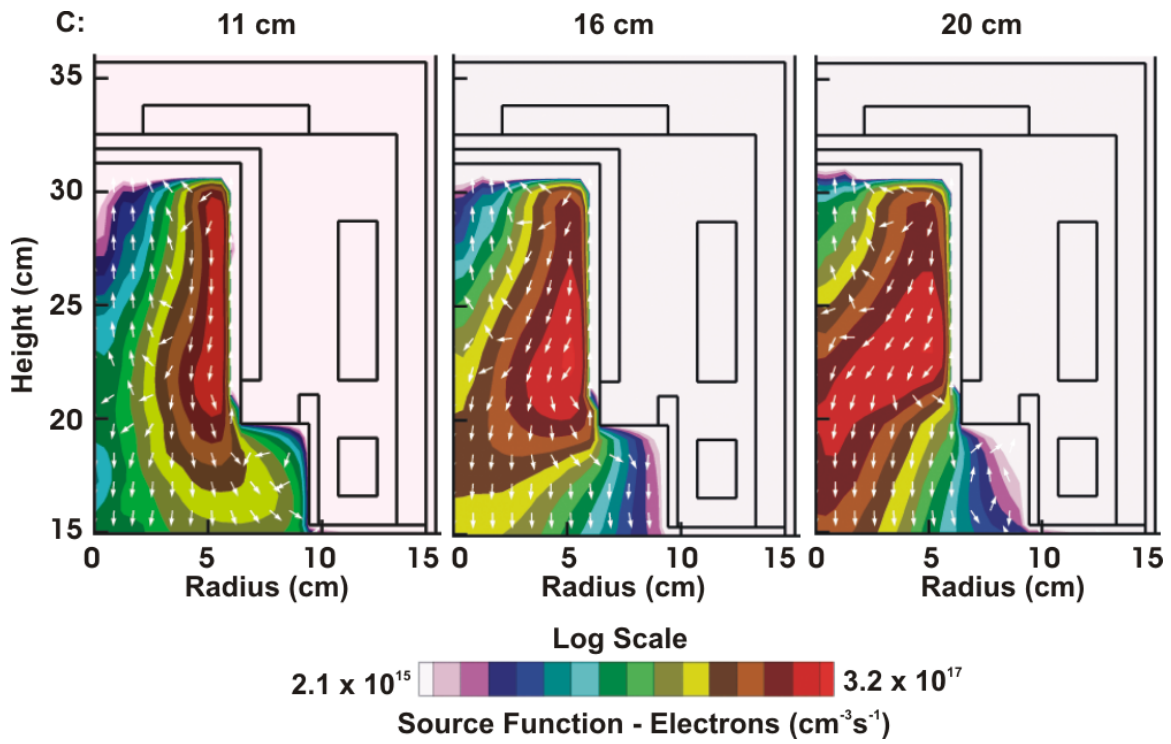


Fig. 5.10. Source function for electrons and the electron flux vectors as a function of magnetic cusp location in a Cu HCM (10 mTorr, 10 kW).

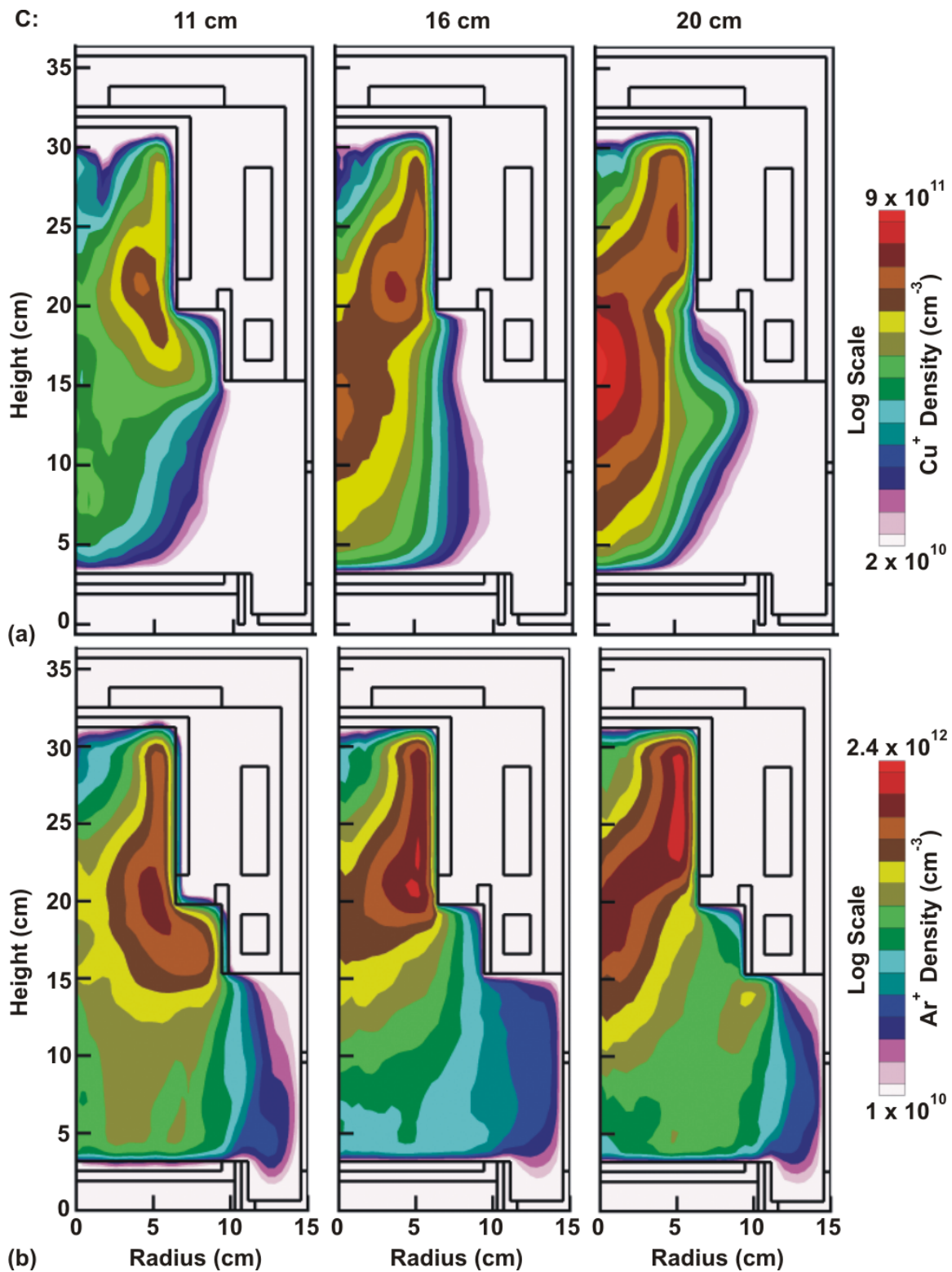


Fig. 5.11. Ion densities as a function of magnetic cusp location in a Cu HCM (10 mTorr, 10 kW). (a) [Cu<sup>+</sup>], and (b) [Ar<sup>+</sup>]. The peak density increases and is more diffuse as the cusp is moved closer to the target opening.

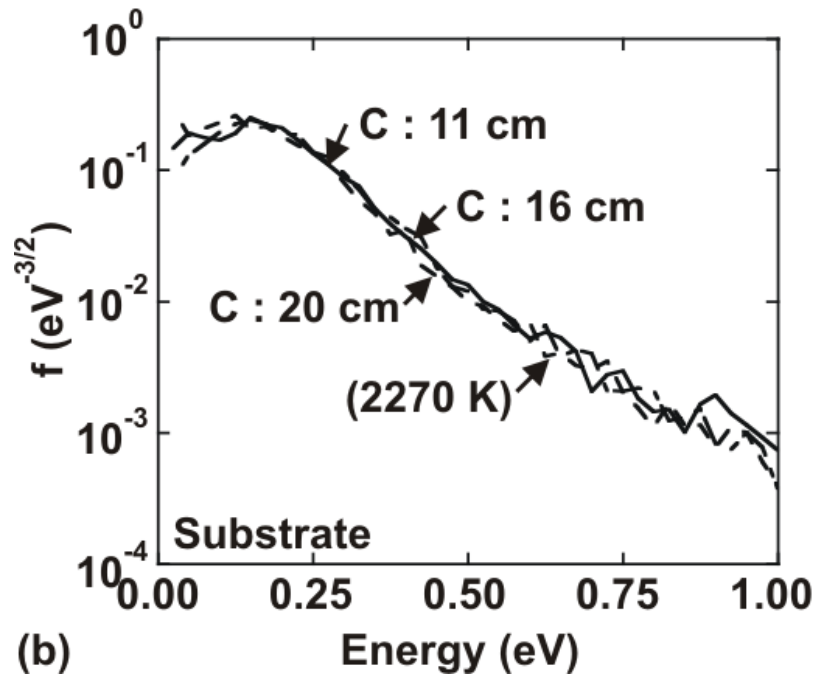
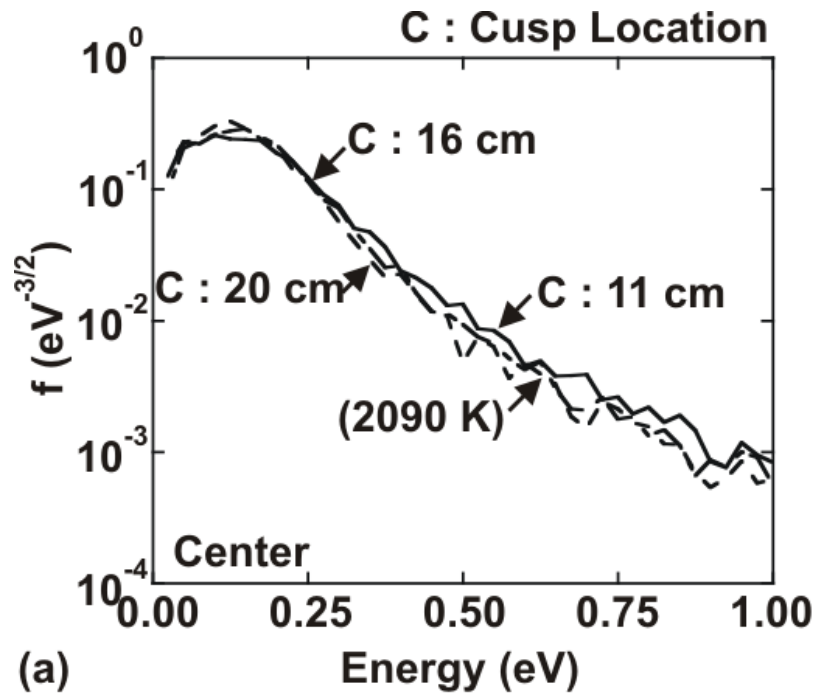


Fig. 5.12. Cu NED as a function of cusp location in a Cu HCM (10 mTorr, 10 kW) at the (a) center of the reactor, and (b) near the substrate.

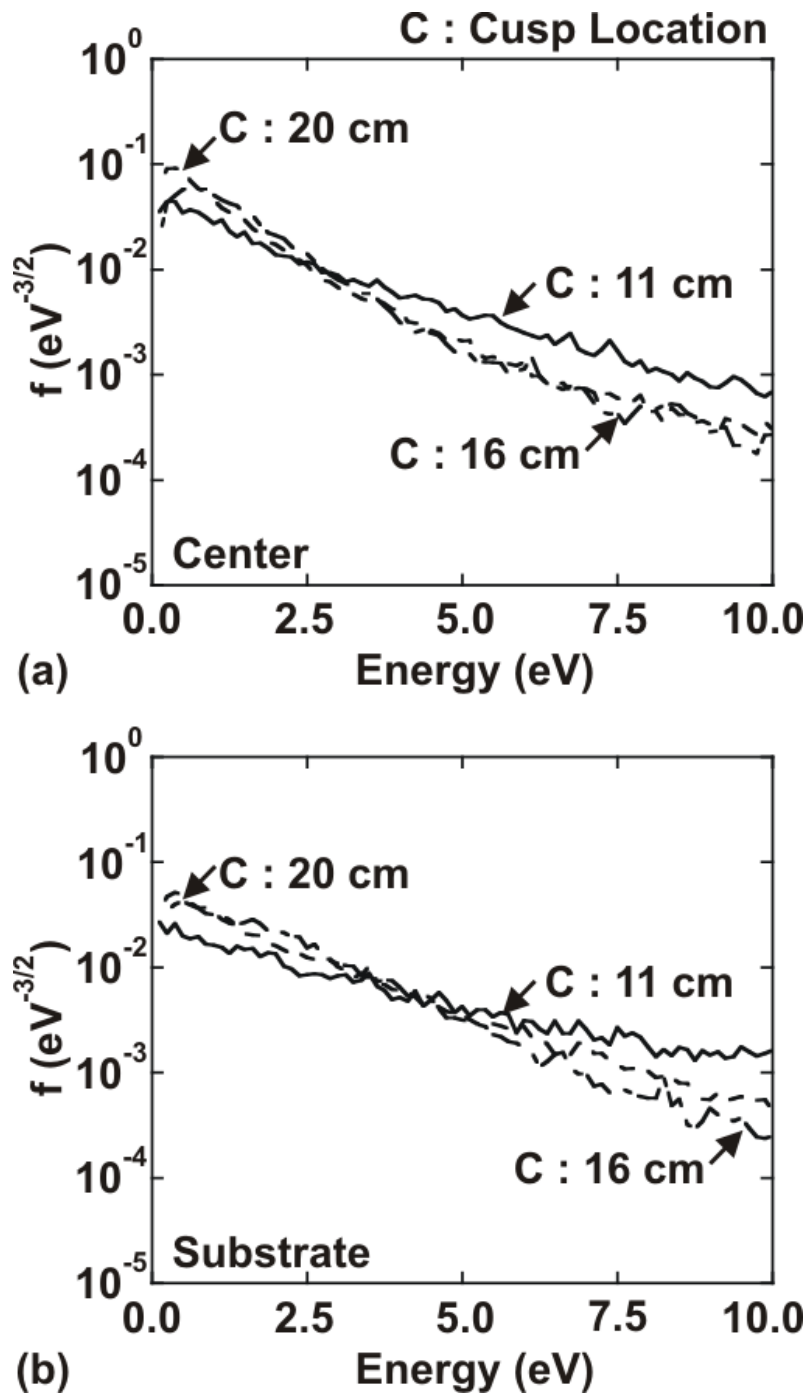


Fig. 5.13. Cu IED as a function of cusp location in a Cu HCM (10 mTorr, 10 kW) at the (a) center of the reactor, and (b) near the substrate.

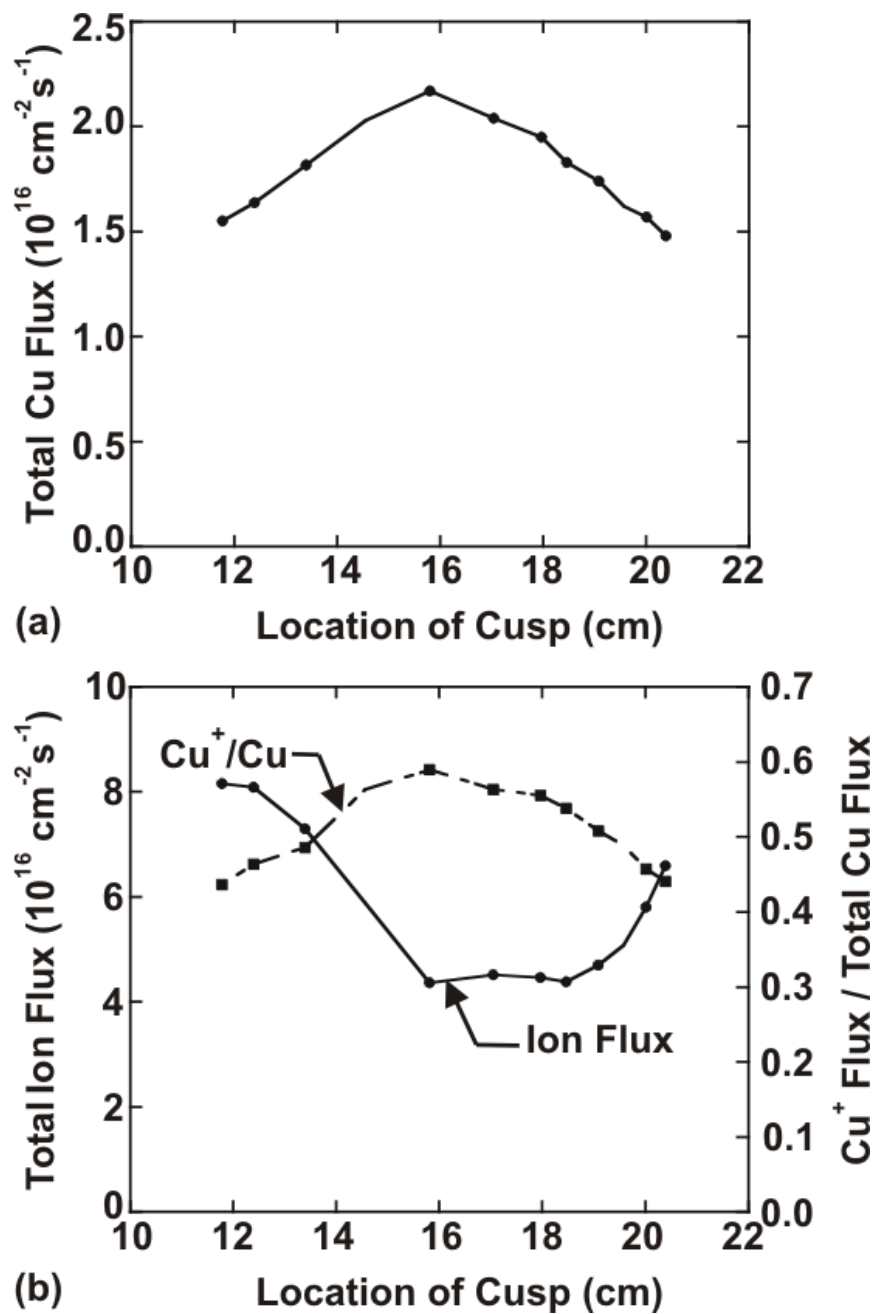


Fig. 5.14. Fluxes incident on the substrate as a function of magnetic cusp location in a Cu HCM (10 mTorr, 10 kW). (a) Total Cu flux, and (b) total ion flux and the ionized fraction of Cu.

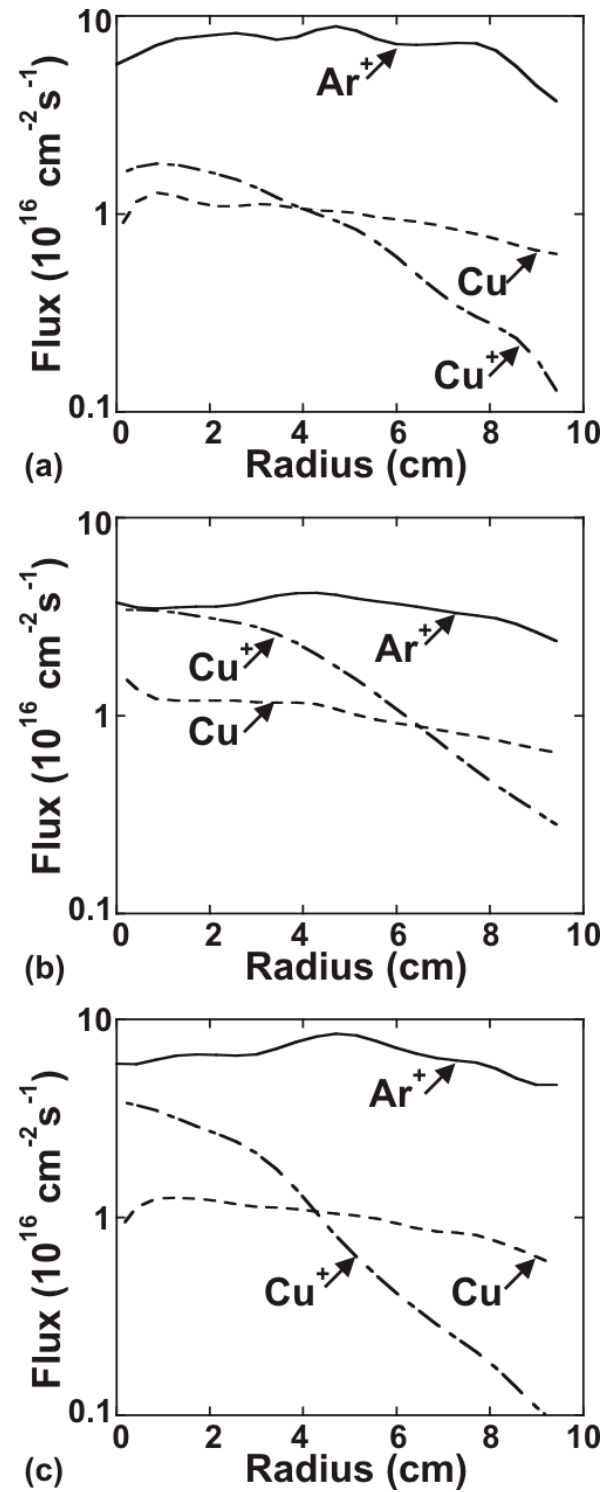
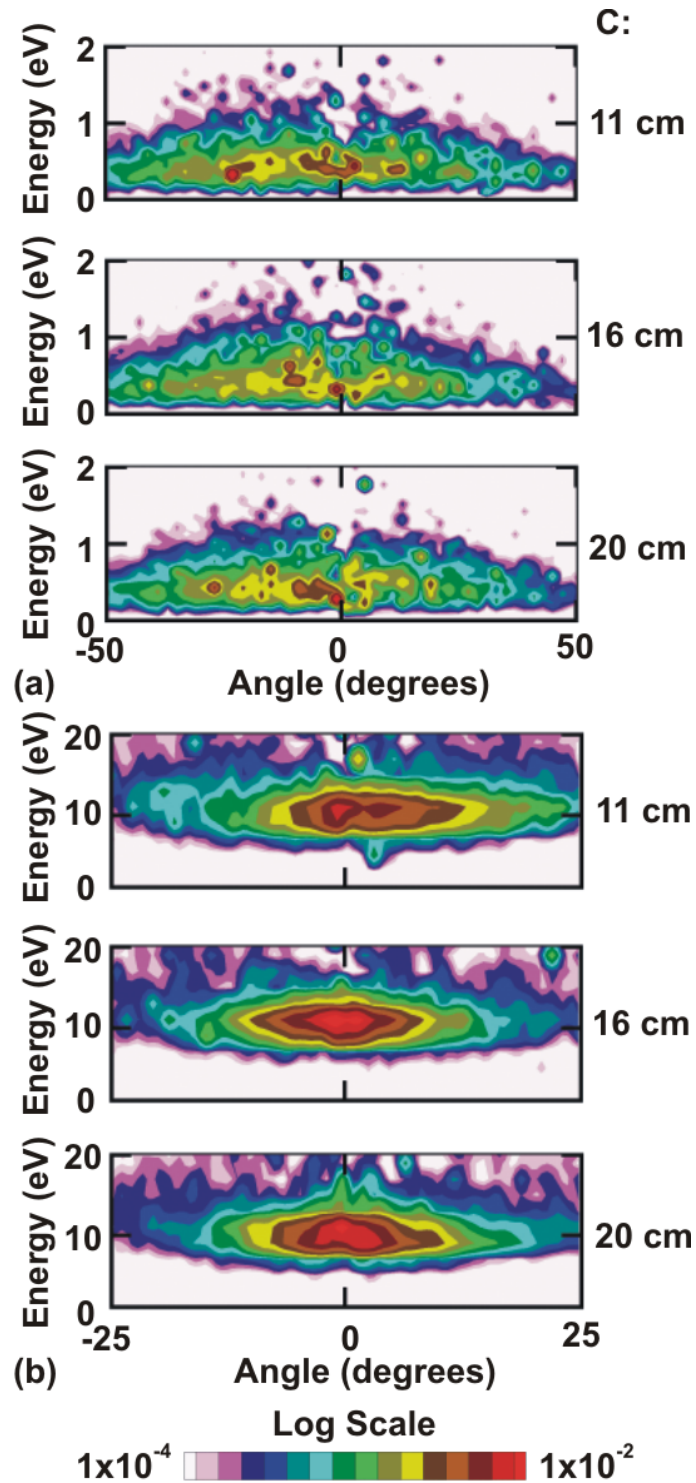


Fig. 5.15. Fluxes incident on the substrate as a function of radius in a Cu HCM (10 kW) for (a)  $C = 11 \text{ cm}$ , (b)  $C = 16 \text{ cm}$ , and (c)  $C = 20 \text{ cm}$ .



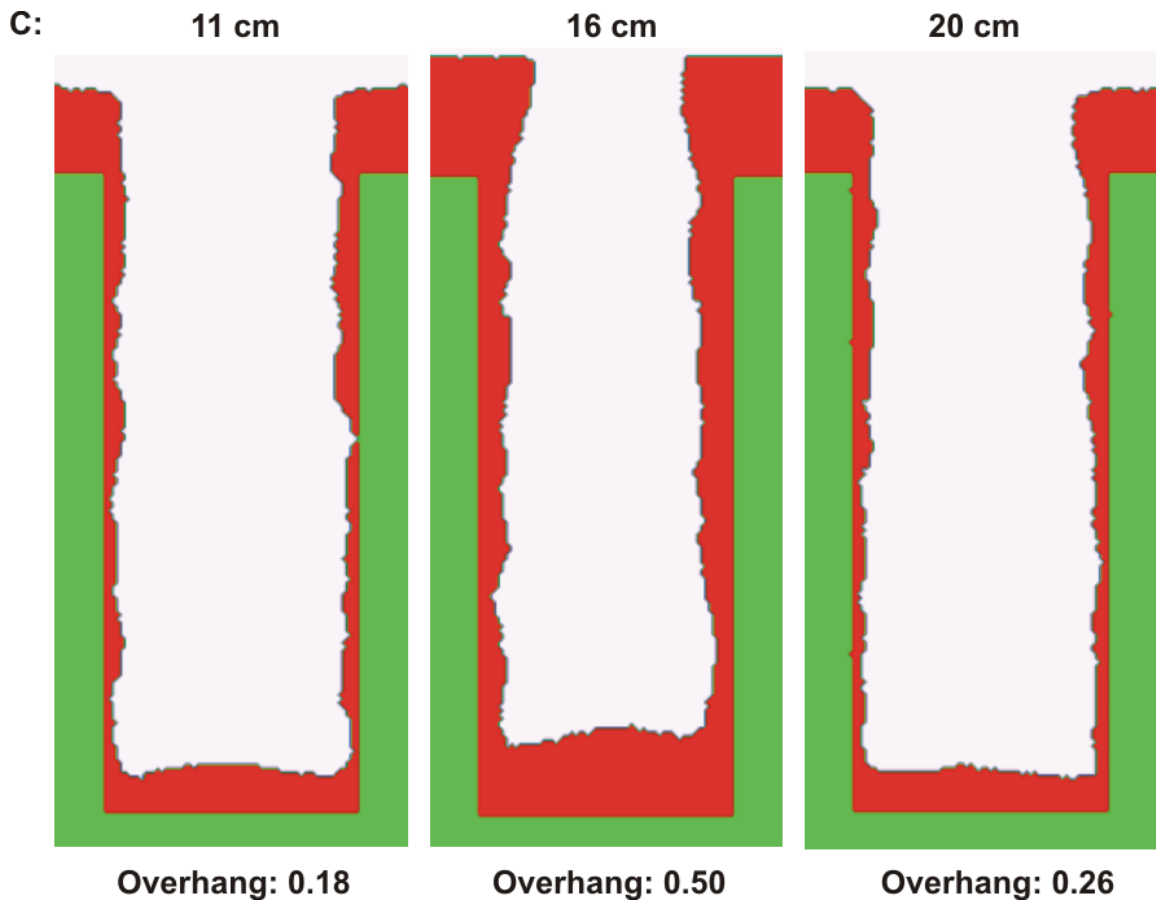


Fig. 5.17. Deposition profiles for a 65 nm feature ( $\beta = 2.5: 1$ ) in a Cu HCM (10 mTorr, 10 kW) as a function of magnetic cusp location. The overhang is a maximum for intermediate cusp locations.

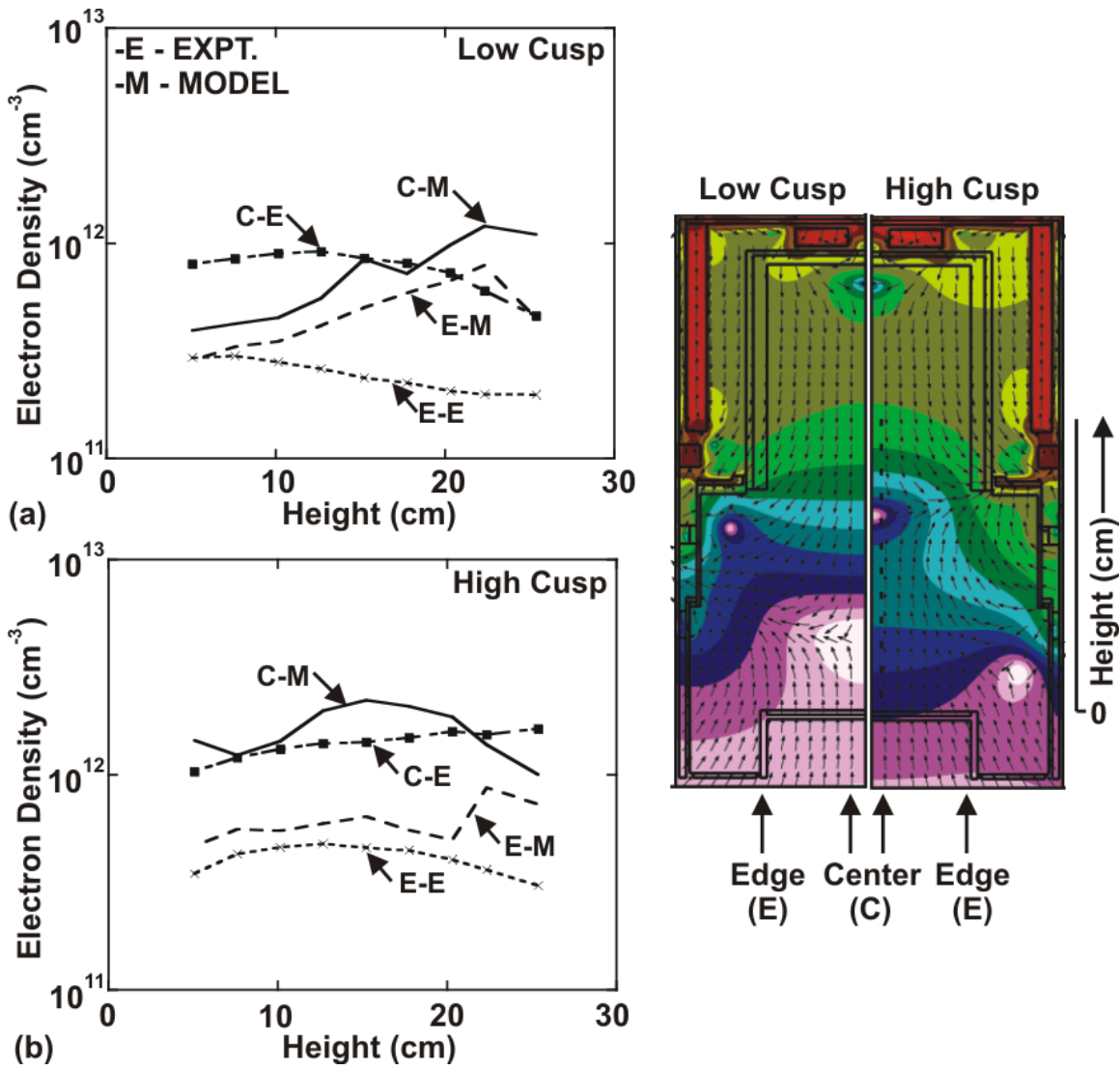


Fig. 5.18. Electron density as a function of height above the substrate in a commercial Cu HCM when the cusp is located (a) near the substrate (low cusp), and (b) near the target opening (high cusp).

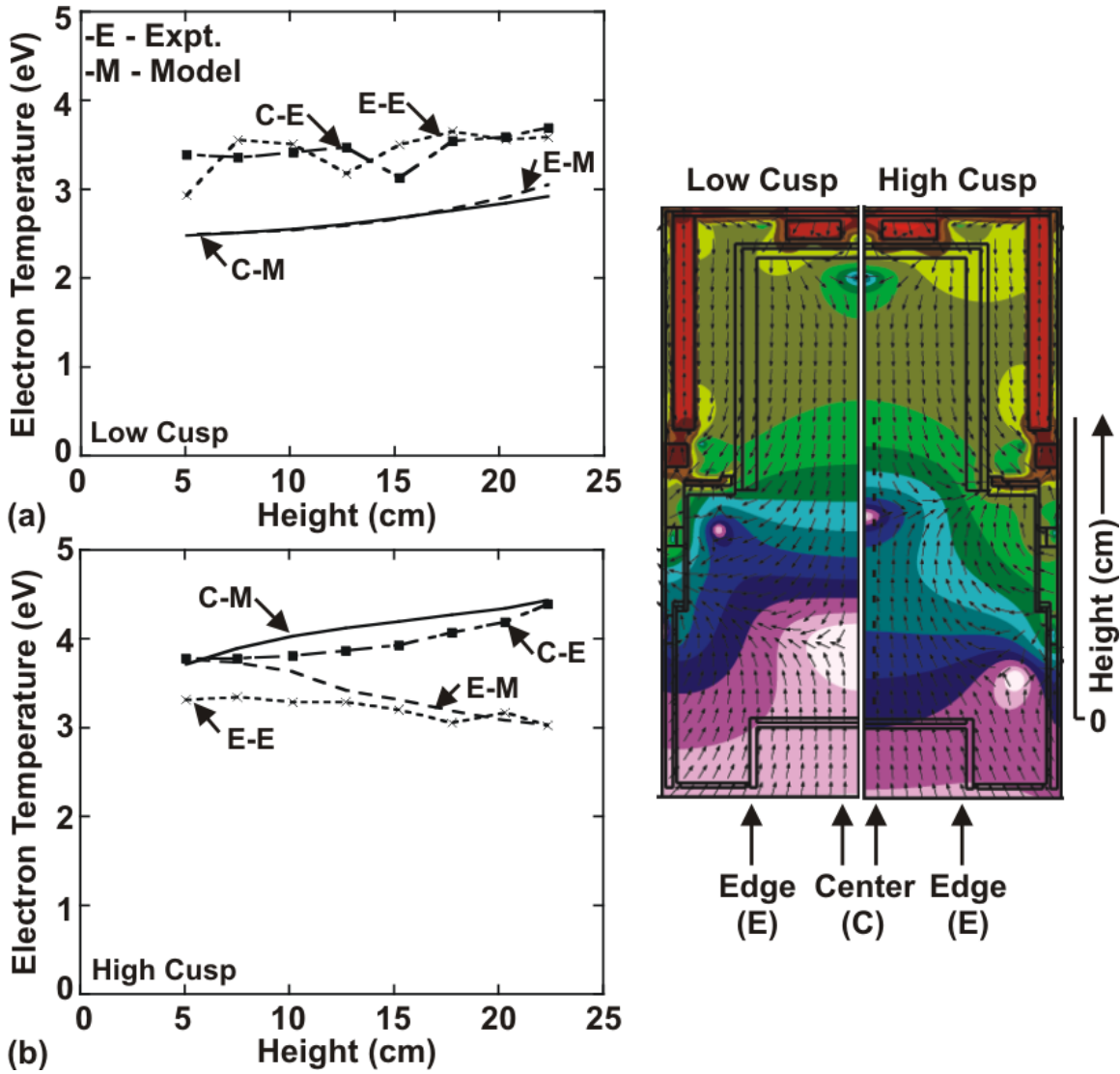


Fig. 5.19. Electron temperature as a function of height above the substrate in a commercial Cu HCM when the cusp is located (a) near the substrate (low cusp), and (b) near the target opening (high cusp).

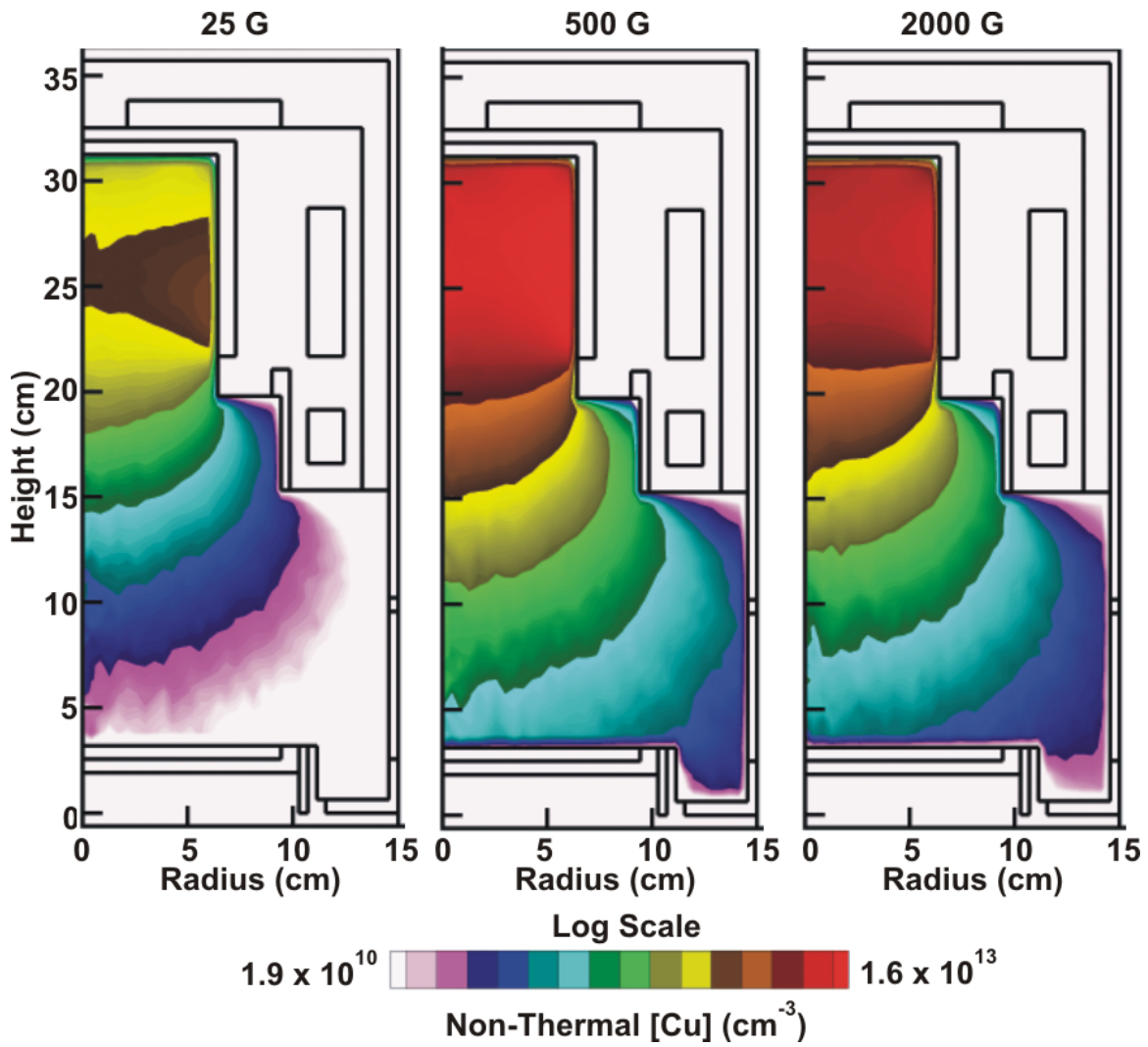


Fig. 5.20. Nonthermal Cu densities as a function of the target surface magnetic field strength ( $B$ ) in a Cu HCM (10 mTorr, - 200 V). The nonthermal Cu density peaks at the Cu target sidewall and moves progressively to higher locations as  $B$  is increased.

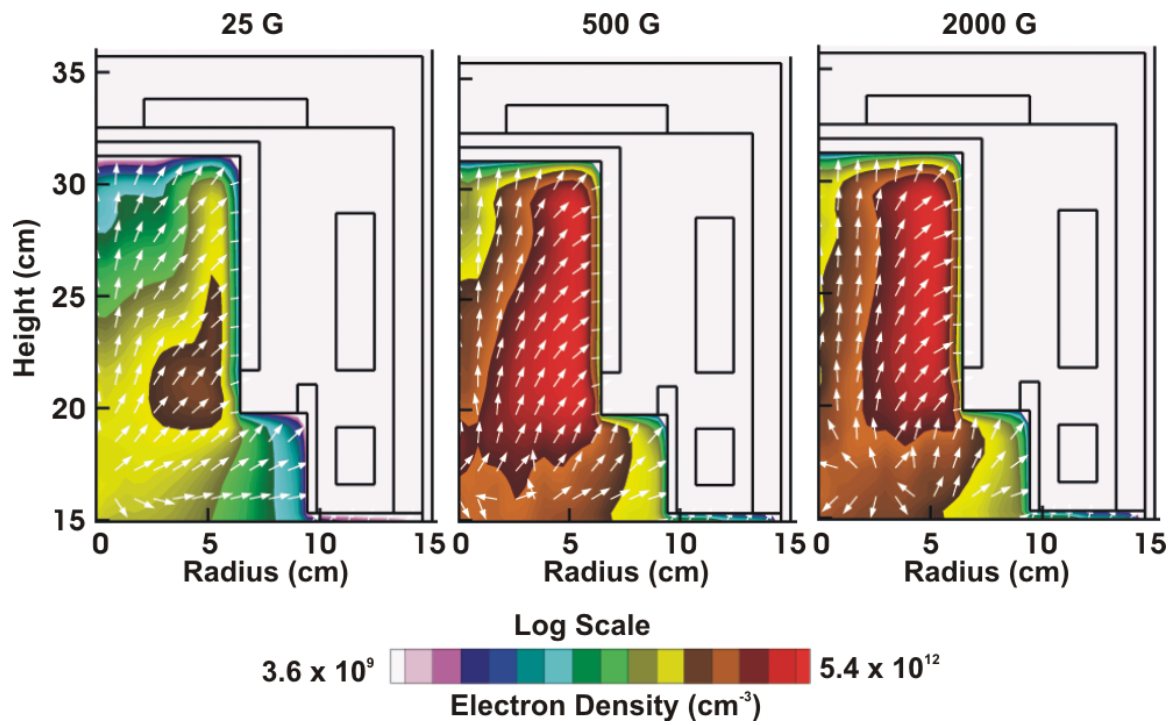


Fig. 5.21. Electron densities and ion-momentum flux vectors as a function of  $B$  in the target region of a Cu HCM (10 mTorr, - 200 V). The electron density is a maximum for  $B = 500$  G and peaks near the target surface. The location of peak in the ion-momentum flux vectors corresponds to the peak in the non-thermal Cu densities.

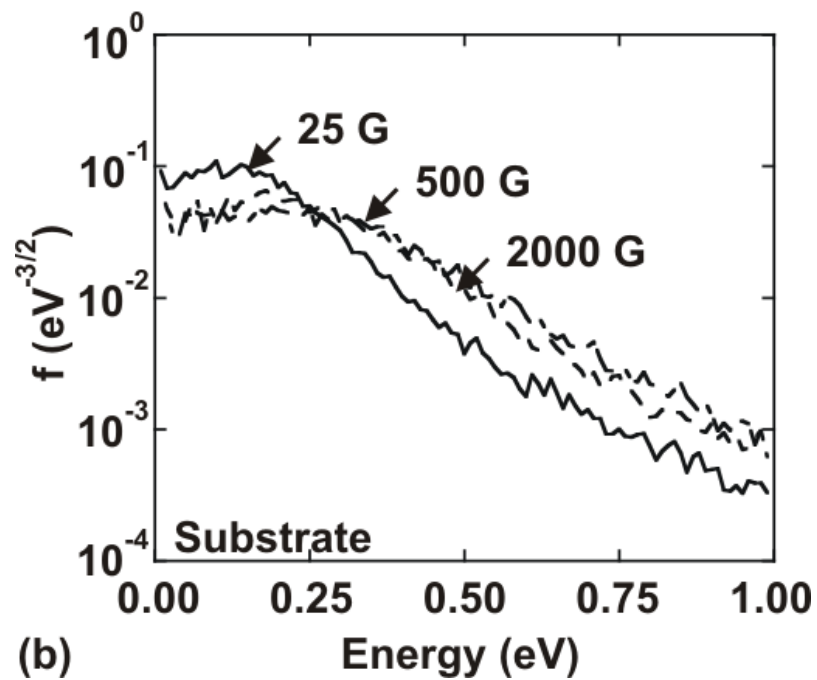
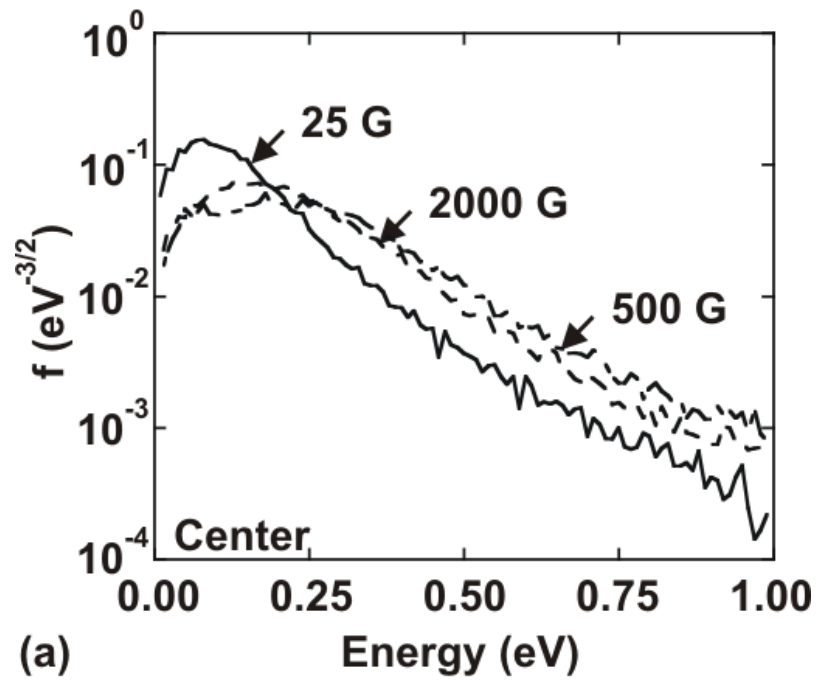


Fig. 5.22. Cu NED as a function of magnetic field strength in a Cu HCM (10 mTorr, -200 V) at the (a) center of the reactor, and (b) near the substrate.

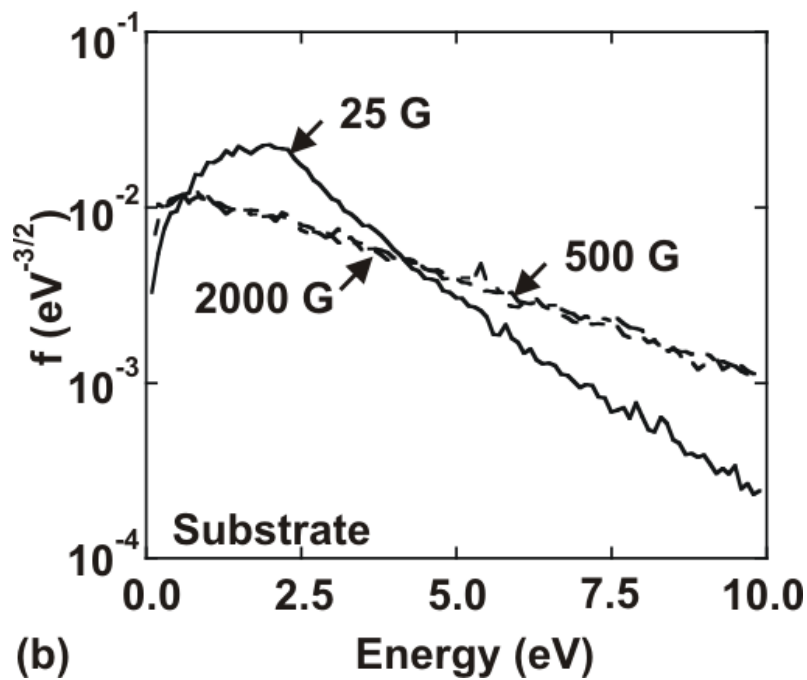
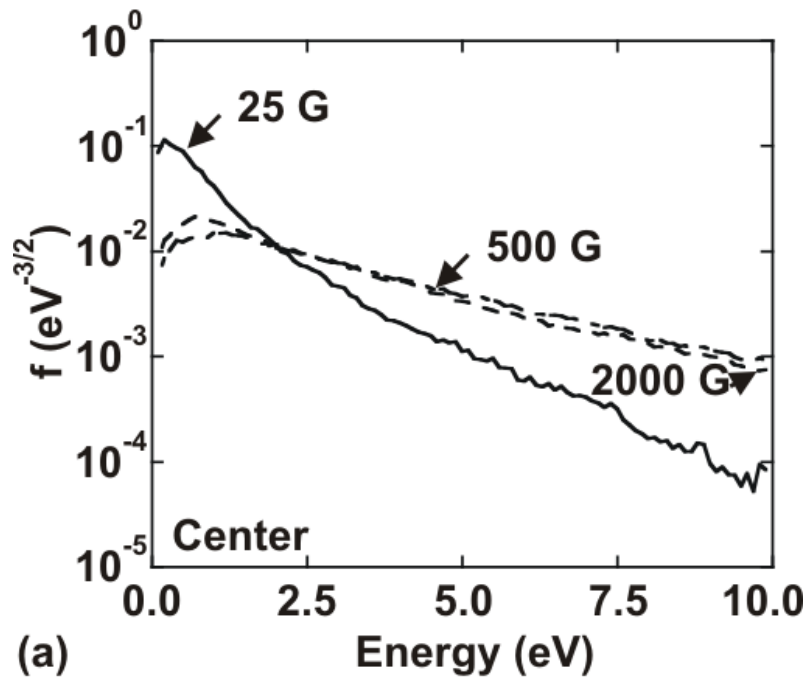


Fig. 5.23 Cu IED as a function of magnetic field strength a Cu HCM (10 mTorr, - 200 V) at the (a) center of the reactor, and (b) near the substrate.

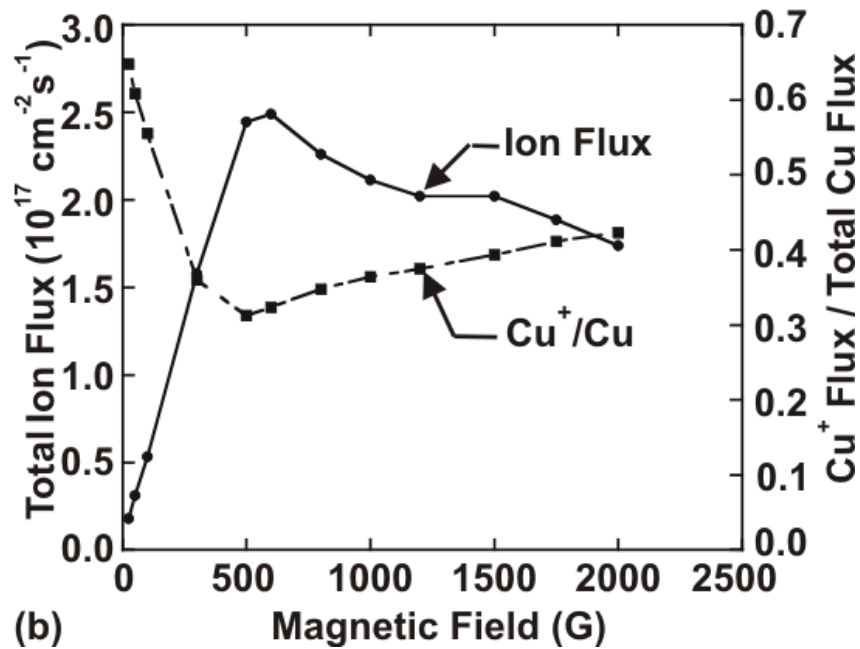
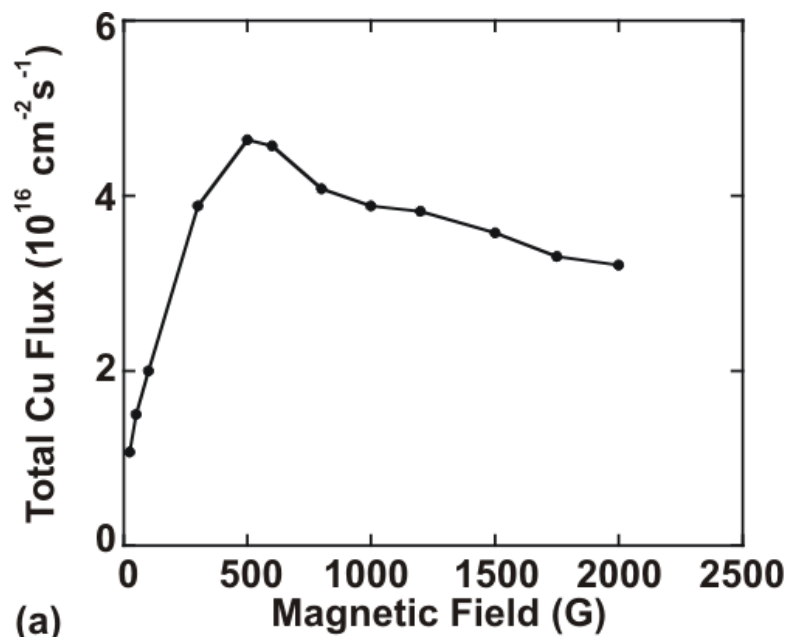


Fig. 5.24. Fluxes incident on the substrate as a function of magnetic field strength in a Cu HCM (10 mTorr, - 200 V). (a) Total Cu flux, and (b) total ion flux and the ionized fraction of Cu.

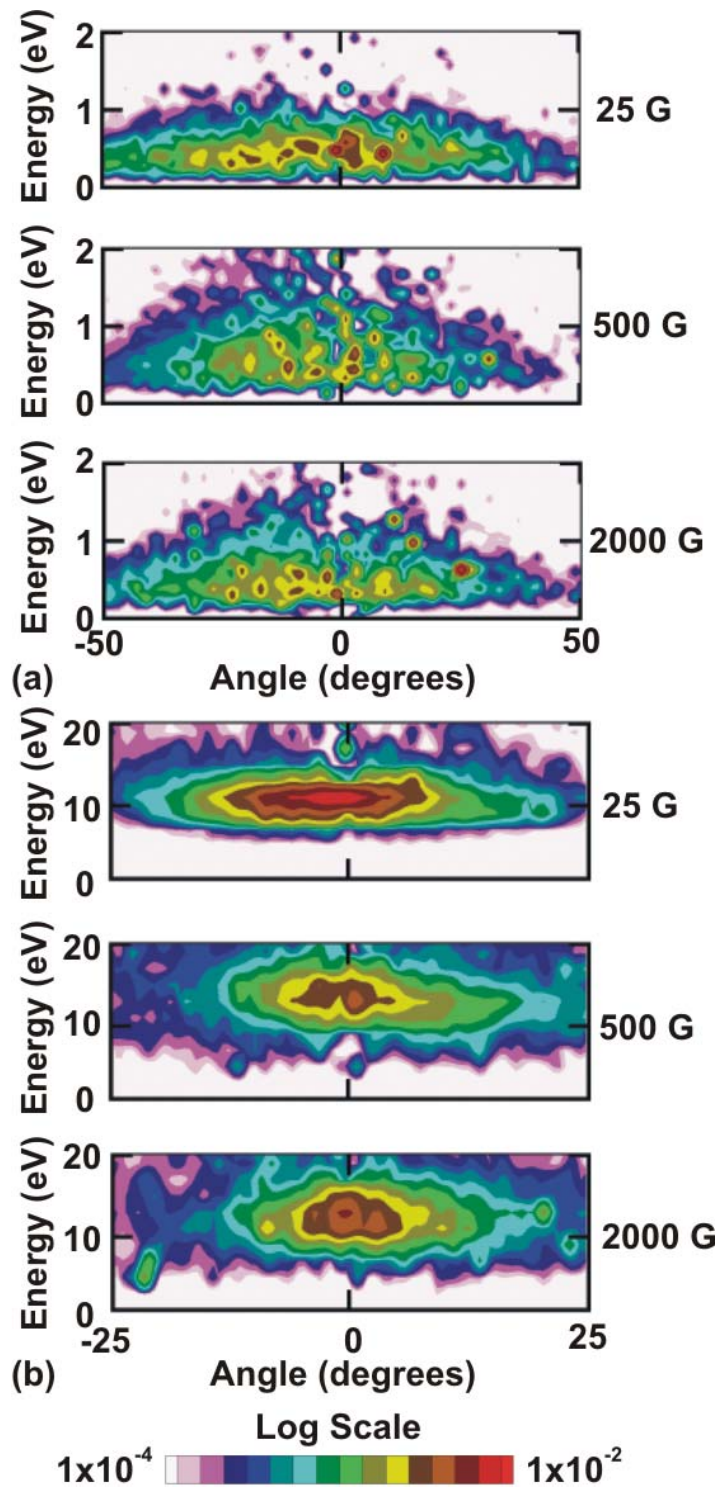


Fig. 5.25. ED incident on and averaged over the wafer as a function of magnetic field strength in a Cu HCM (10 kW) for (a) Cu neutral flux, and (b) total ion flux.

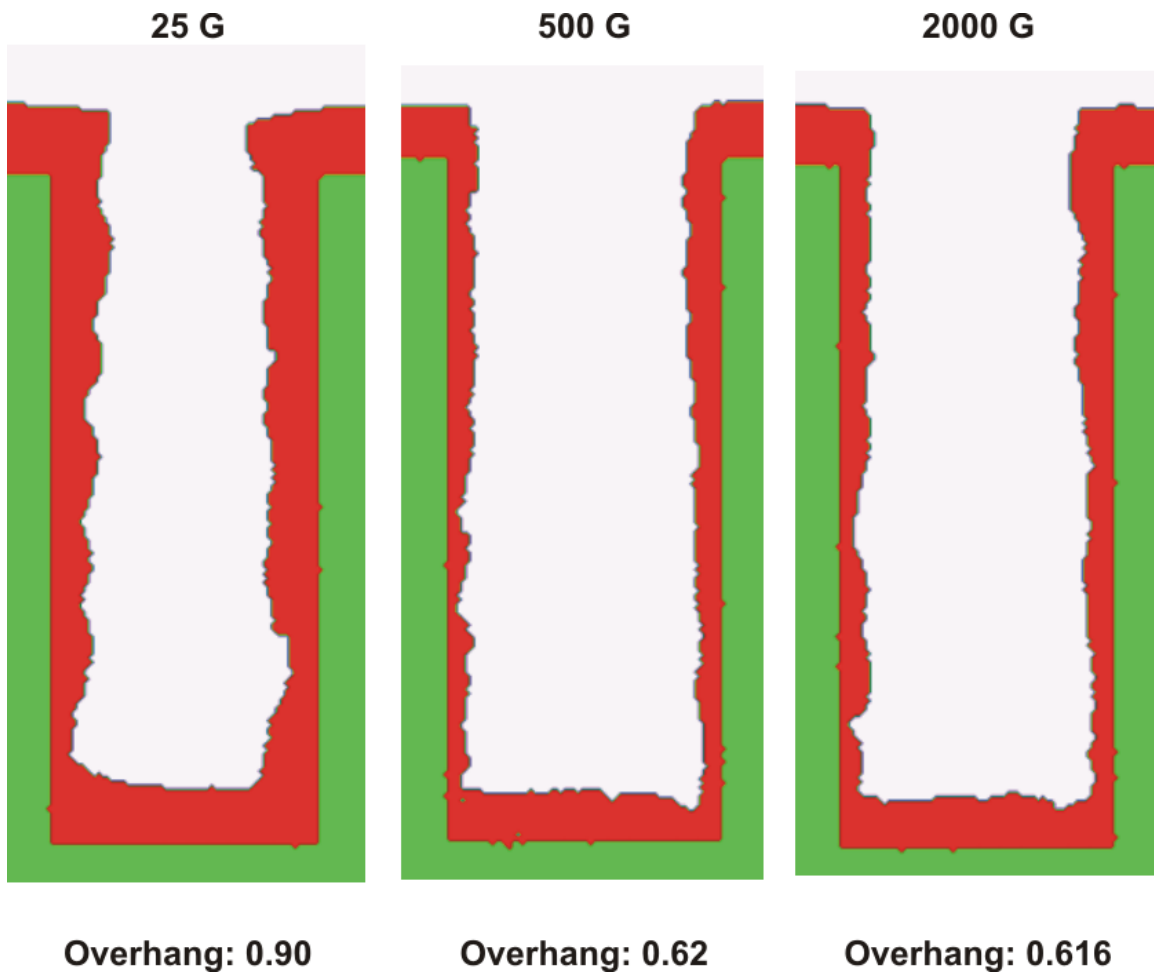


Fig. 5.26. Deposition profiles for a 65-nm feature ( $\beta = 2.5: 1$ ) in a Cu HCM (10 mTorr, -200 V) as a function of magnetic field strength. The overhang is a maximum for  $B = 25$  G corresponding to the broader EADs and a minimum in the total ion flux.

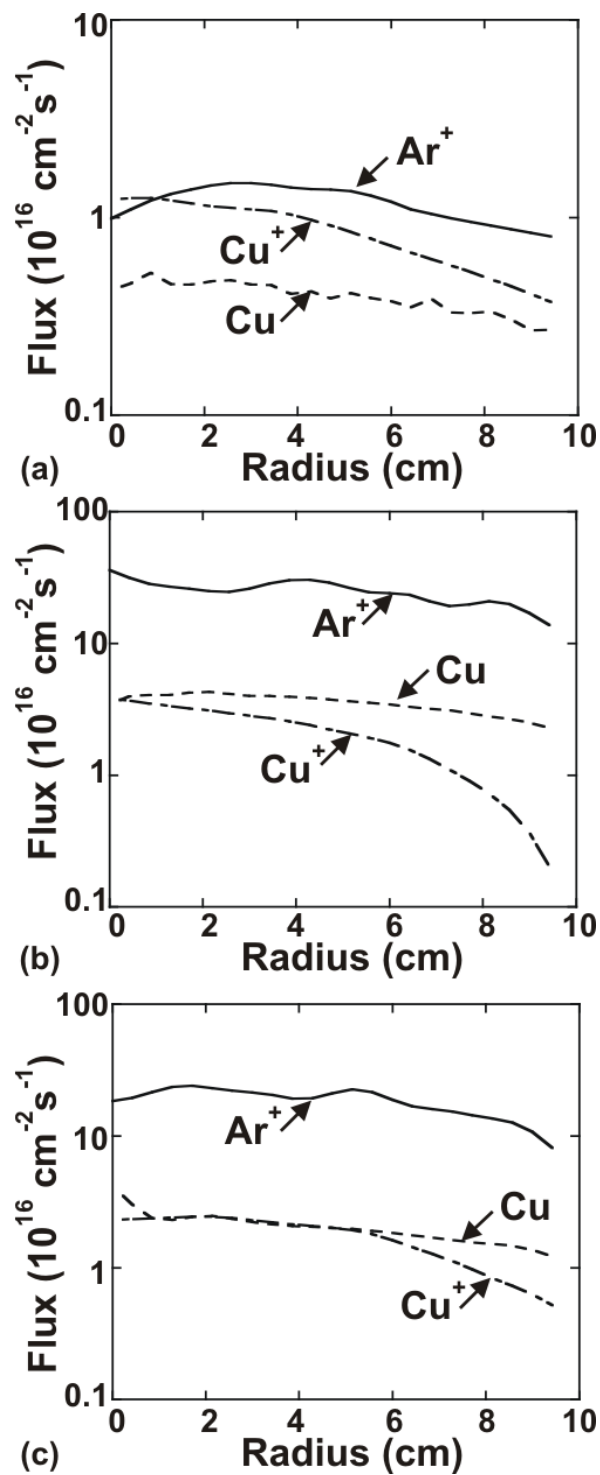


Fig. 5.27. Fluxes incident on the substrate as a function of radius in a Cu HCM (10 mTorr, -200 V) for a magnetic field strength of (a) 25 G, (b) 500 G, and (c) 2000 G.

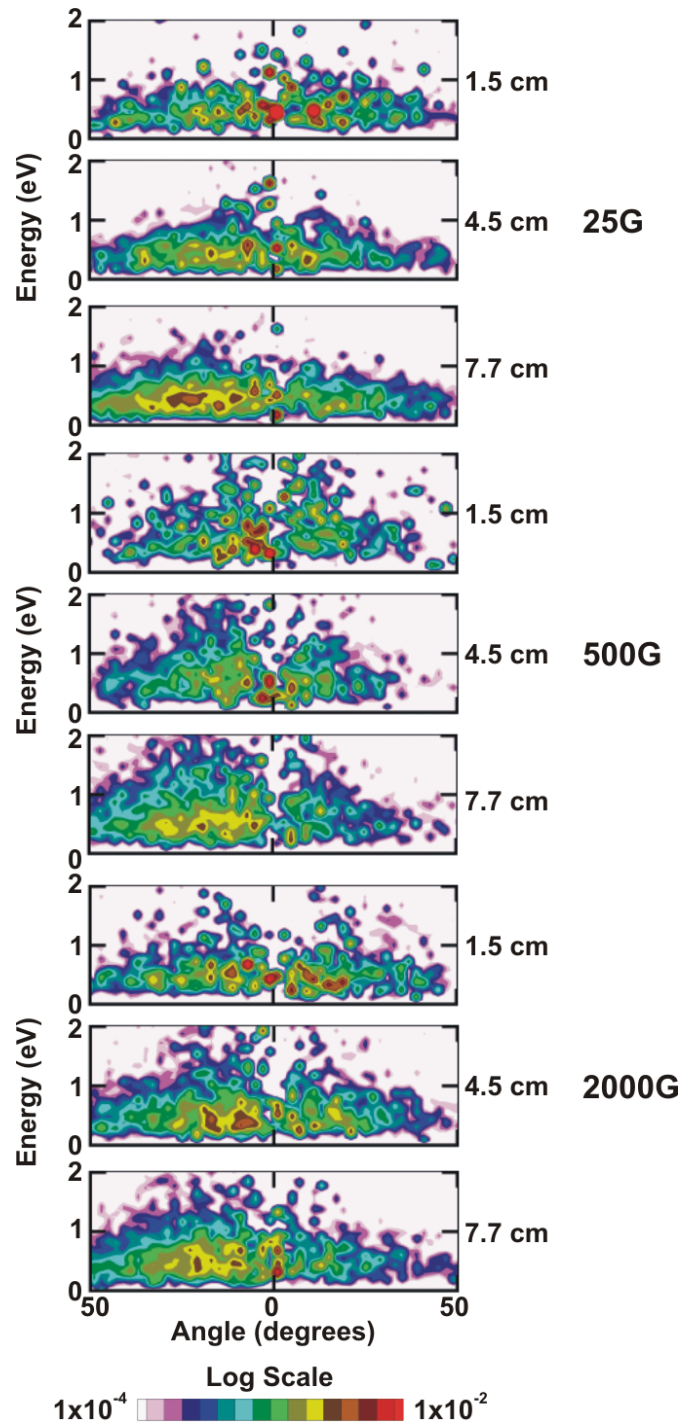


Fig. 5.28. Cu NED as a function of magnetic field and radial position in a Cu HCM (10 kW).

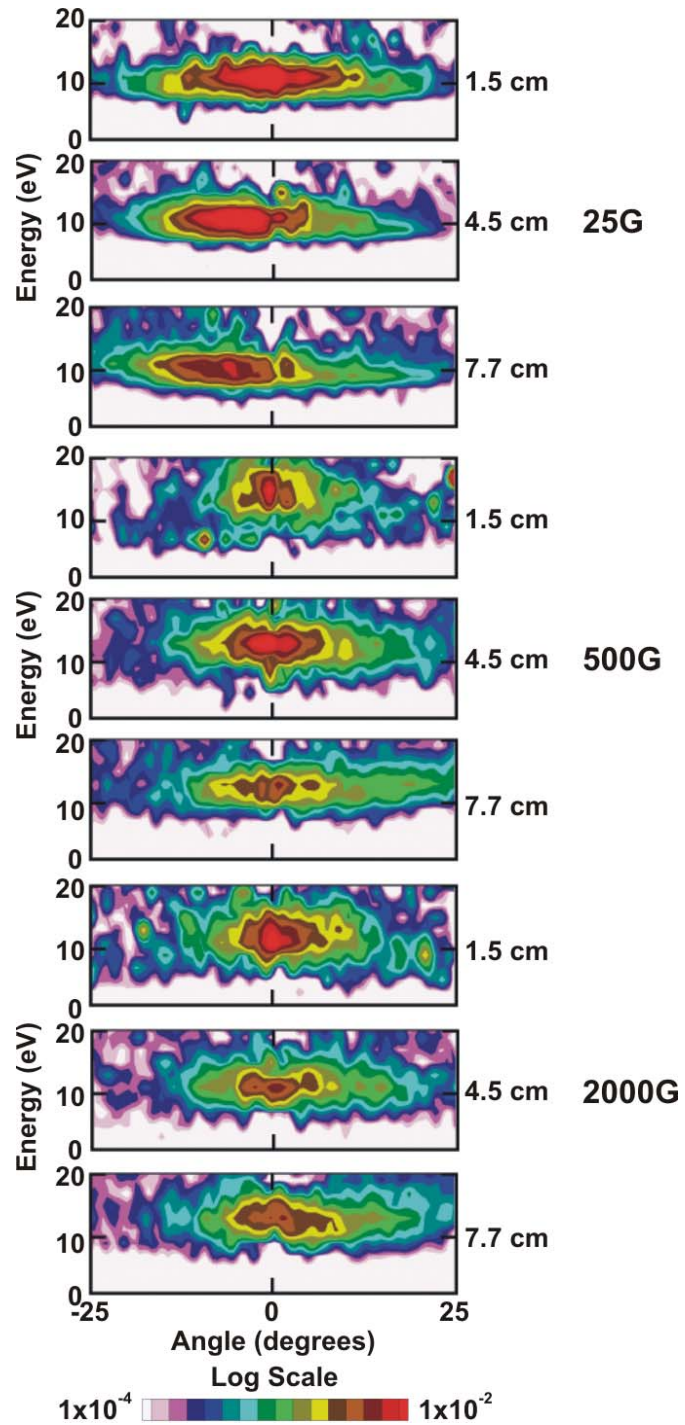


Fig. 5.29. Cu IED as a function of magnetic field and radial position in a Cu HCM (10 kW).

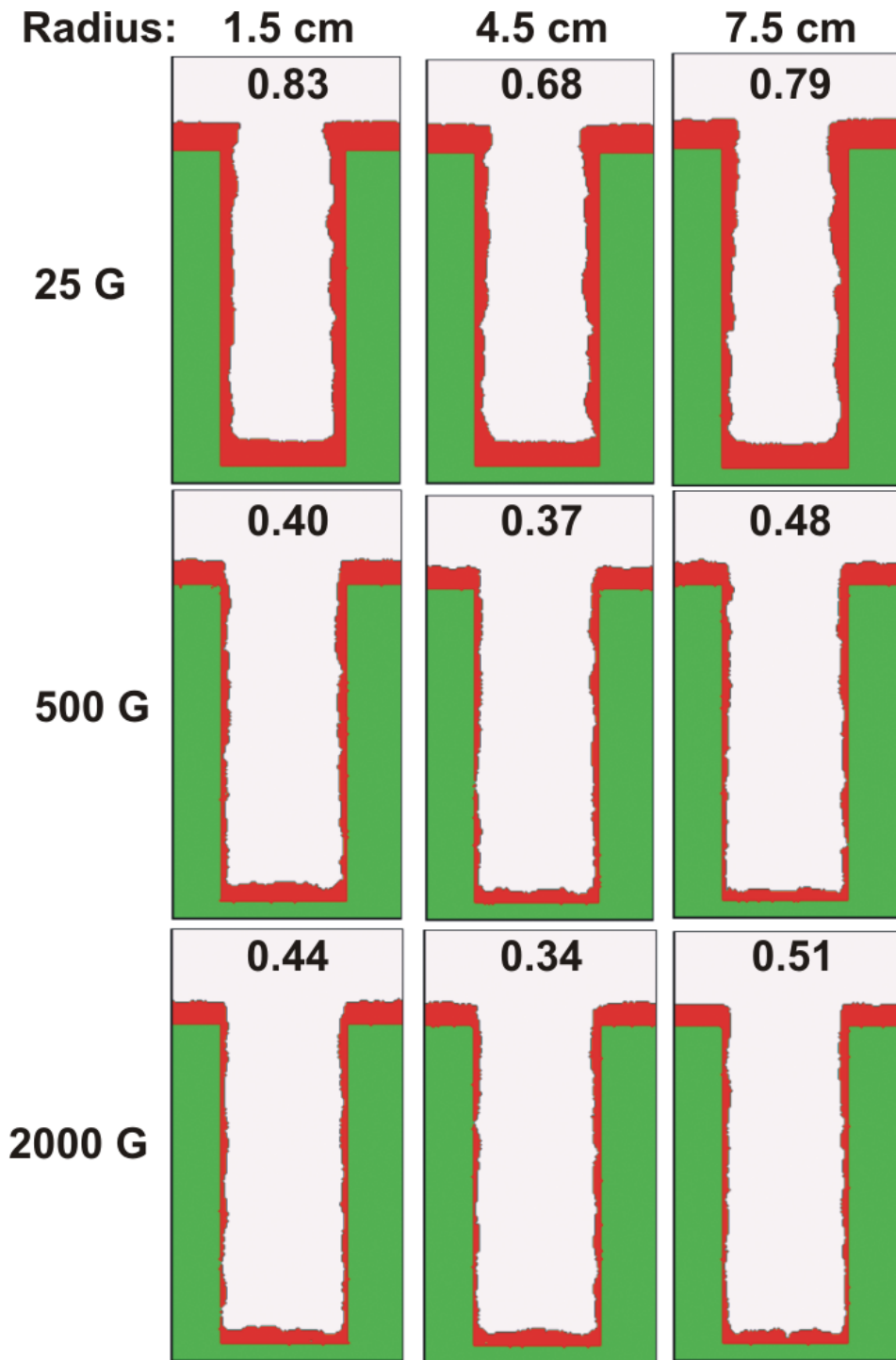


Fig. 5.30. Deposition profiles for a 65-nm feature ( $\beta = 2.5: 1$ ) in a Cu HCM (10 mTorr, -200 V) as a function of magnetic field strength and position. The overhang, as indicated on the profiles, is a minimum for  $B = 25$  G and for intermediate radial positions.

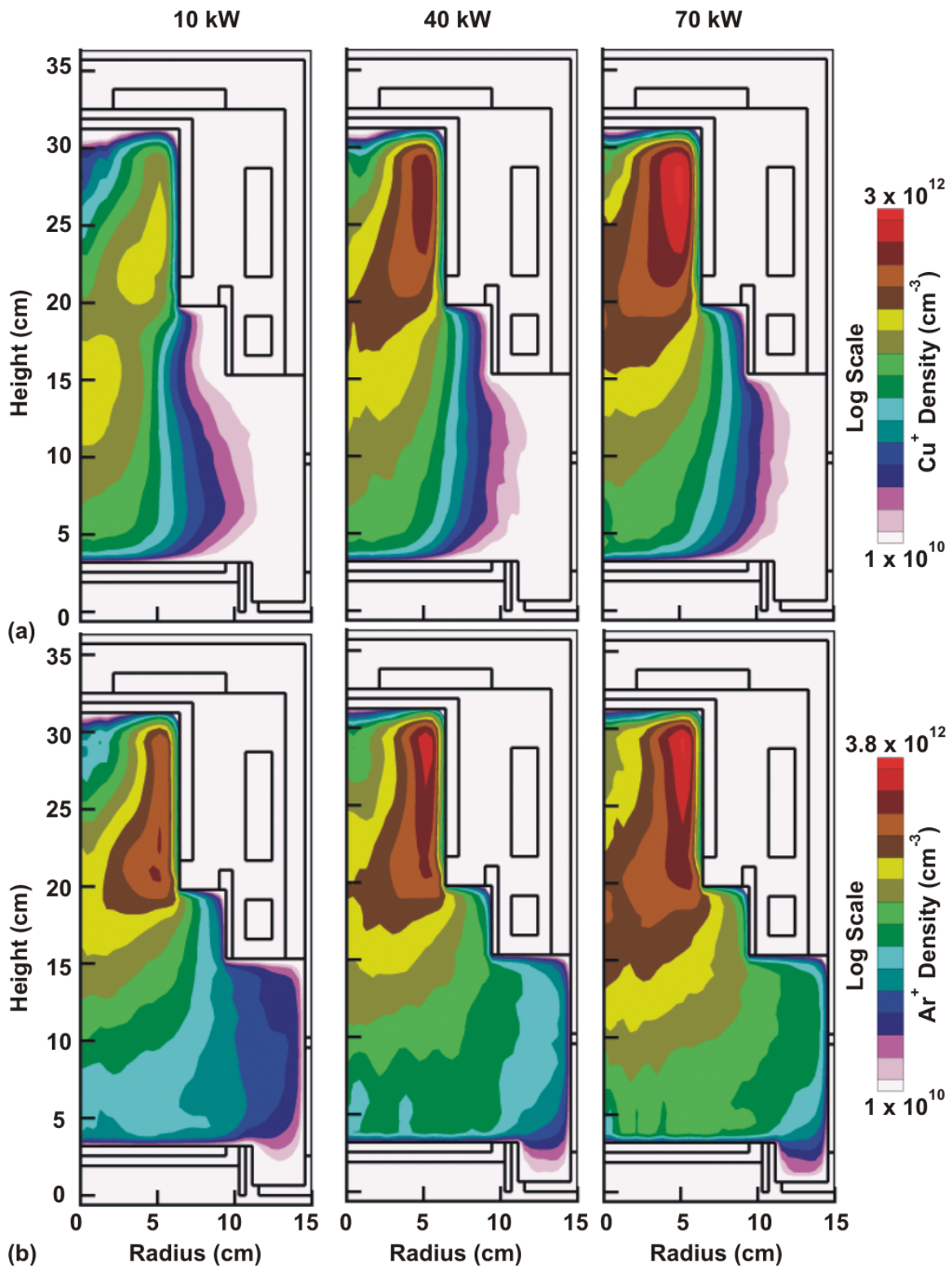


Fig. 5.31. Ion densities as a function of power in a Cu HCM (10 mTorr). (a)  $[\text{Cu}^+]$ , and (b)  $[\text{Ar}^+]$ .

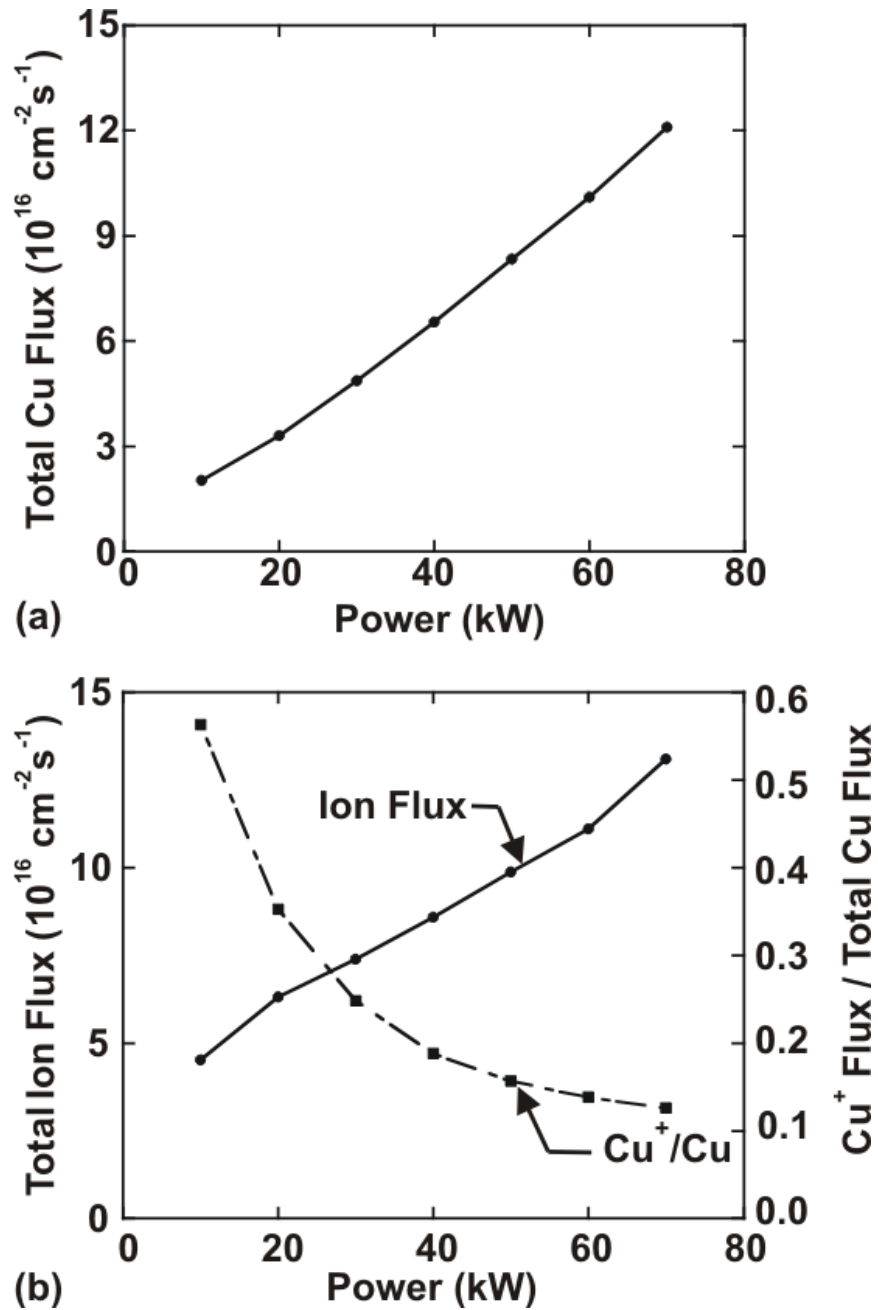


Fig. 5.32. Fluxes incident on the substrate as a function of target power in a Cu HCM (10 mTorr). (a) Total Cu flux, and (b) total ion flux and the ionized fraction of Cu.

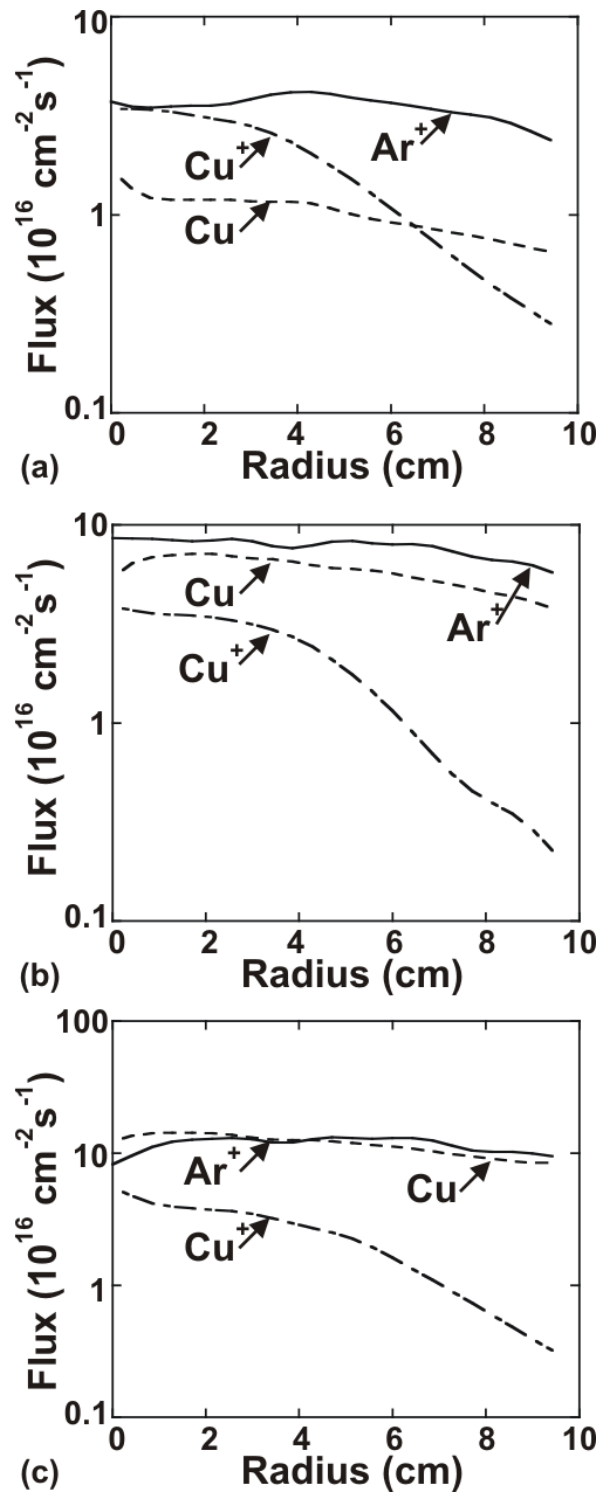


Fig. 5.33. Fluxes incident on the substrate as a function of radius in a Cu HCM (10 mTorr) for a target powers of (a) 10 kW, (b) 40 kW, and (c) 70 kW.

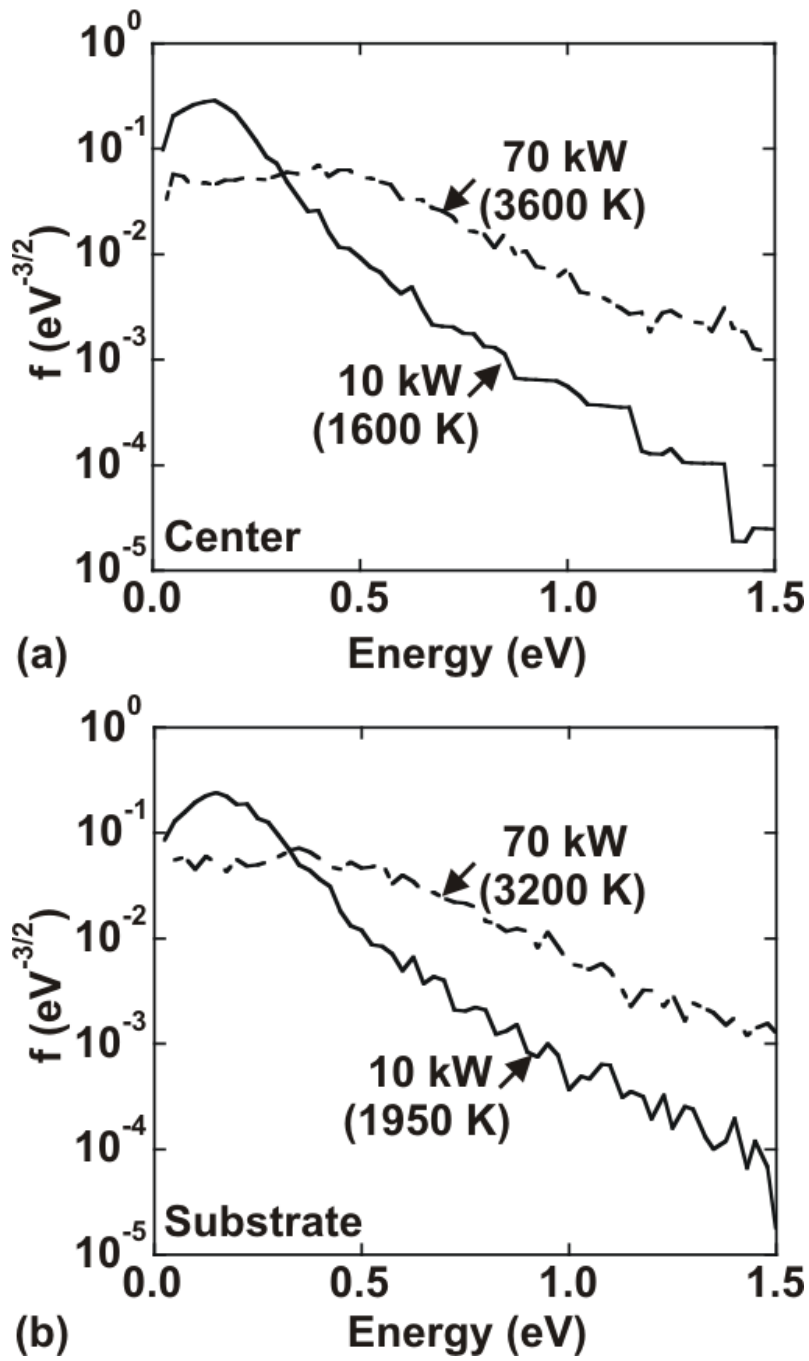


Fig. 34. Cu NED as a function of power in a Cu HCM (10 mTorr) at the (a) center of the reactor, and (b) near the substrate.

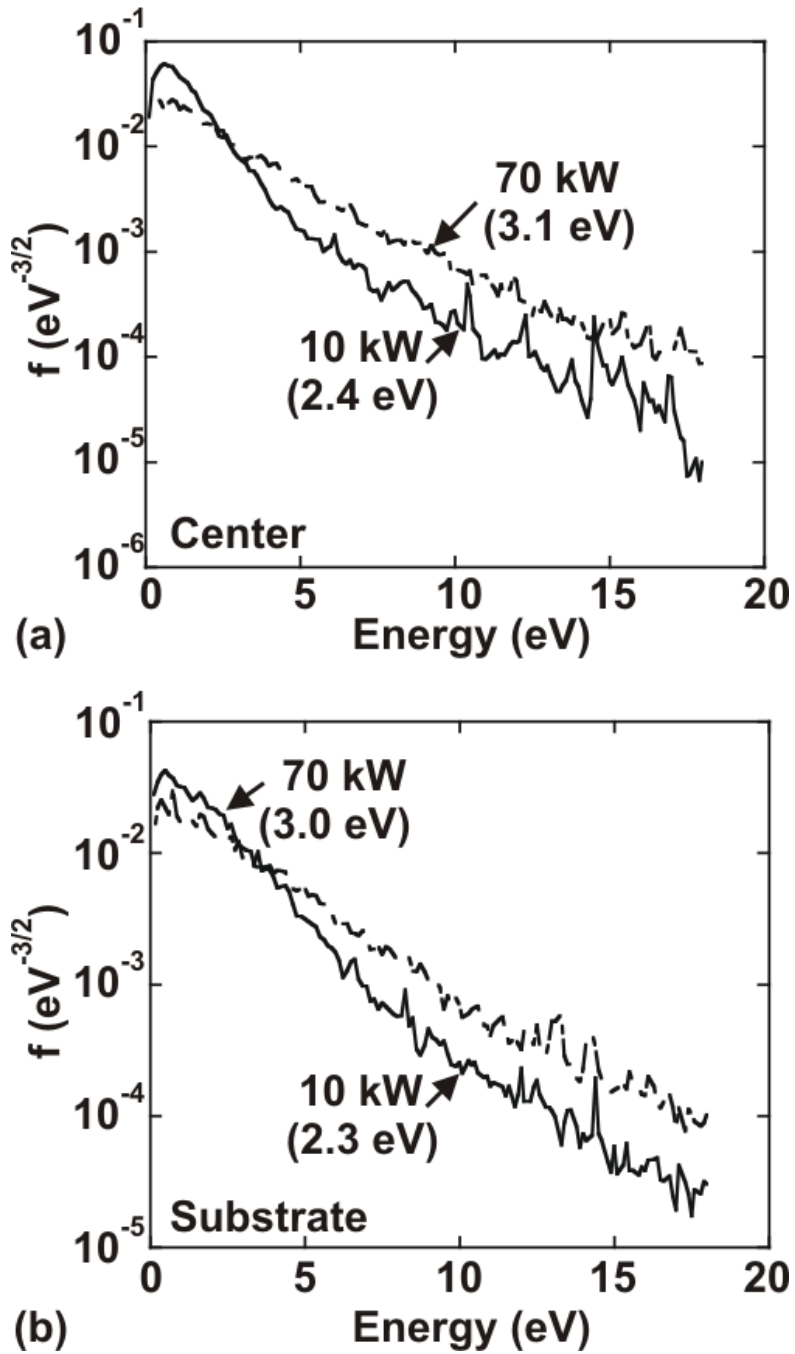


Fig. 35. Cu IED as a function of power in a Cu HCM (10 mTorr) at the (a) center of the reactor, and (b) near the substrate.

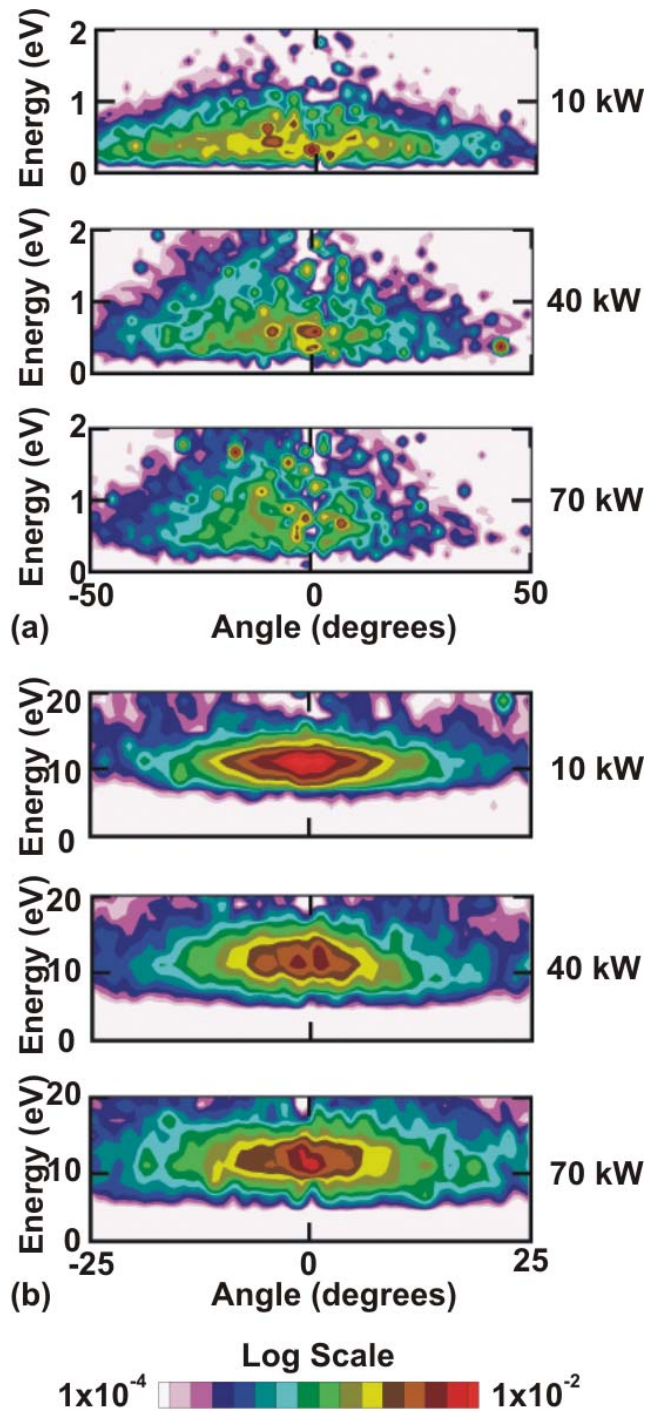


Fig. 5.36. ED incident on and averaged over the wafer as a function of power in a Cu HCM (10 kW) for (a) Cu neutral flux, and (b) Total ion flux.

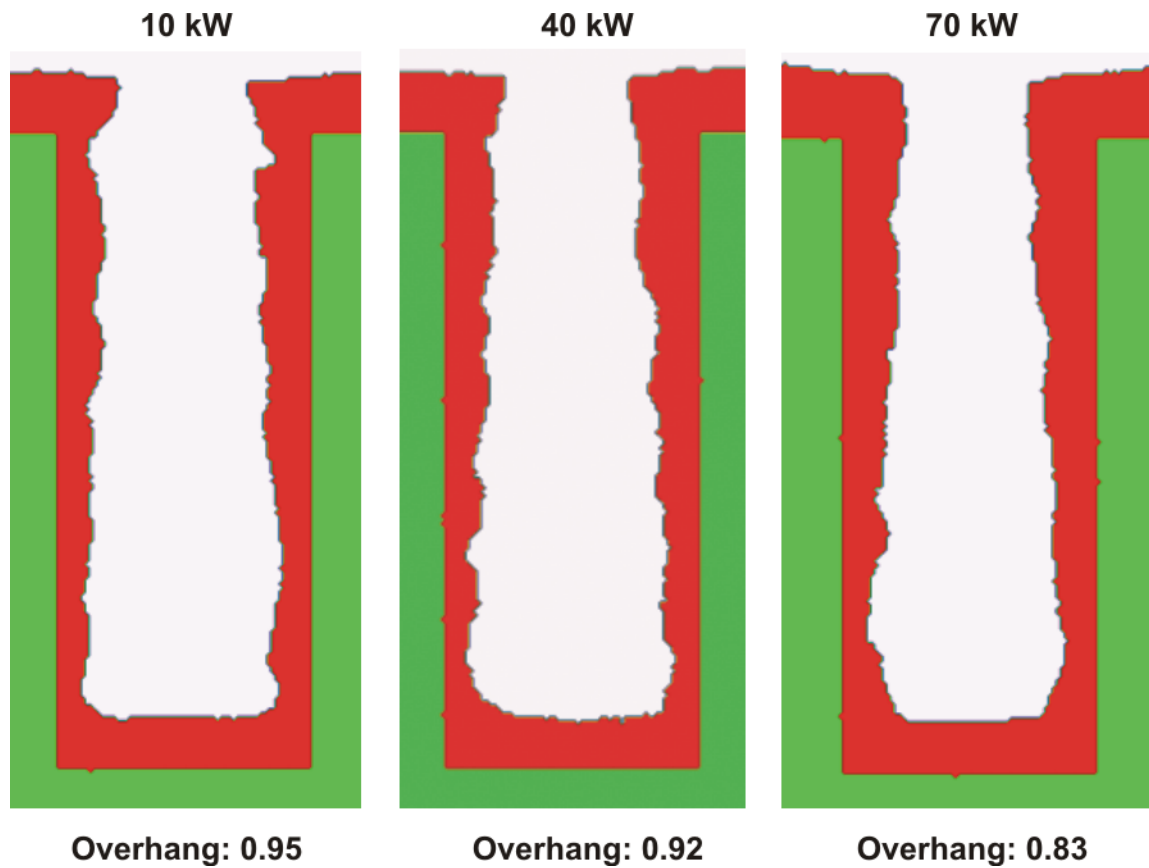


Fig. 5.37. Deposition profiles for a 65-nm feature ( $\beta = 2.5: 1$ ) in a Cu HCM (10 mTorr) as a function of target power. The overhang is a minimum for a target power of 70 kW due to narrower EADs and a maximum in the total ion flux.

## CHAPTER 6

# CONCLUSIONS

Plasma processing of materials is an essential technology for microelectronics fabrication. As plasma processing systems have increased in complexity and cost, it has become prohibitive to develop new reactors by only physical experimentation. The development of plasma equipment models aids in better understanding the complex physical and chemical issues involved in plasma processing of materials and reducing physical development and manufacturing costs. The continuous shrinking of the minimum feature size in microelectronics fabrication has necessitated the use of high-density low-pressure plasma sources. The line of sight transport at these pressures facilitates etching and deposition onto high-aspect ratio features. At these pressures, conventional fluid or hybrid simulations are of questionable validity as transport is highly nonequilibrium and a kinetic approach may be warranted.

In this study, a Monte Carlo simulation for ion and neutral transport (IMCS) has been developed and integrated with a plasma equipment model to improve the capabilities to address lower pressures. The ion/neutral energy distribution functions obtained from the IMCS are used to obtain transport coefficients for use in heavy particle momentum conservation equations. A comparison of the plasma properties obtained using the fluid and the hybrid model has been done. The effect of process conditions on the energy distributions has been investigated. The heavy particle temperatures are found to significantly influence densities, electron temperatures, and sputter rates. The consequences of varying power, pressure, and gas chemistries have been investigated for several low-pressure tools and comparisons have been made to experiments.

Ionized Metal Physical Vapor Deposition (IMPVD) is the technology of choice to extend physical vapor deposition to the 45-nm node. In this work, IMPVD using a hollow

cathode magnetron source has been modeled at the reactor and feature scale. The consequences of varying process parameters such as power, pressure and magnetic fields have been investigated for a hollow cathode magnetron source and comparison has been made with experiments. The gas phase ion and neutral energy distributions are fairly non-Maxwellian, indicative of the non-equilibrium transport in these reactors. The neutral temperatures significantly affect the collisionality of the plasma and consequently the ion and neutral energy distributions on the substrate. The fluxes incident on the wafer are strongly influenced by the magnetic field configuration and strength. The ion flux incident on the wafer increases with pressure due to the larger number of ionizing collisions. The conditions for maximum ion flux on the substrate have been investigated. A Monte Carlo Feature Profile Model has been used to investigate the Cu seed layer deposition process. The lateral overburden at the mouth of features or “overhang” strongly correlates to the ion and neutral energy and angular distributions and the ion flux incident on the substrate.

## APPENDIX A: SURFACE REACTIONS FOR Cu DEPOSITION IN Ar BUFFER GAS

Reaction <sup>a</sup>	Probability	E <sub>th</sub> , E <sub>r</sub> , n <sup>b</sup>	Footnote
$\text{Ar}^+ + \text{Cu}_s \rightarrow \text{Ar}_g + \text{Cu}_g$	0.35	45, 100, 1	
$\text{Ar}^+ + \text{SiO}_{2s} \rightarrow \text{Ar}_g + \text{SiO}_{2g}$	0.10	45, 100, 0.5	
$\text{Cu}^+ + \text{Cu}_s \rightarrow \text{Cu}_g + \text{Cu}_g$	0.35	45,100, 1	
$\text{Cu}^+ + \text{Cu}_s \rightarrow \text{Cu}_s + \text{Cu}_s$	0.55		c,d
$\text{Cu}^+ + \text{Cu}_s \rightarrow \text{Cu}_g + \text{Cu}_s$	0.10		c,d
$\text{Cu}^+ + \text{SiO}_{2s} \rightarrow \text{Cu}_g + \text{SiO}_{2g}$	0.10	45,100,0.5	
$\text{Cu}^+ + \text{SiO}_{2s} \rightarrow \text{Cu}_s + \text{SiO}_{2s}$	0.80		c,d
$\text{Cu}^+ + \text{SiO}_{2s} \rightarrow \text{Cu}_s + \text{SiO}_{2g}$	0.10		c,d
$\text{Cu}_g + \text{Cu}_s \rightarrow \text{Cu}_s + \text{Cu}_s$	0.95		d
$\text{Cu}_g + \text{SiO}_{2s} \rightarrow \text{Cu}_s + \text{SiO}_{2s}$	0.70		d

<sup>a</sup> All ion reactions also apply to hot neutrals and reflected neutrals having high energy.

<sup>b</sup> Threshold and reference energies are in eVs.

<sup>c</sup> See Eq. (3.5).

<sup>d</sup> Estimated [1].

<sup>e</sup> s refers to surface species and g refers to gas species.

### A.1 References

[1] J. Lu and M. J. Kushner, J. Vac. Sci. Technol. A **19**, 2652 (2001).

## APPENDIX B: LIST OF REACTIONS FOR Ar

<u>Reaction</u> <sup>a</sup>	<u>Rate Coefficient</u> (cm <sup>3</sup> s <sup>-1</sup> )	<u>Reference</u>
$e + \text{Ar} \rightarrow \text{Ar}^* + e$	b	1
$e + \text{Ar} \rightarrow \text{Ar}^{**} + e$	b	1
$e + \text{Ar} \rightarrow \text{Ar}^+ + e + e$	b	2
$e + \text{Ar}^* \rightarrow \text{Ar}^+ + e + e$	b	3
$e + \text{Ar}^* \rightarrow \text{Ar} + e$	b	d
$e + \text{Ar}^* \rightarrow \text{Ar}^{**} + e$	b	4
$e + \text{Ar}^{**} \rightarrow \text{Ar} + e$	b	d
$e + \text{Ar}^{**} \rightarrow \text{Ar}^+ + e + e$	b	5
$e + \text{Ar}^{**} \rightarrow \text{Ar}^* + e$	b	d
$\text{Ar}^* + \text{Ar}^* \rightarrow \text{Ar}^+ + \text{Ar} + e$	$5 \times 10^{-10}$	c
$\text{Ar}^{**} + \text{Ar}^{**} \rightarrow \text{Ar}^+ + \text{Ar} + e$	$5 \times 10^{-10}$	b
$\text{Ar}^{**} + \text{Ar}^* \rightarrow \text{Ar}^+ + \text{Ar} + e$	$5 \times 10^{-10}$	b
$\text{Ar}^{**} \rightarrow \text{Ar}^*$	$1 \times 10^7$	c
$\text{Ar}^* \rightarrow \text{Ar}$	-	c

<sup>a</sup>Only reactions which change the density of a species are shown. All pertinent electron impact processes, such as elastic collisions, are included in the EMCS. Ar<sup>\*</sup> is nominally the Ar (4s) manifold. Ar<sup>\*\*</sup> is nominally the Ar (4p) manifold.

<sup>b</sup>Rate coefficients are calculated from electron energy distribution obtained in the EMCS.

<sup>c</sup>Estimated.

<sup>d</sup>Cross section obtained by detailed balance.

## **B.1 References**

- [1] K. Tachibana, *Phys. Rev. A* **34**, 1007 (1986).
- [2] D. Rapp and P. Englander-Golden, *J. Chem. Phys.* **43**, 1464 (1965).
- [3] R. H. McFarland and J. D. Kinney, *Phys. Rev.* **137**, 1058 (1965).
- [4] I. P. Zapesochnyi and L. L. Shimon, *Opt. Spectrosc.* **11**, 155 (1966).
- [5] L. Virens, *Phys. Lett.* **8**, 260 (1964).

**APPENDIX C: LIST OF REACTIONS FOR Ar/Cl<sub>2</sub>**

<b><u>Reaction</u><sup>a</sup></b>	<b><u>Rate Coefficient</u> (cm<sup>-3</sup>s<sup>-1</sup>)</b>	<b><u>Reference</u></b>
$e + \text{Ar} \rightarrow \text{Ar}^* + e$	b	1
$e + \text{Ar} \rightarrow \text{Ar}^+ + e + e$	b	2
$e + \text{Ar}^* \rightarrow \text{Ar}^+ + e + e$	b	3
$e + \text{Ar}^* \rightarrow \text{Ar} + e$	b	d
$\text{Ar}^* + \text{Ar}^* \rightarrow \text{Ar}^+ + \text{Ar} + e$	$5 \times 10^{-10}$	c
$\text{Ar}^+ + \text{Ar} \rightarrow \text{Ar} + \text{Ar}^+$	$5.7 \times 10^{-10}$	c
$e + \text{Cl}_2 \rightarrow \text{Cl}^- + \text{Cl}$	b	4
$e + \text{Cl}_2 \rightarrow \text{Cl} + \text{Cl} + e$	b	4
$e + \text{Cl}_2 \rightarrow \text{Cl}_2^+ + e + e$	b	4
$e + \text{Cl} \rightarrow \text{Cl}^* + e$	b	4
$e + \text{Cl} \rightarrow \text{Cl}^+ + e + e$	b	4
$e + \text{Cl}^* \rightarrow \text{Cl}^+ + e + e$	b	4
$\text{Cl}^* \rightarrow \text{Cl}$	$1.0 \times 10^5 \text{ s}^{-1}$	c
$e + \text{Cl}^- \rightarrow \text{Cl} + e + e$	b	4
$e + \text{Cl}_2^+ \rightarrow \text{Cl} + \text{Cl}$	$1 \times 10^{-7} / T_e^{1/2}$	c
$\text{Cl}^- + \text{Cl}^+ \rightarrow \text{Cl} + \text{Cl}$	$1 \times 10^{-7}$	c
$\text{Cl}^- + \text{Cl}_2^+ \rightarrow \text{Cl}_2 + \text{Cl}$	$1 \times 10^{-7}$	c
$\text{Cl}_2 + \text{Ar}^* \rightarrow \text{Cl}_2^+ + \text{Ar} + e$	$7.1 \times 10^{-10}$	c
$\text{Cl}^- + \text{Ar}^+ \rightarrow \text{Cl} + \text{Ar}$	$1 \times 10^{-7}$	c
$\text{Cl} + \text{Ar}^* \rightarrow \text{Cl}^* + \text{Ar}$	$7 \times 10^{-10}$	c

$\text{Cl}_2 + \text{Ar}^+ \rightarrow \text{Cl}_2^+ + \text{Ar}$	$8.4 \times 10^{-9}$	5
$\text{Cl}_2 + \text{Ar}^+ \rightarrow \text{Cl}^+ + \text{Cl} + \text{Ar}$	$6.4 \times 10^{-9}$	5
$\text{Cl} + \text{Ar}^+ \rightarrow \text{Cl}^+ + \text{Ar}$	$2.0 \times 10^{-10}$	5
$\text{Cl} + \text{Cl} + \text{Ar} \rightarrow \text{Cl}_2 + \text{Ar}$	$1.28 \times 10^{-32} \text{ cm}^6/\text{s}$	5
$\text{Cl} + \text{Cl} + \text{Cl} \rightarrow \text{Cl}_2 + \text{Cl}$	$1.28 \times 10^{-32} \text{ cm}^6/\text{s}$	6
$\text{Cl} + \text{Cl} + \text{Cl}_2 \rightarrow \text{Cl}_2 + \text{Cl}_2$	$5.4 \times 10^{-32} \text{ cm}^6/\text{s}$	6
$\text{Cl}^+ + \text{Cl}_2 \rightarrow \text{Cl}_2^+ + \text{Cl}$	$5.4 \times 10^{-10}$	c,5
$\text{Cl}^+ + \text{Cl} \rightarrow \text{Cl} + \text{Cl}^+$	$1.0 \times 10^{-9}$	c
$\text{Cl}_2^+ + \text{Cl}_2 \rightarrow \text{Cl}_2 + \text{Cl}_2^+$	$0.8 \times 10^{-9}$	c

<sup>a</sup>Only reactions which change the density of a species are shown. All pertinent electron impact processes, such as elastic collisions, are included in the EMCS.

<sup>b</sup>Rate coefficients are calculated from electron energy distribution obtained in the EMCS.

<sup>c</sup>Estimated.

<sup>d</sup>Cross section obtained by detailed balance.

## C.1 References

- [1] K. Tachibana, *Phys. Rev. A* **34**, 1007 (1986).
- [2] D. Rapp and P. Englander-Golden, *J. Chem. Phys.* **43**, 1464 (1965).
- [3] R. H. McFarland and J. D. Kinney, *Phys. Rev.* **137**, 1058 (1965).
- [4] G. L. Rogoff, J. M. Kramer, and R. B. Piejak, *IEEE Trans. Plasma Sci.* **14**, 103 (1986).
- [5] Y. Ikezoe, S. Matsuoka, M. Takabe, and A. Viggiano, *Gas Phase Ion-Molecule Reaction Rate Constants Through 1986* (Mass Spectroscopy Society of Japan, Tokyo, 1987).
- [6] NIST Chemical Kinetics Database 17, Version 2Q98, <http://kinetics.nist.gov/index.php>.

**APPENDIX D: LIST OF REACTIONS FOR Ar/Cu**

<u>Reaction</u> <sup>a</sup>	<u>Rate Coefficient</u> (cm <sup>3</sup> s <sup>-1</sup> )	<u>Reference</u>
$e + \text{Ar} \rightarrow \text{Ar} + e$	b	1
$e + \text{Ar} \rightarrow \text{Ar}[4s] + e$	b	2
$e + \text{Ar} \rightarrow \text{Ar}[4p] + e$	b	2
$e + \text{Ar} \rightarrow \text{Ar}^+ + e + e$	b	3
$e + \text{Ar}^* \rightarrow \text{Ar}^+ + e + e$	b	4
$e + \text{Cu} \rightarrow \text{Cu}[^2\text{D}_{5/2}] + e$	b	5
$e + \text{Cu} \rightarrow \text{Cu}[^2\text{D}_{3/2}] + e$	b	5
$e + \text{Cu} \rightarrow \text{Cu}[^2\text{P}_{1/2}] + e$	b	5
$e + \text{Cu} \rightarrow \text{Cu}[^2\text{P}_{3/2}] + e$	b	5
$e + \text{Cu} \rightarrow \text{Cu}^+ + e + e$	b	5
$e + \text{Cu}^* \rightarrow \text{Cu}^* + e$	b	4
$e + \text{Cu}^* \rightarrow \text{Cu}^+ + e + e$	b	4
$\text{Ar}^* + \text{Ar}^* \rightarrow \text{Ar}^+ + \text{Ar} + e$	$5 \times 10^{-10}$	c
$\text{Cu}^* + \text{Cu} \rightarrow \text{Cu} + \text{Cu}$	$1 \times 10^{-12}$	c
$\text{Cu}^* + \text{Cu}^* \rightarrow \text{Cu} + \text{Cu}$	$1 \times 10^{-12}$	c
$\text{Cu}^* + \text{Ar} \rightarrow \text{Cu} + \text{Ar}$	$1 \times 10^{-12}$	c
$\text{Ar}^* + \text{Cu} \rightarrow \text{Cu}^+ + \text{Ar} + e$	$5 \times 10^{-11}$	c
$\text{Ar}^* + \text{Cu}^* \rightarrow \text{Cu}^+ + \text{Ar} + e$	$5 \times 10^{-11}$	c
$\text{Ar}^+ + \text{Cu} \rightarrow \text{Cu}^+ + \text{Ar}$	$1 \times 10^{-9}$	c
$\text{Ar}^+ + \text{Cu}^* \rightarrow \text{Cu}^+ + \text{Ar}$	$5 \times 10^{-11}$	c

<u>Reaction</u> <sup>a</sup>	<u>Rate Coefficient</u> (cm <sup>-3</sup> s <sup>-1</sup> )	<u>Reference</u>
Ar <sup>+</sup> + Ar → Ar + Ar <sup>+</sup>	1 × 10 <sup>-9</sup>	c
Ar <sup>+</sup> + Ar* → Cu <sup>+</sup> + Ar	1 × 10 <sup>-9</sup>	c
Cu <sup>+</sup> + Cu → Cu + Cu <sup>+</sup>	1 × 10 <sup>-9</sup>	c
Cu <sup>+</sup> + Cu* → Cu + Cu <sup>+</sup>	1 × 10 <sup>-9</sup>	c

<sup>a</sup>In the FKM all excitations of Ar are lumped into Ar\*, which is effectively Ar[4s], and all excitations of Cu are lumped into Cu\*, which is effectively Cu[<sup>2</sup>D<sub>5/2</sub>].

<sup>b</sup>Rate coefficients are calculated from electron energy distributions obtained in EMCS.

<sup>c</sup>Estimated.

## D.1 References

- [1] M. Hayashi, Nagoya Institute of Technology Report No. IPPJ-AM-19 (1991).
- [2] K. Tachibana, Phys. Rev. A **34**, 1007 (1986).
- [3] D. Rapp and P. Englander-Golden, J. Chem. Phys. **43**, 1464 (1965).
- [4] R. H. McFarland and J. D. Kinney, Phys. Rev. **137**, 1965 (A1058).
- [5] M. J. Kushner and B. E. Warner, J. Appl. Phys. **54**, 2970 (1983).

## **AUTHOR'S BIOGRAPHY**

Vivek Vyas was born in Ahmedabad, India. He received his B. Tech. degree in Metallurgical Engineering and Materials Science from the Indian Institute of Technology, Bombay, India, and his M.S. degree in Electrical Engineering from the University of Illinois at Urbana-Champaign. Under the direction of Professor Mark J. Kushner, he has studied low-temperature plasmas for semiconductor applications since August 2000. His work has resulted in three refereed journal publications and seven conference presentations.